Computational Modeling of Pad Surface Irregularities in Fluid Film Bearings

---

A Dissertation
Presented to
the faculty of the School of Engineering and Applied Science
University of Virginia

In Partial Fulfillment
of the requirements for the Degree
Doctorate of Philosophy

By:
Michael Branagan
June 2018

APPROVAL SHEET

The Dissertation
is submitted in partial fulfillment of the requirements
for the degree of
Doctorate of Philosophy

AUTHOR

The thesis has been read and approved by the examining committee:

Advisor

Advisor

Accepted for the School of Engineering and Applied Science:

Dean, School of Engineering and Applied Science

August

2019

Abstract

Bearings serve a critical role in rotordynamic systems by providing support for the rotating components. Fluid-film bearings work by supporting the rotor on a thin film of fluid. This type of bearing can be responsible for providing the majority of damping in a system, which reduces rotor vibrations. The working surfaces of these bearings are often made of a softer, sacrificial layer that is used to protect the rotor surface in the case of metal-to-metal contact and to absorb any hard particulates in the fluid that could score the journal surface. Under heavy loads, this layer can be heavily damaged resulting in bearing failure when the journal speed is too slow to support the load on a hydrodynamic film. In these cases, high pressure oil is often supplied to the working surface of the bearing via ports to lift the rotor hydrostatically. These ports are feed into machined jacking pockets or grooves, which serve to distribute the oil underneath the rotor. The bearing load is then held hydrostatically until the rotor speed is adequate to support the load on a hydrodynamic film. Often the high pressure oil supply is shut off during normal operation to reduce power loss. It is generally assumed that these pockets and grooves do not affect the hydrodynamic performance of the bearing but data on the accuracy of this assumption is limited.

This dissertation presents a comprehensive, multi-part study on the influence of hydrostatic lift features on the performance of fluid-film, journal bearings and an additional study on the applicability of different turbulence models in thin-film applications. The first study presents an examination of a two-pad, fixed-geometry bearing with a stadium-shaped/rectangular jacking pocket using CFD simulations. As the depth of the feature increases, the pressure profile is found to shift through two different regimes. The first is characterized by an increase in the load capacity of the bearing and occurs with depths shallower than $0.28\times$ the bearing radial clearance (C_b). The second regime is characterized by a loss of load capacity and an equalizing of the pressure throughout the pocket. This regime occurs for pockets with depth up to $6.6 \times C_b$. Finally, increasing the pocket depth beyond this depth does not change the pressure profile or further reduce load capacity. Next design-of-experiment and regression models were utilized to examine the influence of the jacking pocket geometry on the power loss, journal position, and stiffness of the film. The bearing stiffnesses varied by up to 25% from the nominal, smooth bearing case for the direct stiffnesses and 12% for the cross coupled stiffnesses. Current literature on fluid-film bearings with hydrostatic lift features has been limited to multi-recess bearings with applied high pressure oil or to thrust bearings. This paper is the first to examine the influence of the geometry of one such feature on the operational and dynamic

characteristics of the bearings.

The next study expanded upon the first study by examining the influence of a pair of double diamond, jacking pockets and an hourglass-shaped, jacking groove on the same two-pad bearing. The same two regimes were found as the depth of the jacking feature was increased. The first regime occurs with depths shallower than $0.28 \times C_b$ to $0.60 \times C_b$. For all three jacking features, the second regime occurred for pocket depths up to $7 \times C_b$. Increasing the feature depth beyond this depth ceased to influence the pressure profile further. Next design-of-experiment and regression models were used to examine the influence of the the different jacking feature geometries on the power loss, journal position, and stiffness of the film. The presence of all three jacking feature had a minimal influence on the bearing power loss and the journal position. The power loss varied between 3% to 1% of the nominal, smooth bearing case for the different designs. The journal position varied up to 6% of the nominal case. The bearing stiffnesses varied by up to 40% from the nominal case for the direct stiffnesses and 104% for the cross coupled stiffnesses. The jacking grooves had significantly less influence than the pockets. This study expanded the applicability of the first novel study by examining two additional jacking features, which included multiple pockets and a system of grooves.

The third study was an examination of the applicability of the Reynolds equation in analyzing bearings with jacking grooves. Several methods were examined to allow the use of Reynolds equation. Biasing the element distribution towards the jacking features was crucial for keeping the analysis runtime within a reasonable limit while still achieving accurate results. The Reynolds equation was compared with CFD results for several different pocket geometries. The Reynolds equation accurately captured the pressure profile, despite the lack of fluid inertia, when an optimization was performed on the journal position. Furthermore, the increase in rotor eccentricity compared with the CFD equilibrium position was limited to 4% of the radial clearance. Reynolds equation is thus an excellent tool for efficiently analyzing bearings with jacking features and will result in a slightly more conservative bearing design due to the lack of inertia. Multiple studies have been performed on hydrostatic lift features which utilized the Reynolds equation for capturing the hydrodynamic behavior in the bearing. This has been done without any justification for its use. This study was the first to examine the applicability of the Reynolds equation and its assumptions across a hydrostatic lift feature. This study will increase the credibility of these studies by providing justification for its use.

Computational fluid dynamics (CFD) is a powerful tool for examining the behavior in a fluid-film bearing. Modeling turbulence in a bearing is challenging due to the wide range of Reynolds number that can occur in a single bearing. The last study examines three different methods for modeling turbulence, along with the laminar assumption, in a four-pad journal bearing using CFD. The predominant model that is used with CFD in prior literature is a two-equation turbulence model. This is often done regardless of the Reynolds number or presented with inadequate data for calculating the Reynolds number. A pad model was developed for a four-pad, tilting-pad, journal bearing. Each model is simulated across a broad range of Reynolds numbers. The two-equation is not always the best choice and justification should be presented for the choice of turbulence model. The one-equation turbulence model has the advantage of accurately predicting the behavior of laminar flow and providing a better prediction near the onset of turbulence. This is highly advantageous in bearings where portions of the film can be turbulent while other portions are laminar. A single turbulence model can be provided for the whole bearing which will greatly reduce simulation runtimes.

Table of Contents

List of Figures

List of Tables

1 Introduction

Bearings are machine components used to support rotating machinery. There are two main types of bearings: radial journal bearings and thrust bearings. Journal bearings are used to support lateral loads, which include the weight of the shaft in horizontal machines, while thrust bearings are used to support any axial (thrust) loads. Fluid-film bearings are common in many types of rotating machines and carry the applied loads on a thin film of fluid. These bearings can have excellent load capacities and damping characteristics, without significant complexity. The performance of the bearing is dependent upon the eccentricity or displacement of the journal axis from the centerline of the bearing for journal bearings or the height of the runner for thrust bearings, which is a function of the applied loads. The temperatures in the bearing, the resulting fluid viscosity, and structural deformations are also important for proper bearing operation. Bearings contribute both stiffness and damping to the overall rotordynamic system. Often the damping is crucial for successful rotor operation at velocities higher than the system critical speeds, while the stiffness can be important in positioning those critical speeds away from the machine operating speeds.

1.1 Overview of Previous Work

Fluid-film bearings are widely used components in many rotordynamic machines. Accurately understanding the steady-state and dynamic behavior of these components can be critical to proper and safe machine operation. This is especially true as machine operating speeds and applied loads on the bearings increase.

To compensate for high loads during machine startup and shutdown and to avoid wiping of the bearing surfaces, hydrostatic ports, grooves, and pockets are often machined into the surfaces of the bearings. These ports are supplied with pressurized lubricant to hydrostatically lift the journal and avoid dry rubbing of the metal components. Pockets and grooves are machined to distribute the lubricant underneath the journal and hydrostatically support the rotor. Girard first took out a patent on hydrostatic, water bearings as early as 1865, although they remained little more than curiosities for three-quarters of a century. In 1973, Walter and Brasch [1] presented a detailed report on the first application of hydrostatic bearings in industrial machines. Hydrostatics was first applied as a lifting feature to gas bearings in 1953. More recently there has been some investigations into the influence of these jacking features. Raud et. al. [2] presented a 3D isothermal, numerical study into the behavior of a journal bearing with jacking pockets at low speeds.

This study ignored the rapid pressure changes that can hydrodynamically occur at the leading and trailing edge of the pockets. Thus their numerical methods are only applicable at low speeds when the hydrodyamic influences of the bearing are negligible.

Some bearings are designed for a continuous flow of the high pressure oil during operation. This tends to improve the load capacity of the bearings but increases the power loss in the machine. These bearings are commonly referred to as hybrid bearings as they rely on both hydrostatics and hydrodynamics in their operation. Most of these bearings have a series of pockets in close proximity to each other and are referred to as multirecess bearings. There are a variety of different approaches used for capturing the influence of the hydrodynamics in multi-recess, hydrostatic, journal bearings. San Andres [3] presented a numerical analysis of hydrostatic, journal bearings. This was done by solving the 2D momentum and continuity equations on the bearing lands coupled with the continuity equation throughout the bearing pocket. These equations were coupled with a pressure spike equation found by Constantinescu and Galetuse [4]. San Andres found that fluid inertia is crucial in hydrostatic bearings and will result in higher recess pressures. Braun et. al. [5] used the 2D momentum and continuity equations to examine the flow in a recess. They examined the influence of the pocket depth, among other things, on the pressure profile. It was found that a shallow pocket would have an improved pressure profile resulting in an increased load capacity. As the pocket became deep (a 1.5 ratio of the rotating surface height, assuming a concentric rotor and the recess depth), the pressure profile would cease to change. Helene et. al. [6] performed a two-dimensional CFD analysis of just the jacking recess, assuming an infinitely long bearing and recess. The paper examines the recirculation in the recess and its effect on the pressure under both laminar and turbulent flow conditions. They concluded that it was very difficult to separate the viscous and inertial effects in the flow in the recess. Helene et. al.[7] expanded this study by solving the full 3D Navier-Stokes equation in a single rectangular pocket. Liang et. al. [8] performed a numerical analysis on a hydrostatic journal bearing but chose to ignore the hydrodynamic influence all together. No justification was presented for this assumption. Several authors have performed numerical studies of these bearing by coupling hydrostatic results together with a hydrodynamic smooth bearing model. Johnson and Manring [9] performed a 1-D analytical study of a single thrust pad with a hydrostatic lift pocket. The pressure is solved for using the Reynolds equation but different boundary conditions are applied for the pressure induced by the oil injection than for the pressure due to the thrust runner motion. However, the validity of the Reynolds equation near the edge of the pockets due to the sudden transition in film thickness is not discussed. The study found that wide deep pockets exhibited the largest load capacity, and that the impact of the pocket depth is reduced as the depth increases past the nominal film thickness. Kumar et. al. [10] performed such an analysis on a hydrostatic journal bearing and using the Reynolds equation to account for hydrodynamics and the Dufrane model [11] to account for wear. Dwivedi et. al. [12] assumed a linear decrease of pressure across the bearing land due to the land's narrowness. While a variety of different approaches have been used to analyze the performance of multi-recess hydrostatic journal bearings, most of them rely on several large assumptions related to the hydrodynamic portion of the physics (ignored hydrodynamic effects [9], assumed a smooth pad for hydrodynamic effects [8], used the Reynolds equation [10]), and adequate justifications are not presented in their defense.

Other times the high pressure ports are shut off during hydrodynamic operation to reduce power losses in the machine. There have been a small number of studies devoted to examining the influence of the presence of jacking features on the hydrodynamic performance of fluid-film bearings, with the majority of these papers having a thrust bearing application. In 1975, Wordsworth and Ettles [13] performed a simple numerical calculation using Reynolds equation on the influence of jacking pockets on hydrodynamic thrust pads. They found that pockets with areas of 25% of the pad surface area had a load capacity of 91% of a pad without the pocket. This loss could be minimized if the recesses follow the constant pressure contours on the pad. Heinrichson [14] wrote his dissertation on the numerical modeling of thrust bearings with jacking pockets. He used a 3-D thermoelastohydrodynamic (TEHD) analysis of tilting-pad thrust bearings including recesses. An extended Reynolds equation is solved for the film ignoring inertial effects. Three-dimensional thermal analyses were used for deep recesses assuming uniform recess temperature caused by the re-circulation in the recess. This same re-circulation was absent in grooves with a depth the same order of magnitude as the film thickness. The dissertation showed that bearings with recesses resulted in a decrease in friction coefficient. Heinrichson et. al. [15, 16] performed a numerical and experimental study examining the influence of injection pockets on the performance of tilting-pad thrust bearings. The developed numerical model was a three-dimensional TEHD analysis of a single thrust pad including the injection pocket utilizing the Reynolds equation. The model was able to demonstrate that a shallow pocket at a depth of $1.1\times$ the nominal runner height is able to positively contribute to the load capacity of the bearing while a deeper pocket has a negative effect. This numerical work was also coupled with an experimental study [16] in which the influence of the oil injection pocket on the pressure distribution and the oil film thickness was investigated. The numerical model corresponded well at low loads but differences up to 25% were seen at the higher applied loads and rotor velocities. De Pellegrin and Hargreaves [17] presented a numerical study of a sector-shaped pad examining the effect of the recess size and shape on bearing performance. Isoviscous and isothermal assumptions were made. The study found that certain types of grooves can promote oil film thickness and reduce power loss up to a certain angular velocity and viscosity thresholds. Fillon et. al. [18] performed a THD analysis of a large tilting-pad thrust bearing with a lifting pocket. Previous papers [19, 20] had performed analyses on the same bearings but neglected to model the pocket. Fillon et. al. [18] coupled the generalized Reynolds equation with the full three-dimensional energy equations. The conical pocket was modeled by increasing the oil film thickness at the pocket. To achieve convergence, a much finer mesh was required than in the previous studies [19, 20]. The author found that the recesses had a significant effect on both the pressure and temperature fields. Zouzoulas and Papadopoulos [21] performed a computational fluid dynamics (CFD) analysis on a variety of thrust bearing pads with various surface geometries and properties, including a pad with one large pocket, a pad with several circumferential grooves, a pad with several radial grooves, a pad with a series of rectangular texturing (very small pockets), and a smooth pad with a hydrophobic surface. The authors solved for the numerical solution of the Navier Stokes and energy equations for incompressible flow. The bearing with the single large pocket with a depth of $1\times$ the nominal runner height was found to increase the minimum film thickness by up to 20%, lower the friction torque by up to 8% and decrease the maximum film temperature by up to 8° C, while the bearing with the circumferential grooves saw similar but lower numbers for each of the prior bearing flow characteristics. The bearings with the radial grooves and with the rectangular texturing were both shown to inhibit the pressure buildup as the edges of the surface feature were perpendicular to the flow path. In 2017, Fu and Untaroiu [22] published a paper where they presented a methodology for predicting the behavior of fluid-film journal bearings with rectangular, circular, triangular, elliptical, and annular shaped jacking recesses. The paper focused on the statistical methodology and presented results in the form of figures of the overall flow patterns. The main focus on bearings with jacking features has been on hydrostatic operating conditions and on thrust bearings. The primary method of modeling the influence of hydrodynamics has been the use of Reynolds equation. This has been done with no justification for its application.

Another phenomena this dissertation examines is turbulence. Turbulence can be an important feature that many studies have ignored or considered improperly. Turbulence is a deviation from the stable laminar flow conditions, in which the fluid moves in layers, to a more irregular flow. While a turbulent flow is characterized by randomness with respect to both time and spatial coordinates, it can be characterized by statistically distinct average values [23]. Turbulence is caused by high friction forces at a wall or between different fluid layers of varying velocities. The viscosity of the fluid dampens out turbulence as more viscous fluids can absorb more of the kinetic energy [24]. Predicting the transition from laminar to turbulent flow is difficult and not well understood. Turbulence can have a significant influence on the operation of fluid-film journal bearings. This is especially true for bearings operating at high speeds or which use low viscosity fluids, such as water, as the working fluid [25]. Turbulence will begin to occur locally in flows with Reynolds numbers of 2000 and higher, where $Re = r\omega h/\nu$ is the local Reynolds number [26, 27].

The onset of turbulence will cause an increase in the heat transfer in the film, thereby lowering the peak film temperature. Szeri [28] found that the onset of turbulence causes a decrease in the maximum pad temperature. Hopf and Schüler [29] confirmed this behavior and found that this drop in temperature occurs in the vicinity of the minimum film thickness where the largest variation in temperature exists. They attributed this behavior to the mixing and increased heat transfer in the presence of high thermal gradients. Therefore, turbulent bearings will often run with lower peak temperatures than laminar bearings. However, as the turbulence increases further, this cooling effect can be offset by the increased heat generation [26, 30, 31]. Turbulence will usually result in an improvement in the load capacity of the bearing [32, 33, 25]. The lower film temperatures and improved load capacity will cause a variation of the journal equilbrium eccentricity, which along with the changes in the fluid characteristics, will alter both the stiffness and damping characteristics of the film. Turbulence also causes an increase in the power loss of a bearing, which can be up to 1000 horsepower in bearings larger than 31 inches in diameter [34].

To solve the inherent closure problem that occurs in turbulence problems, Boussinesq [35] related turbulence shear stress to mean flow variables using Equation 1.1.

$$\tau_{ij} = 2\mu_t S^*_{ij} - \frac{2}{3}\rho k \delta_{ij}, \tag{1.1}$$

where τ_{ij} is the Reynolds stress tensor, μ_t is a proportionality constant called the eddy viscosity, S^*_{ij} is the trace-less mean strain rate tensor, ρ the fluid density, k is the turbulent kinetic energy, and δ_{ij} is the Kronecker delta. This relationship is utilized in a branch of turbulence models known as eddy viscosity models. The primary distinction between the different eddy viscosity models is the method by which the eddy viscosity term is calculated. These models are commonly categorized by the number of differential equations that are required to solve for the eddy viscosity. zero-equation models relate the eddy viscosity algebraically to various flow parameters. one-equation models add a differential equation that is used to solve for the turbulent kinetic energy (k). two-equation models add an additional equation that solves for some form of the turbulent dissipation (ϵ, ω). Both the one and two-equation models then algebraically relate these new turbulent parameters to calculate the eddy viscosity.

Constantinescu [36] developed analytical equations for the velocity distributions in a film using Prandtl mixing length hypothesis and the thin film approximation. Prandtl mixing length hypothesis is given by Equation 1.2.

$$-\rho\overline{u'v'} = \rho l^2 \frac{\partial \bar{u}}{\partial y}|, \frac{\partial \bar{u}}{\partial y}|, \tag{1.2}$$

where $\overline{u'v'}$ represents the Reynolds stresses and l is the mixing length. The exact dependence of the rate of flow on the pressure dependence is replaced by a linear relationship to obtain a simple pressure differential equation and its solution. Ng [37] worked to fix some anomalies with Constantinescu's work [36] by using Boussinesq approximation [35] for the Reynolds stresses which resulted in Equation 1.3 for two-dimensional thin film flow

$$\tau = \mu_t(1 + \frac{\epsilon}{\nu})\frac{du}{dy}, \tag{1.3}$$

where ϵ is the turbulent diffusivity. Reichardt's formula [38] (Equation 1.4) is used to calculate the eddy diffusivity.

$$\frac{\epsilon}{\nu} = k(y^+ - \delta_l^+ tanh\frac{y^+}{\delta_l^+}), \tag{1.4}$$

where k and δ_l^+ are constants, y^+ is the dimensionless distance to the wall and is equal to $\frac{yu_t}{\nu}$, y is the distance from the wall, and u_t is the "wall velocity" parallel to the wall ($\sqrt{\frac{\tau_w}{\rho}}$). These assumptions allow for the development of alternative equations for the velocity profile. Both Constantinescu's [36] and Ng's [37] velocity equations are based on perturbing a Coullete flow. Elrod and Ng [39] applied the theory developed by Ng [37] to the flow inside of fluid-film bearings and expanded it to include both Coullete and Poseuille flows.

In 1970, Hanjalick [40] developed a turbulence model composed of two partial differential equation for the turbulent kinetic energy (k) and the turbulent dissipation rate (ϵ). These terms were algebraically related to the eddy viscosity. To apply the model to the viscous layer, Jones and Launder [41] added viscous diffusion, Reynolds number dependent functions, and additional terms to account for the fact that the dissipation processes are not isotropic. This model is known as the k-ϵ turbulence model and was further validated by Launder and Sharma [42].

In 1988, Wilcox [43] made a review of the current two-equation turbulence models and determined that these models failed to accurately predict boundary layer flow in the presence of an adverse pressure gradient. He developed a new model to better account for this short coming. This model was further improved to account for misalignment of the Reynolds stress tensor and the mean strain rate tensor principle axes [44]. This model is known as the k-ω turbulence model. Mentor [45, 46] further developed the model by Wilcox [43] to remove the dependence on arbitrary free stream values. This was done by using the Wilcox [43] model for the first 50% of the boundary layer and then transitioning to the Jones and Launder's [41] k-ϵ model in a k-ω formulation. This model is known as the Baseline (BSL) k-ω model. Mentor [45, 46] made further modifications to the BSL model to develop the Shear Stress Transport (SST) k-ω model.

In 1997 Mentor [47] combined Bradshaw's assumption [48] in which the turbulent kinetic energy is assumed to be proportional to the turbulent shear stresses, with the k-ϵ turbulence model to develop a one-equation turbulence model known as the Eddy Viscosity Transport model. Reynolds equation uses a thin film approximation to reduce the Navier-Stokes equations into a single differential equation. There have been numerous modifications made to the Reynolds equation to incorporate a turbulence model. A zero-equation, eddy viscosity model is usually used [49, 50, 51].

With the increase in computational power, the use of computational fluid dynamics (CFD) to solve the full or steady Navier-Stokes equations in the analysis of the operation of fluid-film bearings has become more prevalent. The proper use of turbulence models is important to fully understand the bearing behavior. Unfortunately, many of the papers utilizing CFD neglect to mention the Reynolds number and turbulence model that were used. Those papers which do specify a turbulence model tend to heavily favor the two-equation turbulence models although a justification for this choice is generally not given. For example, Ravikovich et. al. [52] performed a steady-state CFD study on three different bearings which used water, oil, and gas as the operating fluids. They used the SST k-ω turbulence model for all of the bearings despite the huge variance in the Reynolds number. The oil bearing was operating at Reynolds numbers below 5, while the water bearing and the gas bearing operated at Reynolds numbers above $1e7$. Ghezali et. al. [53] analyzed the flow in a hydrostatic bearing with Reynolds numbers varying from

500-3500. Again the SST k-ω turbulence model was used for all of the analyses. Worse, many authors do not provide enough information to calculate the Reynolds number of the bearing flow. Edney et. al. [54], Uhkoetter et. al. [55], Manshoor et. al. [56], and Fu and Untaroiu [22] all used k-ϵ models. These studies examined oil flow in a variety of bearing types. (hydrostatic bearings [22], fixed-geometry bearings [55, 56] and six-pad, tilting-pad bearings [54]). However, inadequate information was provided to calculate the Reynolds numbers. This missing data makes examining the validity of the chosen turbulence model impossible. Several of these different turbulence models are used in this dissertation to examine the applicable ranges in thin film applications.

1.2 Scope of Current Work

The primary focus of prior research in the literature related to bearings with jacking features has been on either hydrostatic operation or on thrust bearings. These often involve the use of the Reynolds equation without any justification for the appropriateness of its use. As such, an important goal of this work was to expand current understanding by looking at the influence of jacking pockets on the performance of fluid-film, journal bearings. This was done in two stages to gain insight into the appropriateness of Reynolds equation. First, multiple CFD studies were performed on three different jacking feature geometries, including both pockets and a groove. Several of these studies were then repeated using the Reynolds equation, and these results are compared with the CFD.

The second chapter of this dissertation focuses on the hydrodynamic regime of a fluid-film, journal bearing with a rectangular/stadium-shaped jacking pocket. CFD was used to examine the influence of the pocket on the operation of the bearing. These findings were used to make an initial examination of the validity of the assumptions involved in the Reynolds equation. The influence of the various geometric parameters of a stadium-shaped jacking pocket on the performance and dynamic characteristics of a journal bearing were examined using CFD. A baseline, numerical model was developed and validated without the presence of the jacking pocket. The jacking pocket was added to the model, and an investigation was performed examining the influence of the depth and circumferential length of the jacking pocket on the pressure profile of the film. Next, a series of simulation cases were selected using design-of-experiment methods. The test cases were used to create response surface models relating the jacking pocket geometry to the static and dynamic characteristics of the bearing. The goal of this study was to develop an increased understanding of the influence of jacking pocket geometry on the performance of fluid-film, journal bearings, which has been largely absent in literature. This study is the first to examine how each aspect of a jacking pocket's geometry influence the operation and linear stiffness values of a fluid-film journal bearing.

The third chapter presents an extension of the second chapter by examining two additional jacking feature geometries. The two geometries selected for this study were a pair of diamond-shaped pockets and an hourglass-shaped groove. Some initial studies were performed on these different geometries examining the influence of particular aspects of their geometries at a fixed journal position. The depth of both geometries was varied in a similar manner as performed in Chapter 2. The width of the hourglass-shaped groove was also varied to further understand the transition between pockets and grooves. Separate design-of-experiments were then performed for both jacking features. The influence of the geometries on the power loss, journal eccentricity position, and direct and cross-coupled stiffnesses were examined. Linear regression models were developed for each case and the relationships were discussed in terms of the physics. This study expanded upon the first study by adding two additional jacking feature geometries, making all of the results more applicable over a broader ranges of geometries.

The fourth chapter presents an examination of the use of Reynolds equation in analyzing bearings that includes jacking pockets. The stadium-shaped jacking pockets from Chapter 2 were used. A new tool was developed which solves the Reynolds equation while allowing axial variation in the film thickness. Several different methods are presented with the goal of reducing the simulation runtime while still achieving accurate results. These methods were then applied to a range of pocket depths and compared with the CFD results from Chapter 2. A discussion is included on the applicability and the advantages of the different methods. Lastly, the superior method was compared with several of the pocket designs that were developed in the design-of-experiment performed on the stadium-shaped pocket previously. The Reynolds equation results were compared with the CFD results while maintaining identical film geometries as the CFD. Then an optimization was performed on the Reynolds solution to find an equilibrium journal position. These new results along with the new journal equilibrium position were compared with the CFD results. Justification for the acceptable use of the Reynolds equation for bearings with hydrostatic lifting feature has not been previously addressed in the literature. This chapter demonstrates how the Reynolds equation can successfully be used to capture the physics that occur in these bearings

An additional study was performed on the use of different turbulence models in CFD models of bearings. The two-equation, turbulence model is the primary turbulence model used in CFD in literature. This was often done with little justification of the choice of model and often presented with inadequate data for calculating the Reynolds number. Therefore, the fifth chapter of this dissertation presents a study of three different turbulence models, along with the laminar model, over a wide range of Reynolds numbers to try to better determine the applicability of each model. A discussion is presented on different flow conditions that occur in tight clearances, as seen in fluid-film bearings. A CFD model of a four-pad, tilting-pad bearing was developed and validated versus experimental results [57]. This CFD model was used to examine a two-equation model (k-ω SST), a one-equation model (eddy viscosity transport), a zero-equation model, and a laminar model over a broad range of Reynolds numbers from 10 to 40e3. The fifth chapter of this document presents an argument against always using the more complicated turbulence model for all flow conditions in thin film applications, which has been the trend in the literature.

2 Hydrodynamic Performance Characteristics of a Fluid-Film Journal Bearing with a Rectangular Jacking Pocket

Nomenclature

C_b Bearing radial clearance
d Pocket depth
h Local film thickness
K Stiffness
l_c Pocket circumferential length
$l_{c,pad}$ Pad circumferential length
P Pressure
U Surface velocity
l_a Pocket axial length
$l_{a,pad}$ Pad axial length
x Circumferential coordinate
y Axial coordinate
μ Local fluid viscosity
ξ Power loss
ρ Fluid density
τ_s Surface shear stress

2.1 Introduction

Fluid-film bearings are widely used components in many rotating machines. Accurately understanding the dynamic behavior of these components is critical to proper and safe machine operation. This is especially true as machine operating speeds and applied bearing loads increase.

To compensate for high loads during machine startup and shutdown, and to avoid wiping or damaging the bearing surface, hydrostatic pockets and grooves containing ports to the pressurized lubricant supply can be added to the bearings. Hydrostatic ports are supplied with pressurized lubricants during startup and shutdown to lift the shaft and avoid severe rubbing. Pockets and grooves are added to adequately distribute the lubricant underneath the journal and ensure rotor lift off is achieved prior to startup. More recently, there have been some investigations into the influence of these jacking pockets on bearing performance. Sometimes the supply pressure to these ports is left on during the regular, hydrodynamic bearing operation to improve the load capacity of the bearings. This bearing design is commonly referred to as a hybrid bearing as it includes both hydrostatics and hydrodynamics in their operation. San Andres [3] presented a numerical analysis of hydrostatic, journal bearings. This was done by solving the 2D momentum and continuity equations on the bearing lands coupled with the continuity equation throughout the bearing pocket. This was coupled together with a pressure spike equation found by Constantinescu and Galetuse [4]. San Andres found that fluid inertia is crucial in hydrostatic bearings and will result in higher recess pressures. Braun et. al. [5] used the 2D momentum and continuity equations to examine the flow in a recess. They examined the influence of the pocket depth, among other things, on the pressure profile. It was found that a shallow pocket would have an improved pressure profile. As the pocket became deep (a ratio of the rotating surface height, assuming a concentric rotor, and the recess depth of 1.5), the pressure profile would cease to change. Helene et. al. [6] performed a two-dimensional CFD analysis of the jacking recess alone, assuming an infinitely long bearing and recess. The paper examined the influence of the local Reynolds number and the pocket depth on the fluid recirculation in the recess and the pressure distribution under both laminar and turbulent flow conditions. They found that it is difficult to separate the viscous and inertial effects in the recess flow. Helene et. al.[7] expanded this study by solving the full 3D Navier-Stokes equation in a single rectangular pocket. Liang et. al. [8] performed a numerical analysis on a hydrostatic journal bearing, but chose to ignore the hydrodynamic regime all together. No discussion is presented as to the errors introduced due to this assumption. Several authors have performed numerical studies of these bearings by coupling hydrostatic results together with a hydrodynamic smooth bearing model. This method ignores any influence that the recess has on the hydrodynamic flow. Johnson and Manring [9] performed a 1-D analytical study of a single thrust pad with a hydrostatic lift pocket. The laminar Reynolds equation was solved to calculate the hydrodynamic pressure, and flow rate equations were used to determine the hydrostatic pressure. These two resulting pressures were then summed together. One of the key assumptions of the Reynolds equation is the thin film assumption. No discussion is presented as to the validity of this assumption near the edge of the pockets due to the sudden transition in film thickness. The study found that wide, deep pockets exhibited the largest load capacity, where deep pockets are defined by a depth of 0.75 times the nominal film thickness. This study was limited to relatively shallow pockets. Pocket depths varying up to 50 times the nominal film thickness are commonly used in industrial practice. Johnson and Manring [9] state that the impact of the pocket depth is reduced as the depth increases past unity with the nominal film thickness. Kumar et. al. [10] also performed a Reynolds equation based analysis on a hydrostatic journal bearing and using the Reynolds equation to account for hydrodynamics and the Dufrane model [11] to account for wear. The various hydrodynamic assumptions (ignored hydrodynamic effects [9], assumed a smooth pad for hydrodynamic effects [8], used the Reynolds equation [10]) made in these papers may not be adequate in capturing the whole physics of these bearings, and adequate justifications are not presented in their defense.

For other bearing designs, the sole purpose of the jacking feature is to sustain the rotor in the high friction regimes. In these cases, the supply pressure to the hydrostatic ports is shut off to reduce power losses in the machine. There have been few studies devoted to examining the influence of jacking features on the hydrodynamic performance of fluid-film bearings. The majority of papers that investigate jacking pocket effects have been related to thrust bearing applications. In 1975, Wordsworth and Ettles [13] performed a simple numerical calculation using the Reynolds equation to model the influence of jacking pockets on hydrodynamic thrust pads. They found that thrust pads with pockets taking up 25% of the pad surface area had a load capacity of 91% of a pad without the pocket. This loss was minimized if the recesses followed constant pressure contours on the pad. Heinrichson [14] wrote a dissertation on the numerical modeling of thrust bearings with jacking pockets. The dissertation employed a 3-D thermoelastohydrodynamic (TEHD) analysis of tilting-pad thrust bearings including recesses. An extended Reynolds equation is solved for the film, ignoring inertial effects. The temperature in the recess was assumed to be uniform due to the flow recirculation. Three-dimensional thermal analyses were used for the rest of the flow and pads including this boundary condition. Re-circulation was absent in pockets with a pocket depth on the same scale as the film thickness. The dissertation showed that these recesses decreased the friction coefficient of the bearings. Heinrichson et. al. [15, 16] performed a numerical and experimental study examining the influence of injection pockets on the performance of tilting pad thrust bearings. The numerical model was a three-dimensional TEHD analysis of a single thrust pad, including the injection pocket, utilizing the Reynolds equation. The model showed that a shallow pocket at a depth of $1.1\times$ the nominal runner height positively contributes to the load capacity of the bearing, while a deeper pocket has a negative effect. Heinrichson also performed an experimental study [16] which investigated the influence of the oil injection pocket on the pressure distribution and the oil film thickness. The numerical model corresponded well at low loads but predicted runner heights up to 25% lower than the measurements at the higher loads and velocities. Fillon et. al. [18] performed a THD analysis of a large tilting-pad thrust bearing with a lifting pocket. Previous papers [19, 20] had performed analyses on the same bearings but failed to capture the physics adequately near the lifting pocket due to neglecting to model the pocket. Fillon et. al. coupled the generalized Reynolds equation with the full three-dimensional energy equations. The conical pocket was modeled by a series of steps with increasing oil film thickness. To achieve convergence, a much finer mesh (860% increase in number of elements) was required than in the previous studies [19, 20]. The recesses had a significant effect on both the pressure and temperature fields.

The primary focus of prior research in the literature on bearings with jacking features has been on either the hydrostatic operation or on the operating characteristics of thrust bearings. This study focuses exclusively on the hydrodynamic regime of a fluid-film journal bearing containing a rectangular/stadium-shaped, jacking pocket. CFD was used to achieve high accuracy. These findings were used to make an initial examination of the validity of the Reynolds equation assumption. The influence of the various geometric parameters of a stadium-shaped, jacking pocket on the performance and dynamic characteristics of a journal bearing were examined using CFD. A baseline numerical model was developed and validated without the presence of the jacking pocket. The jacking pocket was added and an investigation was performed examining the influence of the depth and circumferential length of the jacking pocket on the pressure profile of the bearing. Next a series of simulation cases were selected using design of experiments methods. The test cases were used to create response surface models relating the jacking pocket geometry to the static and dynamic characteristics of the bearing. The goal of this study was to develop an increased understanding of the influence of jacking pocket geometry on the performance of fluid-film, journal bearings, which has been largely absent in literature.

The objectives for this chapter were to:

1. Develop an understanding of how the depth of the pocket influences the
    - Pressure profile throughout the film
    - The hydrodynamic forces
2. Develop an understanding of how the circumferential width of the pocket influences the pressure profile throughout the film
3. Understand how the different aspects of the stadium-shaped, jacking pocket geometry (axial length, circumferential length, pocket depth) influence the
    - The direct (K_{xx} and K_{yy}) and cross-coupled (K_{xy} and K_{yx}) stiffnesses

Table 1: Fitzgerald and Neal [58] bearing geometry

Journal Diameter	mm	76.2
Axial Length	mm	38.1
Pad Thickness	mm	9.5
Radial Cb	mm	0.076
Pad Arc Length	deg	151.3
Preload		0.0
Offset		0.5
Shell Heat Conductivity	W/m-°C	50
Lubricant Density	kg/m	855
Lubricant Specific Heat	J/kg-°C	1952
Lubricant Heat Conductivity	W /m-°C	0.15
Lubricant Viscosity at 40 °C	Pa-s	0.028
Lubricant Viscosity at 99 °C	Pa-s	0.0047
Lubricant Supply Temperature	°C	50
Shaft Speed	rpm	8000
Load	kN	5.43

- Power loss
- Journal equilibrium position (eccentricity ratio and attitude angle)

4. Develop models for each of these outputs

2.2 CFD Model

The experimental study of Fitzgerald and Neal [58] was chosen as the baseline for this study. The bearing is a two-pad, fixed-geometry bearing with geometry characteristics and operating conditions given in Table 1 and a lateral cross section illustrated in Figure 1.

Fitzgerald and Neal [58] presented thermal results from their experiments. However, in this study, an isothermal assumption was used as the focus was on the flow characterstics of bearings with jacking pockets. The initial CFD model was validated by creating a model of the bearing using a 2-D thermoelastohydrodynamic (TEHD) code called MAXBRG [59]. This program solves the 2-D modified Reynolds, energy, and elasticity equations. The code calculates the maximum Reynolds number in the bearing and uses either the Reichardt turbulence model [38] or a laminar assumption accordingly. The

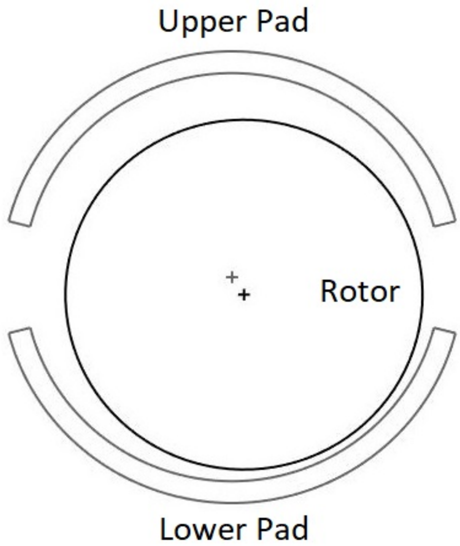

Figure 1: Cross section of rotor and pads of Fitzgerald and Neal's bearing [58]

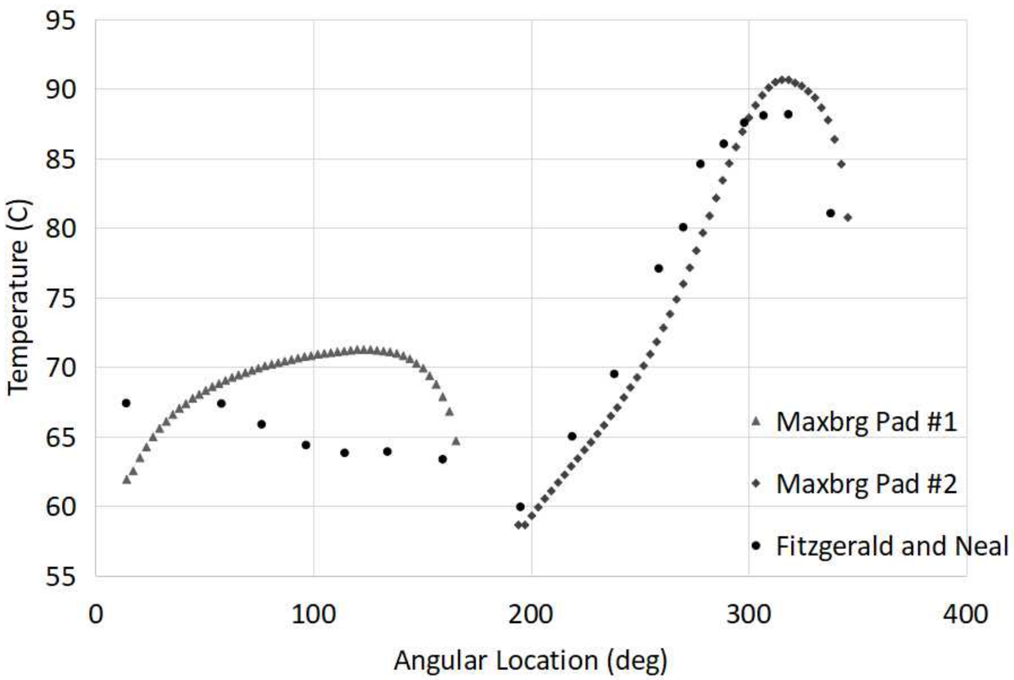

Figure 2: Comparison between experimental results[58] and 2-D TEHD solver

laminar assumption was used as the code predicted a maximum Reynolds number of 300. Comparisons of the pad surface temperature profile along the axial centerline between Fitzgerald and Neal [58] and MAXBRG can be seen in Figure 2. The results for the bottom pad agreed quite well, although MAXBRG did slightly overpredict the peak temperature.

The bottom pad is responsible for all of the load capacity of the bearing design. Therefore, only the bottom pad of the bearing was modeled with CFD. ANSYS CFX was used to perform the CFD analysis in this study. To validate the isothermal CFD model, the validated MAXBRG model was recalculated with an isothermal assumption and compared with the CFD results. The CFD model was assumed to be laminar due to the low Reynolds number. The axial centerline pressure comparison between CFD and MAXBRG can be seen in Figure 3. While the CFD model captured the overall shape of the pressure profile given by MAXBRG, the results had an approximate peak difference of 13%. This difference was the result of the assumptions used in the different equations that each method employed. One difference is that the Reynolds equation neglects all of the inertial terms. The density of the fluid was set to 1% of the actual density to remove the inertia from the CFD model for a better comparison. Excellent agreement can be seen between MAXBRG and the CFD results with negligible density in Figure 3. As the model was validated with MAXBRG, the inertia was added back into the CFD model. The inertia terms, in the normal density CFD model, will increase the load capacity of the bearing. These results agree with other studies [60, 61] on the influence of inertia in fluid-film bearings. It was concluded that the CFD model is an adequate approximation of the validated MAXBRG model, while also accounting for the inclusion of inertial effects on the flow, which is neglected in the Reynolds equation.

In Figure 3, negative pressure results are reported. In most bearings these negative pressures are not realistic as cavitation will occur. Modern CFD software can model this cavitation using a two-phase flow model. In this study, the cavitation was accounted for by reassigning negative pressure values to zero. This assumption is not particularly accurate in the region immediately prior to cavitation and introduces some small errors into the results. However, this method is very simple to use and allows for a greatly reduced run time when compared to a full two-phase simulation. This method is commonly used in literature [62] for this reason. Therefore, an assumption of zero pressures was chosen for its simplicity and was used in all of the following analyses.

After verifying the smooth bearing CFD model against the validated MAXBRG model, a jacking pocket was added to create a new CFD model. When a rectangular jacking pocket is machined into the surface of the pad,

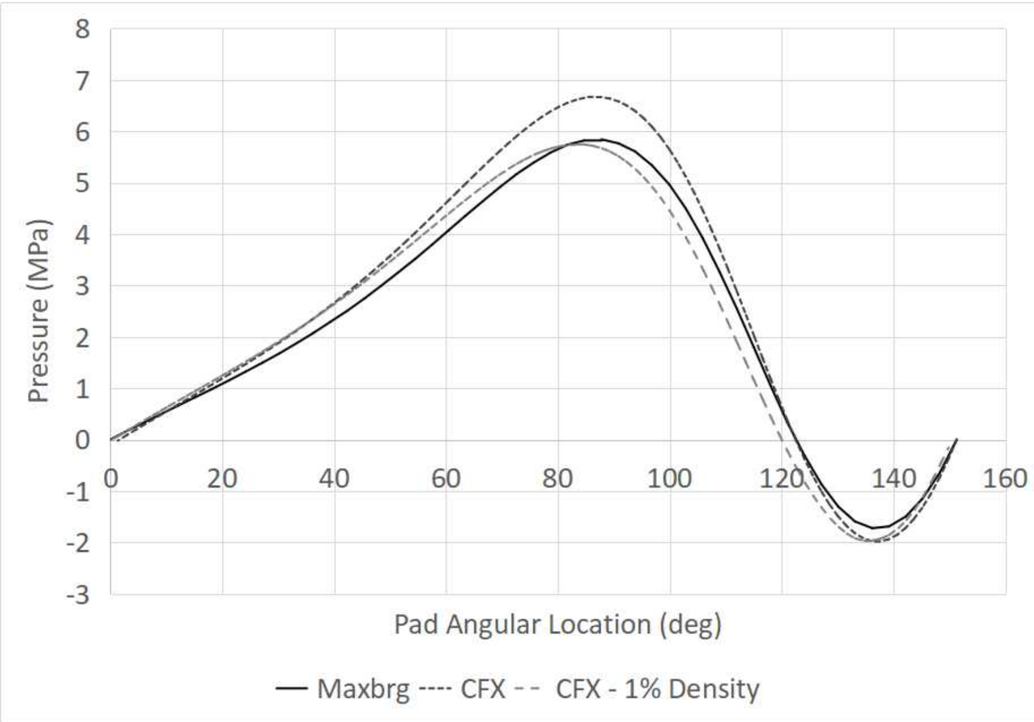

Figure 3: Comparison between CFD and 2-D TEHD solver

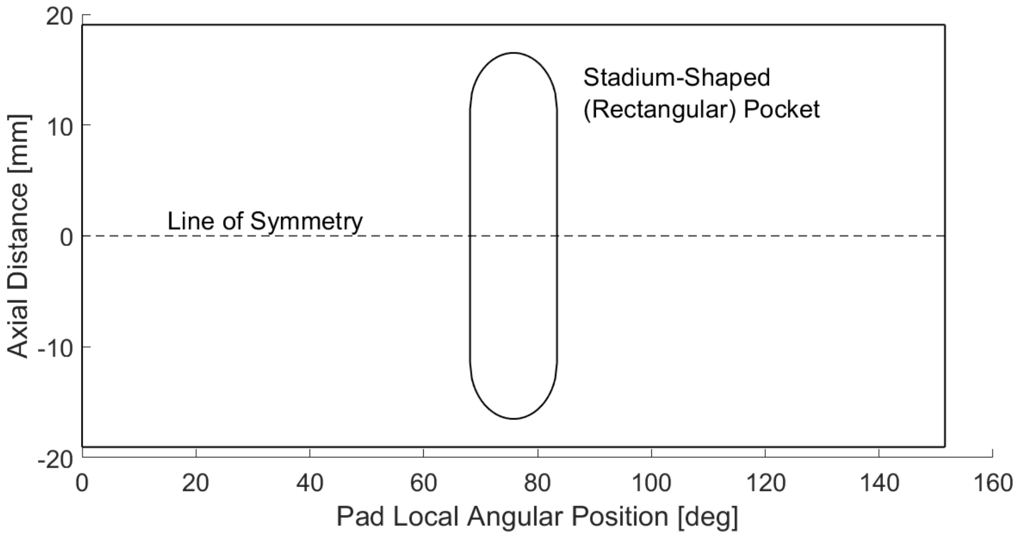

Figure 4: Two-dimensional view of bottom pad with stadium-shaped, jacking pocket geometry

the axial ends are often left as semicircles. This shape (rectangle with a semi-circle on either end) is known as stadium-shaped (also obround or discorectangular). This new CFD model was created with a parameterized, jacking pocket geometry. The jacking pocket was located axially-centered and circumferentially in-line with the direction of loading. For the sake of reducing the model size, axial symmetry is used in each of the CFD models in this study. Figure 4 shows a 2D representation of the full pad surface including the stadium-shaped pocket and the line of symmetry.

A mesh independence study was performed to ensure the accuracy of the CFD model. A stadium-shaped jacking pocket with an axial length of 17.78 mm (47% of the pad axial length) and a circumferential length of 12.7 mm (12% of the pad circumferential length) was chosen for the mesh independence study. A deep pocket of 10 times the bearing clearance was used. The journal eccentricity ratios were fixed at values given in Table 2. The number of cross film elements was varied from 20 elements to 50 elements and the number of cross pocket elements was varied from 15 elements to 100 elements. The results of the mesh independence study are shown in Table 3. The pressure profile changed negligibly when varied from the coarse mesh to the finer mesh. The 3 million element mesh was used to balance the computational costs with result accuracy.

Table 2: Fixed Eccentricity Values

x_j/C_b	0.4085
y_j/C_b	0.4508

Table 3: Mesh Independence Study

Number of Elements	Peak Pressure (MPa)	Percent Change (%)
225,000	5.88	-1.38
3,000,000	5.84	-0.61
9,000,000	5.80	-

2.3 Pocket Depth vs Pressure Profile Study

A study was performed to analyze the influence that the depth of the jacking pocket has on the centerline pressure profile. The journal eccentricity (Table 2) and jacking pocket length and width used were the same as for the mesh independence study. The depth of the pocket was varied from $0.01 \times C_b$ to $50 \times C_b$ over 36 levels. A selection of the resulting centerline pressure profiles can be seen in Figures 5-6.

Figure 5 shows the pressure with the jacking pocket depth varying from $0.01 \times C_b$ to $0.28 \times C_b$. As the pocket got deeper the pressure at the entrance to the jacking pocket decreased. The peak pressure increased by 30% and reached a maximum at the exit of the pocket. The pressure sharply increased across the pocket and then suddenly dropped after the trailing edge of the pocket.

Figure 6 shows the results as the pocket depth increases further to $6.6 \times C_b$. The peak pressure dropped, while the pressure reduction at the leading edge of the pocket disappeared. The pressure profile matches between the $6.6 \times C_b$ case and the smooth bearing up to the pocket leading edge. Beginning at the leading edge of the pocket, the pressure flattened until a jump occurs at the pocket's trailing edge. The pressure profile ceased to change as the pocket depth increased past $6.6 \times C_b$ (up to $50 \times C_b$). The lack of change occurring above $6.6 \times C_b$ is attributed to axial vorticies occurring in the pockets. An example of these vortices are shown in Figure 7. Vortices will fill up the larger pockets reducing the change to the jetstream flow. This trend agrees with an analytical study by Branagan [63] on the influence of scratch depths. The

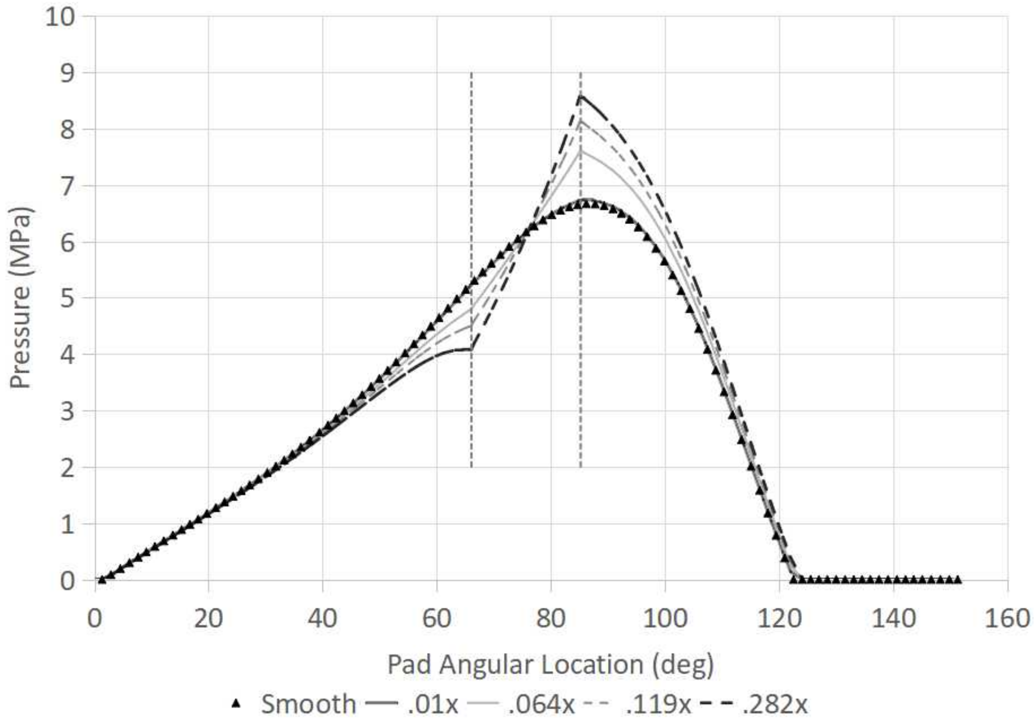

Figure 5: Centerline pressure for bearing with jacking pocket varying from $0.01 \times C_b$ to $.28 \times C_b$

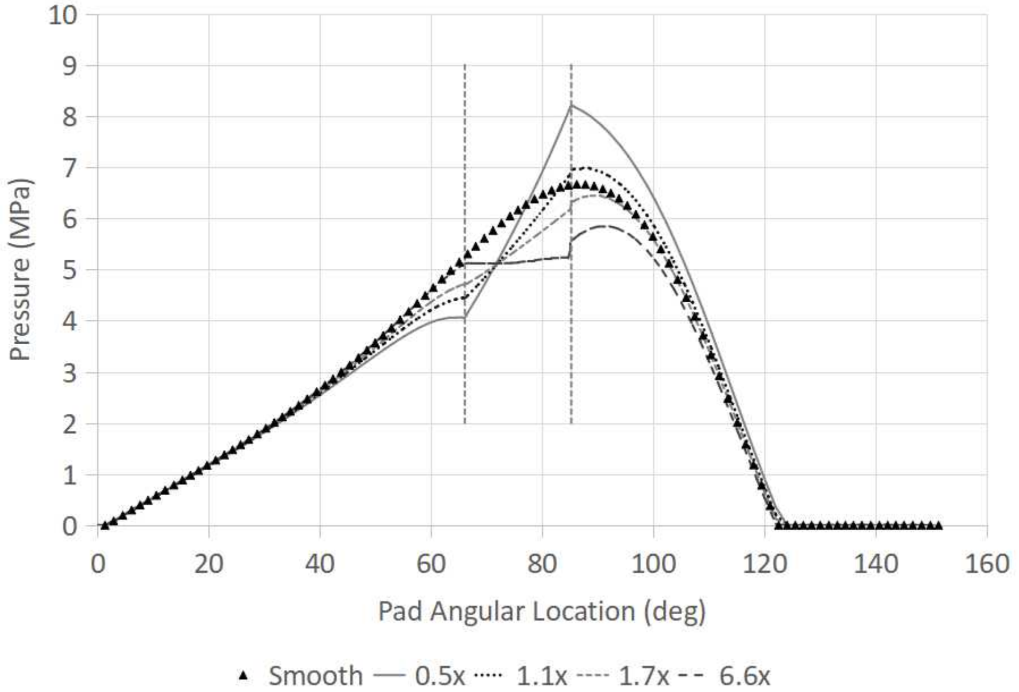

Figure 6: Centerline pressure for bearing with jacking pocket varying from $0.5 \times C_b$ to $6.6 \times C_b$

ratios of vertical force in bearings with and without jacking grooves are shown in Figure 8 as a function of pocket depth. Pockets with a depth of less than $1 \times C_b$ experience an increase in the vertical hydrodynamic force. The peak increase in vertical force occurs at $0.28 \times C_b$. A loss of vertical force occurs as the pocket depth increases, as would be expected from the reduction of the peak pressures seen in Figure 6. When the jacking pocket is deeper than $1 \times C_b$, the overall pressure generated by the pad was reduced. Pockets with a depth of $6.6 \times C_b$ and deeper generate 11% less vertical force than a smooth bearing. These results agree with the theoretical results seen in Heinrichson et. al. [15, 16]. They found that pockets less than $1.1 \times C_b$ contributed positively to the pressure generation, while deeper pockets inhibited it.

A simple hydrodynamic (HD) script was written using FreeFem++ which solves the laminar, isoviscous Reynolds equation given in Equation 2.1.

$$\frac{\partial}{\partial x}\left(\frac{\rho h^3}{12\mu}\frac{\partial p}{\partial x}\right) + \frac{\partial}{\partial y}\left(\frac{\rho h^3}{12\mu}\frac{\partial p}{\partial y}\right) = \frac{\rho U}{2}\frac{\partial h}{\partial x} \tag{2.1}$$

Figure 9 shows a side by side comparison of the CFD centerline pressure profile to that generated by the HD code with jacking pocket depths varying

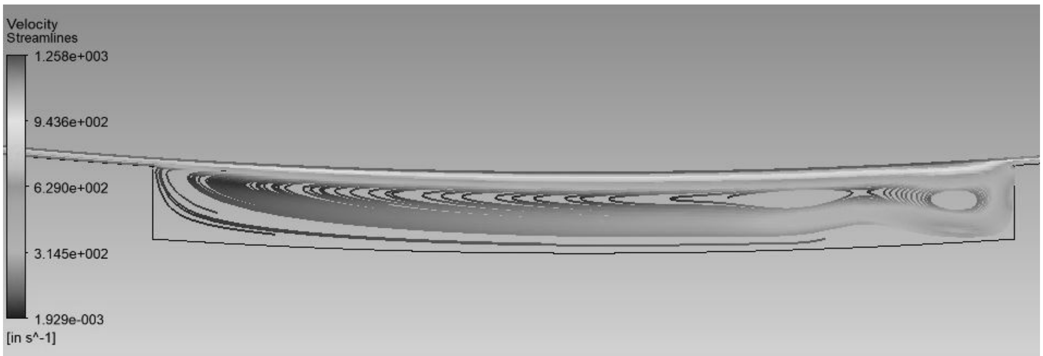

Figure 7: Streamlines along the centerline of pocket

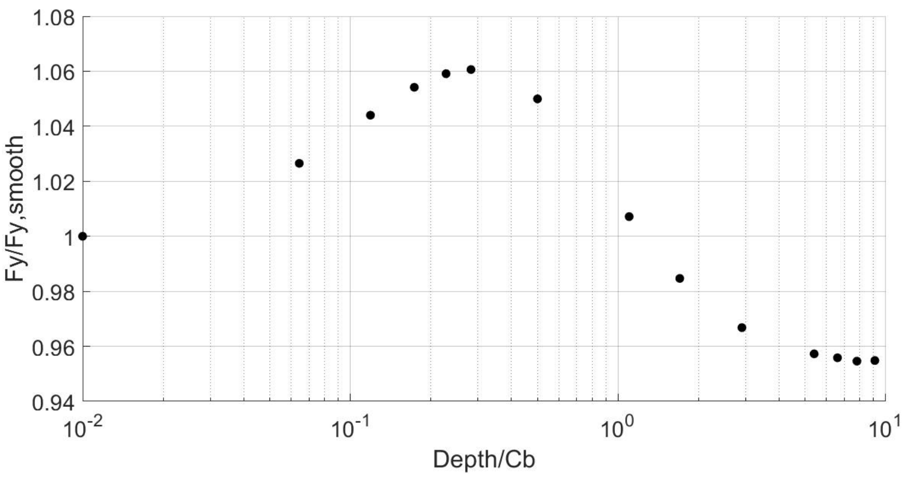

Figure 8: Ratio of vertical force of pad with pocket to smooth pad

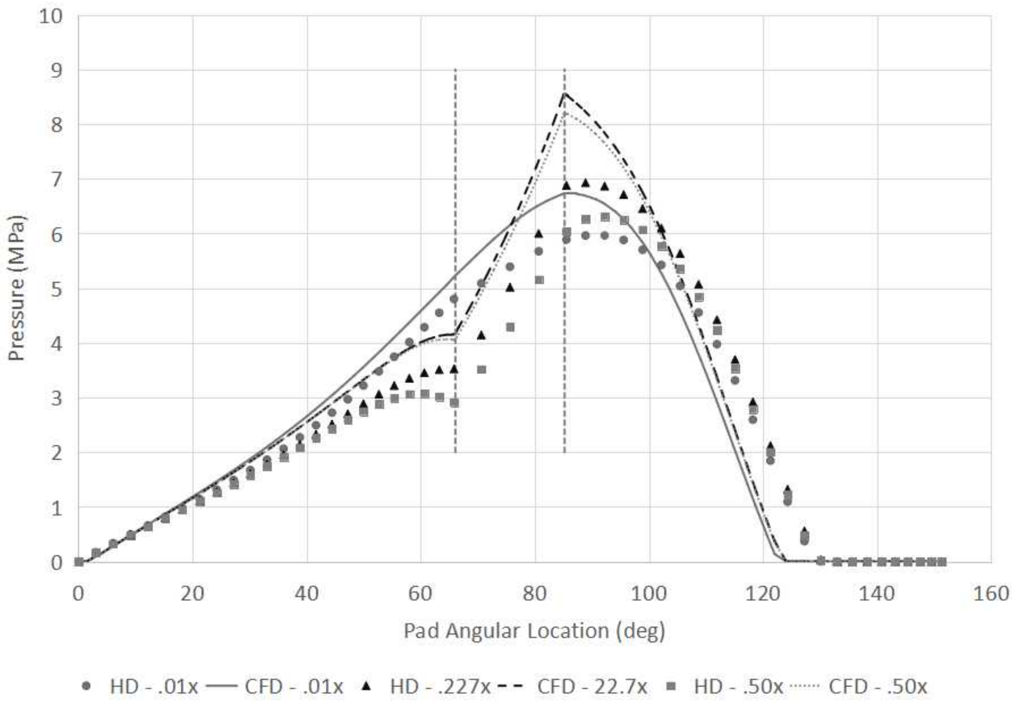

Figure 9: Comparison between CFD and HD pressure profiles for pockets between $0.01 \times C_b$ to $0.5 \times C_b$

from 1% to 50% of the radial clearance. As stated above, the Reynolds equation does not include the inertial terms which results in lower peak pressures [60, 61]. Therefore, while the HD code underpredicted the CFD results, the change in the shape of the curve is still the same. The pressure drop forms at the leading edge of the pocket, and the peak pressure increases. However as the jacking pocket depth is increased beyond 50% of the radial clearance, the results of the HD code begin to diverge from the CFD results. Relating to Figure 10, the pressure profile of the HD code does show a flat pressure profile across the pocket and a sharp increase at the trailing edge of the pocket at higher depths. However, the HD results also showed an overall increase in the pressure profile intensity with depth as also seen in Figure 10. The CFD pressure results ceased increasing after a depth of $6.6 \times C_b$. Based on this, it was hypothesized that at a depth of approximately $0.5 \times C_b$, the assumptions used in the Reynolds equation break down and this methodology is no longer a viable means of solving for the pressure across a jacking pocket.

Next another CFD study was performed by varying the circumferential length of the jacking pocket from 12% down to 1.2% of the pad circumfer-

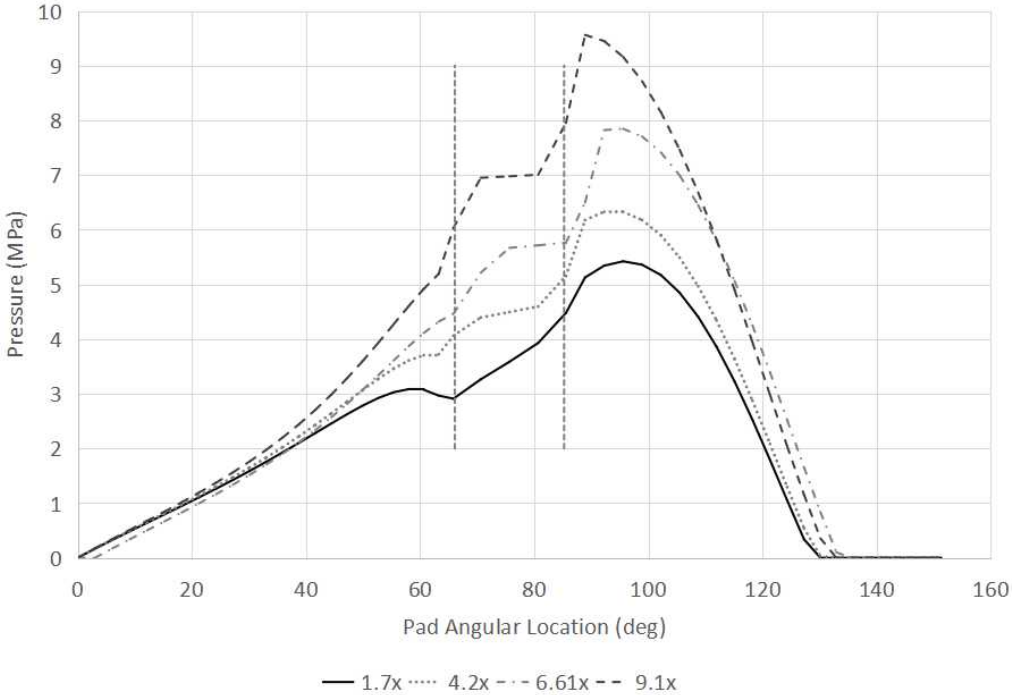

Figure 10: HD pressure profiles for pockets between $1.7 \times C_b$ to $9.1 \times C_b$

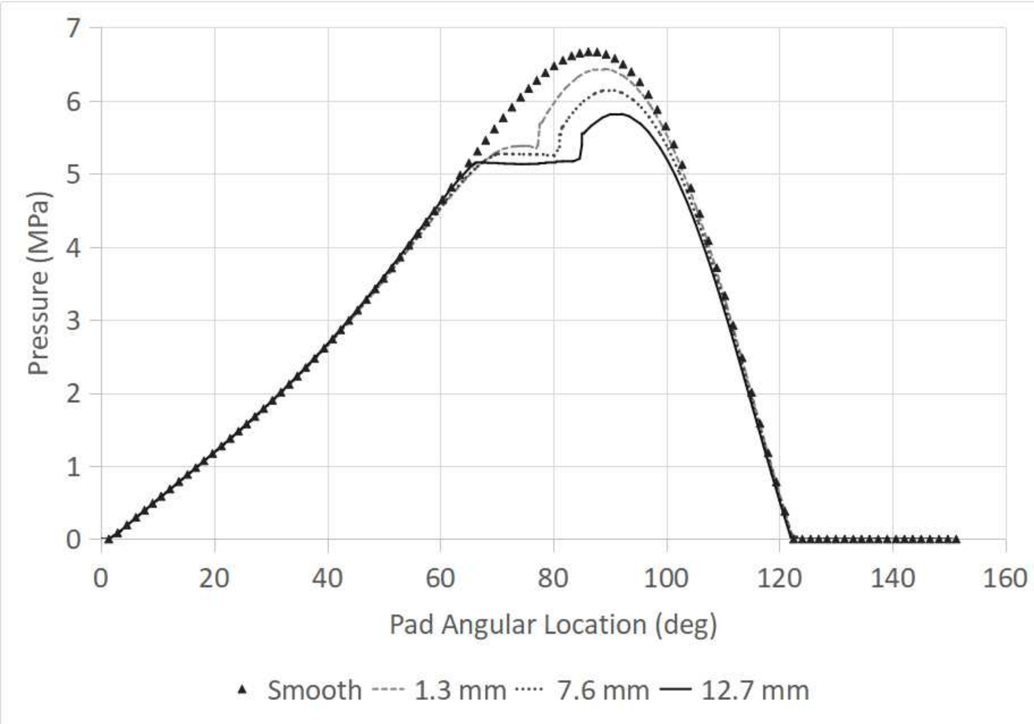

Figure 11: Centerline pressure for bearing with jacking pocket circumferential length varying from 100% to 10% of the initial pocket length of 12.7 mm

ential length over 10 levels. The same baseline hydrostatic jacking pocket geometry was used with the pocket depth being set to $10 \times C_b$. The centerline pressure of these simulations were compared with the smooth bearing case in Figure 11. Seen in Figure 11, as the pocket circumferential length is reduced, the pressure spike at the trailing edge of the pocket increases greatly while the pressure across the pocket increases slowly. Overall as the pocket length decreases, convergence to the smooth bearing case is observed

2.4 Design-of-Experiments and Linear Regression Models

An experimental design of CFD simulations was performed on the stadium-shaped jacking pocket to examine the influence of the pocket geometry on the operation and dynamic characteristics of the bearing. The three design parameters and their bounding values are presented in Table 4.

The seven responses examined in this study are the direct and cross coupled stiffness, power loss, eccentricity, and attitude angle. A central compos-

Table 4: Design Parameters

Parameters	Lower Bound	Upper Bound
d	$0.5 \times C_b$	$10 \times C_b$
l_a	33% $l_{a,pad}$	87% $l_{a,pad}$
l_c	5% $l_{c,pad}$	15% $l_{c,pad}$

ite (CC) design [64] was performed with 5 different levels (separate values for each parameter). The CC design was selected to allow the fitting of a response surface that could show curvature and include potential first order interaction effects between the three design variables. The CC design resulted in fifteen different design cases. Three of these fifteen points were found to be outliers based on the distribution of externally studentized residuals, across all of the responses, so three more points were added close to these to check the validity of outlying data points and improve the models' accuracy. In contrast with the prior studies, the equilibrium eccentricity position for each particular pocket geometry was found through iterating the CFD model geometry to balance the load with generated force. This was done using an optimization routine which minimized the sum of the external forces and the generated hydrodynamic forces using the Nelder-Mead algorithm [65]. All of the resultant sum of forces were reduced to less than 0.5% of the applied load. This process was worth while to ensure the improved understanding of actual running conditions. A perturbation method is used to calculate the stiffnesses for each pocket geometry. Cases were run with perturbation values set to 10%, 1%, and 0.1% of the bearing radial clearance. The perturbation size of 1% of C_b resulted in the lowest percent difference when compared with MAXBRG's (TEHD) stiffness calculation for the smooth case. Most of the difference resulted from how cavitation was handled. Lastly, power loss was calculated using Equation 2.2 on the journal surface with some modifications.

$$\xi = U \int_A \tau_s dA \tag{2.2}$$

Power loss is reduced in the cavitated region due to the air streamlets taking up space in the flow field. MAXBRG uses an equivalent, reduced bearing axial length method to account for the reduced power loss in the cavitated region. Multiple different eccentricities were tested for this bearing in MAXBRG and the equivalent bearing axial length varied minutely around $0.3 \times w_{pad}$. Therefore this value was used to account for the power loss reduction in the cavitated region in the CFD model. Lastly, to include the power

Table 5: Response Data Summary

Response	Units	Min.	Max.	Std. Dev.
K_{xx}	N/mm	1.09e5	1.42e5	2.87e3
K_{xy}	N/mm	2.41e4	2.61e4	190
K_{yx}	N/mm	-2.93e5	-2.60e5	4.50e3
K_{yy}	N/mm	1.06e5	1.12e5	1.34e3
ξ	W	1.12e3	1.15e3	4.25
e/C_b	-	0.56	0.61	3.12e-3
ϕ	degrees	44	47	0.37

loss on the top pad, MAXBRG was run at the same eccentricity as found through the CFD optimization and the power loss of the smooth top pad was added to that calculated from CFD of the bottom pad. The additional power loss from the top pad was an order of magnitude less than the bottom pad.

An overview of the response data is presented in Table 5. and can be compared with the responses of the smooth bearing presented in Table 6. In all cases, the jacking pocket caused a reduction in power loss. This agrees with Heinrichson's findings [14]. This was due to the reduction of the velocity gradient in the region of the pocket from an increase in local film thickness. However, the overall reduction in power loss was quite minimal. The jacking pockets also uniformily decreased the attitude angle. This trend was not unexpected, as the pocket tends to push the hydrodynamic load towards the leading edge of the pad. Therefore any change in the attitude angle will be back towards the pad trailing edge to balance the loads. Conversely, the eccentricity ratio was increased due to the reduction in the pressure profile caused by the pocket, resulting in a higher eccentricity ratio necessary to carry an equivalent load. The direct horizontal stiffness is also increased due to the presence of the pocket. The increased eccentricity results in a stiffer film.

A regression model was fitted for each response. Initially a full quadratic model with linear interaction terms was chosen. Then each term was evaluated for its statistical significance [66]. The R^2, adjusted R^2, and p-values for each model are reported in Table 7. An R^2 value is a measure of the model's ability to capture the variation in the response. An adjusted R^2 value is used to prevent statistically insignificant terms from artificially increasing the R^2 measure. Therefore, an adjusted R^2 value of 0.80 means that the

Table 6: Response Data for Smooth Bearing

Response	Units	Value
K_{xx}	N/mm	127200
K_{xy}	N/mm	24030
K_{yx}	N/mm	-277800
K_{yy}	N/mm	105700
ξ	W	1157
e/C_b	-	0.55
ϕ	degrees	47

Table 7: R^2 Values for Best Fit Linear Regression Models

Response	R^2	Adjusted R^2	p-Value
K_{xx}	0.88	0.83	9.6e-5
K_{xy}	0.92	0.90	2.9e-7
K_{yx}	0.79	0.69	2.0e-3
K_{yy}	0.52	0.48	1.2e-3
ξ	0.77	0.74	3.6e-6
e/C_b	0.96	0.95	1.6e-7
ϕ	0.61	0.55	1.4e-3

model is able to predict only 80% of the variation of the data. Conversely, this means that 20% of the variation cannot be explained by the model. The p-values in this chapter are the result of an ANOVA test comparing the value of the coefficient of each term to zero. The null hypothesis being that the coefficient is zero, which would suggest that the coefficient does not belong in the model. So a 0.05 p-value represents a 95 percent confidence that the coefficient is not equal to zero. This is not directly related to the relative strength of the correlation between the model and the response data, like an R^2 value. Instead, it is the likelihood that an individual coefficient, or the entire model of coefficients, found significance due to random chance. Each regression model was built up using forwards regression by adding coefficient terms based on their individual p-value. All of the models developed in this chapter had p-values below the standard limit for statistical significance of 0.05. The parameter coefficients for each model are reported in Tables 8 and 9.

Table 8: Regression model coefficients for power loss and eccentricity

	ξ	e/C_b	ϕ
A_1	1.14e3	1.72e-3	46.1
A_2	-985	5.93e-6	0.761
A_3	-22.6	1.03e-4	-0.869
A_4	-	2.17e-5	-
A_5	-	-3.40e-5	-
A_6	-	1.20e-4	-

Table 9: Regression model coefficients for stiffness coefficients

	K_{xx}	K_{xy}	K_{yx}	K_{yy}
A_1	1.23e5	2.50e4	-2.71e5	1.08e5
A_2	2.12e3	-519	-2.67e3	4.14e3
A_3	1.02e4	938	-9.99e3	-
A_4	-9.70e3	1.50e3	2.00e4	-
A_5	-1.25e4	-	-2.35e4	-
A_6	2.50e4	-	-3.47e4	-

Of all the responses, the direct horizontal stiffness showed the largest variability over the design range with a standard deviation of 5.5% and an overall change of 27% of the mean value. The smooth bearing response fell close to the center of this range. A reduced quadratic model, with pocket depth and axial length having the largest influences on the response, was selected to have the best fit. This model is defined in Equation 2.3.

$$K_{xx} = A_1 + A_2 d + A_3 l_a + A_4 l_c + A_5 d^2 + A_6 l_a^2 \tag{2.3}$$

The pocket depth's influence on the pressure profile explains its large influence on K_{xx}. The pocket depth's ability to both increase or decrease the peak pressure would help explain variation of K_{xx} about the smooth bearing case. Figure 12 shows the model prediction compared with the CFD data points. All of the data points fall close to the line and have no clear pattern of distribution about the line. This shows that the model is able to capture not only the major trends, but also capture most of the variation that occurs within this data set with relatively small errors. Figure 13 shows that the residuals match with the expected normal distribution of error between the model and the data points. Figures 14 and 15 depict some response surface plots using the regression model. From these plots, the quadratic shape of the model and some of the interaction effects between the different design parameters can be seen. Both of these figures show a distinct pocket axial length of 10 mm (26% of pad axial length) which results in the lowest horizontal stiffness. Figure 14 shows a pocket depth of 0.5 mm ($6.6xC_b$) which results in a maximum value of K_{xx}. These surface response plots can be useful tools in guiding engineers in refining their designs.

The direct vertical stiffness has a variability resulting in a standard deviation of 1.2% and a overall change of 5.8% of the mean value. The best fit model for K_{yy} was a simple linear model related only to the axial length of the pocket given in Equation 2.4.

$$K_{yy} = A_1 + A_2 l_a \tag{2.4}$$

This model was not very good. The adjusted R^2 value was 0.48 meaning that it is only predicting half of the variability in the data about its mean. However, the model did have a p-value of 1.2e-3 which is below the standard cutoff of 0.05 for statistical insignificance. This means that although the model doesn't capture all of the trends in the data, what is captured is relevant. As the axial length of the pocket increased, this model predicted a higher stiffness. As the axial length of the pocket is increased, the high pressure that occurs at the center of the bearing is distributed throughout the pocket. This will result in an increased pressure distribution directly

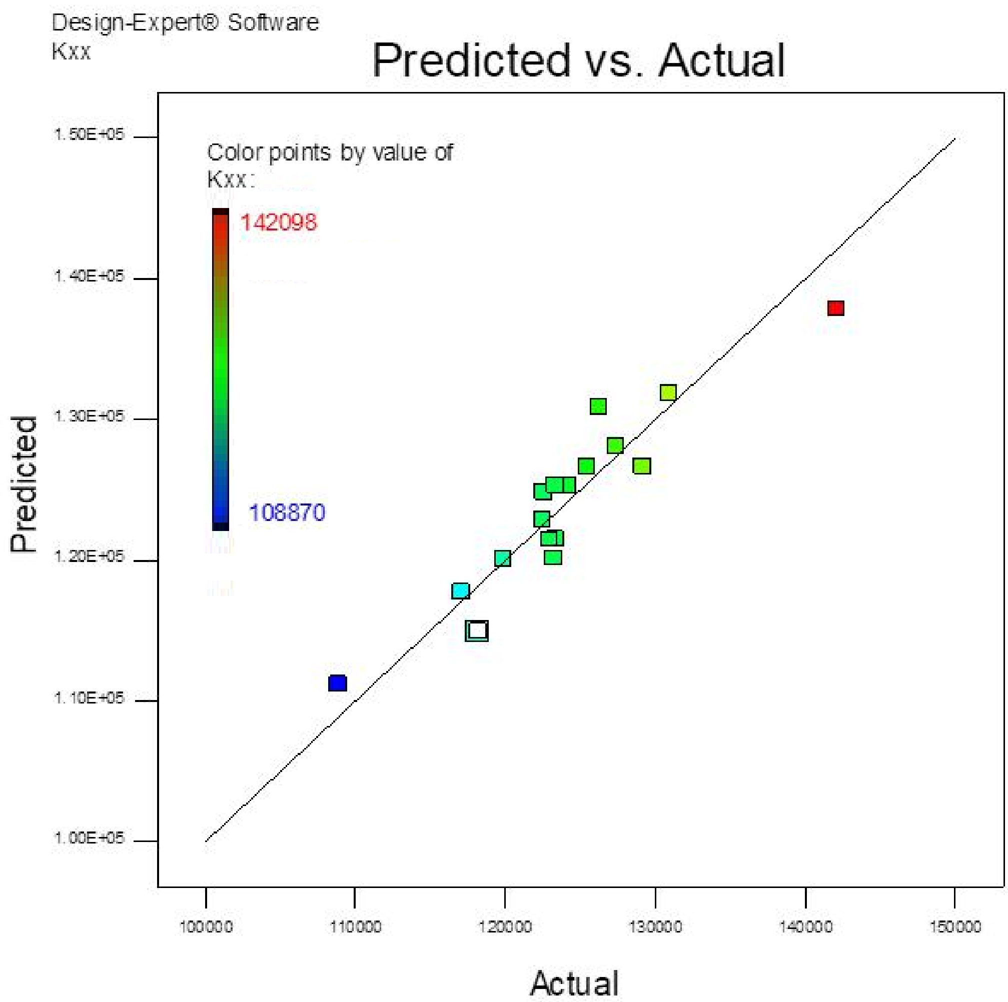

Figure 12: Plot of CFD data points compared with the K_{xx} model prediction

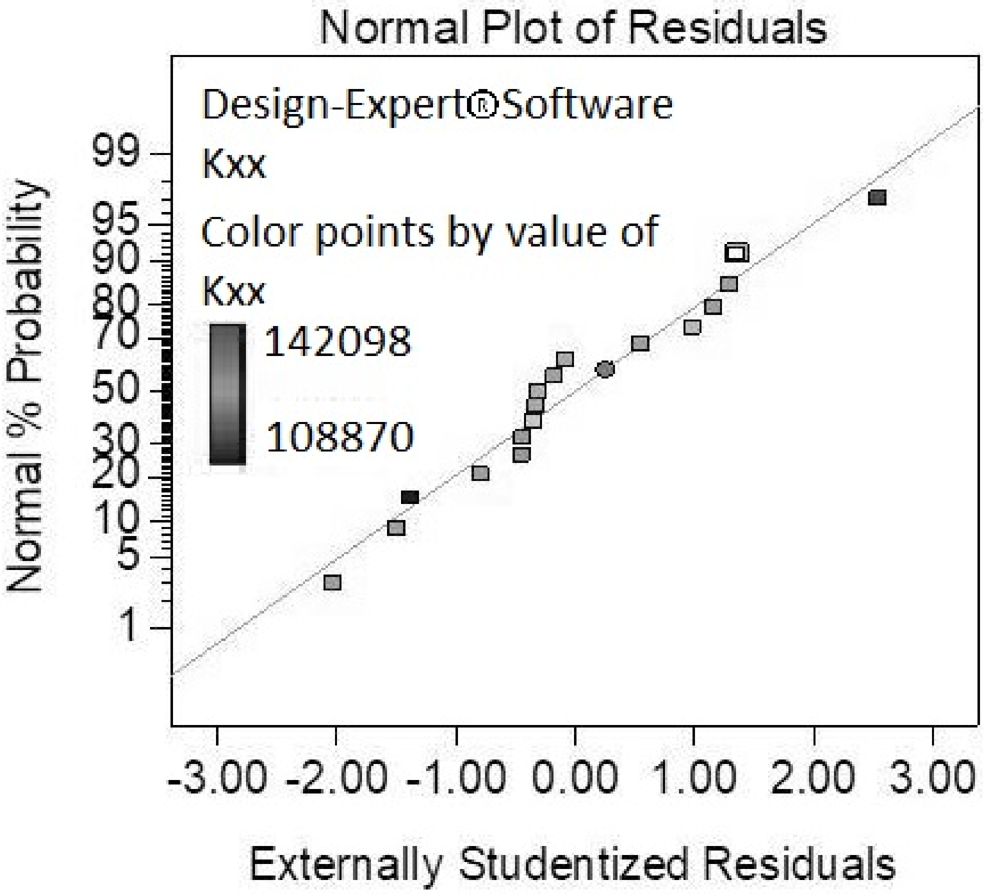

Figure 13: Plot of K_{xx} residuals compared with an expected normal distribution around the model prediction

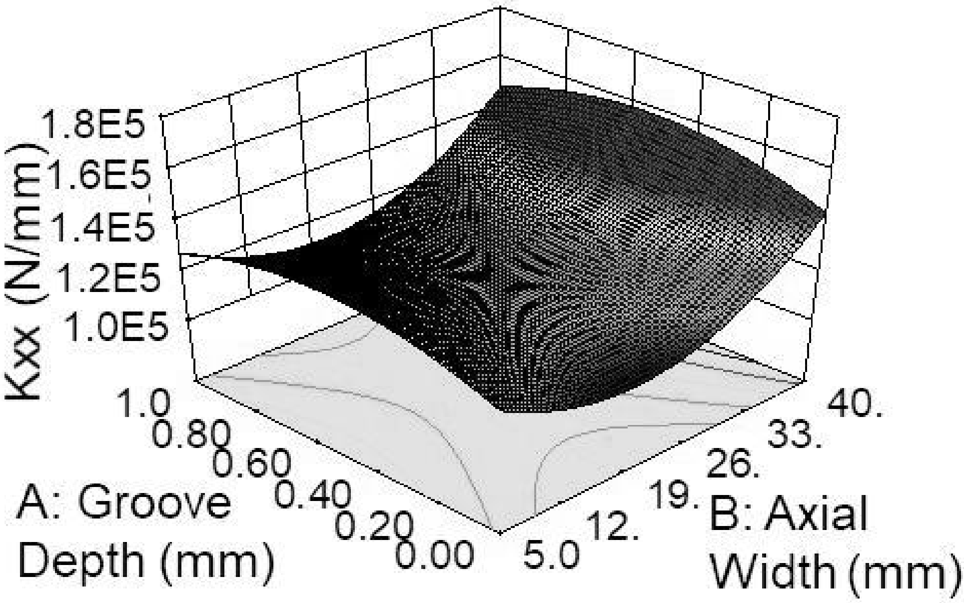

Figure 14: K_{xx} compared with pocket depth and axial width

underneath the rotor leading to an increase in the vertical stiffness. Figure 16 shows a plot of the predicted responses compared to the assumed normal distribution. The data on this plot seems to correspond to several different lines of varying slopes. A possible explanation for this could be the presence of several different flow regimes within the design space. Another hypothesis for the inadequacy of the model as a predictive tool is based on the vortices in the pocket. Figures 7, 17, and18 show vortices of varying size and orientation are occurring within the pockets of varying geometries. These complex flows present a challenge to fitting a linear model to the direct vertical stiffness. Owing to the location of the pocket, the stiffness of these complex pocket flows are directly included in K_{yy}. This hypothesis could also explain the presence of varying lines in Figure 16. While this model is able to demonstrate the rough trend in the data, it needs significant improvements to be a useful design tool. One possible means of improving the model is by redefining the relationship of the design variables and the K_{yy} response. Another alternative is by expanding the number of data points and developing multiple higher complexity models.

K_{xy} was fit with the full linear model given in Equation 2.5.

$$K_{xy} = A_1 + A_2 d + A_3 l_a + A_4 l_c \tag{2.5}$$

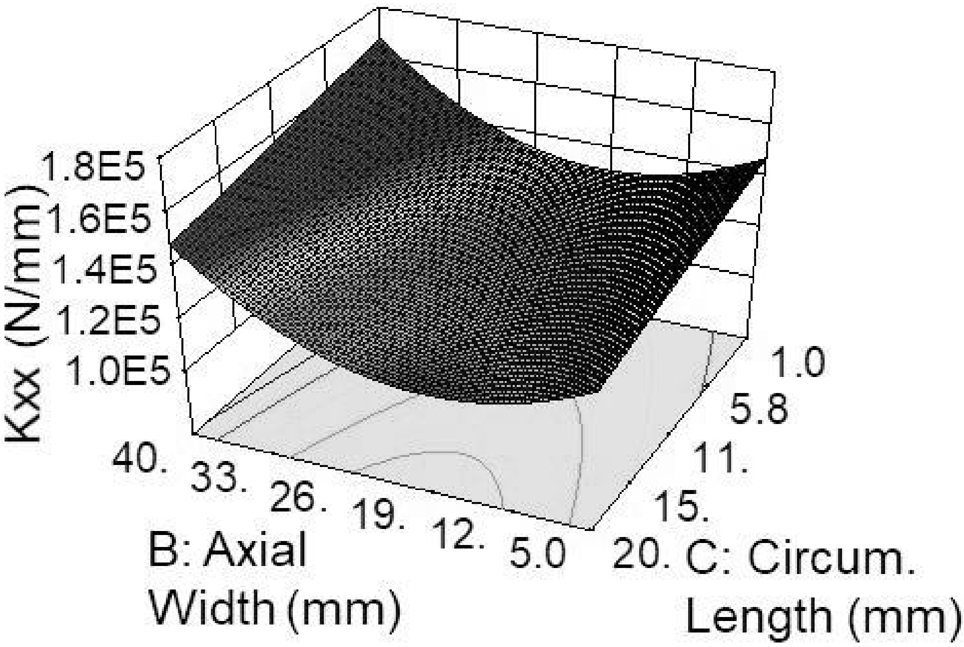

Figure 15: K_{xx} with varying axial length and circumferential length of the pocket

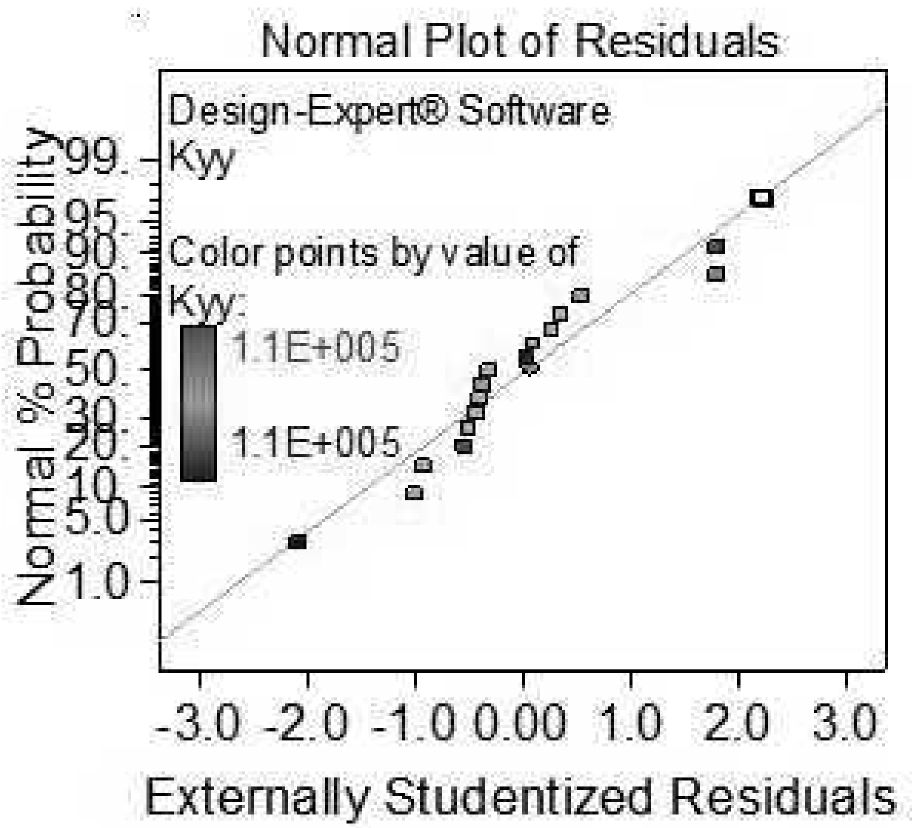

Figure 16: Plot of K_{yy} residuals compared with an expected normal distribution around the model prediction

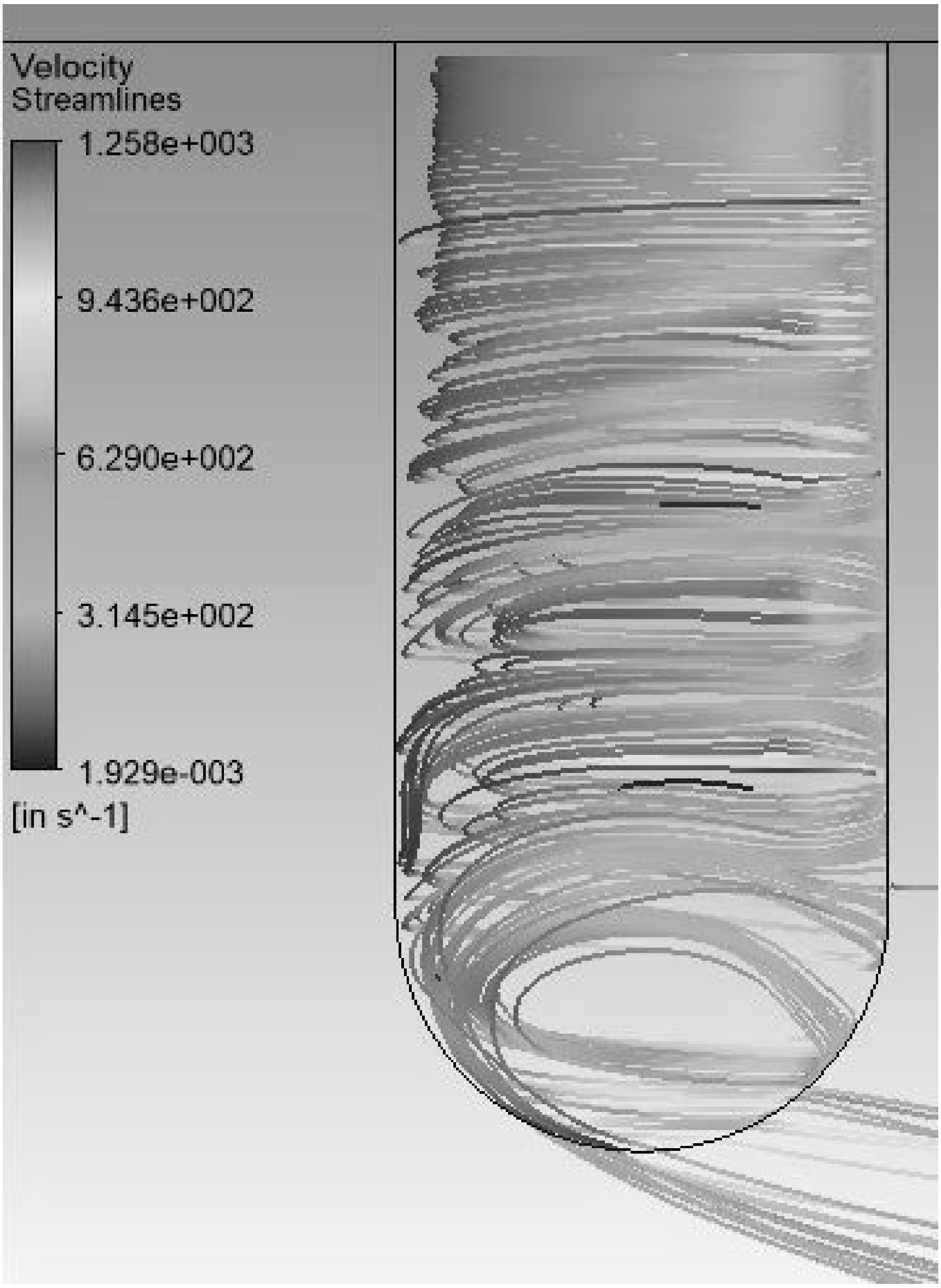

Figure 17: Overhead view of streamlines in pocket

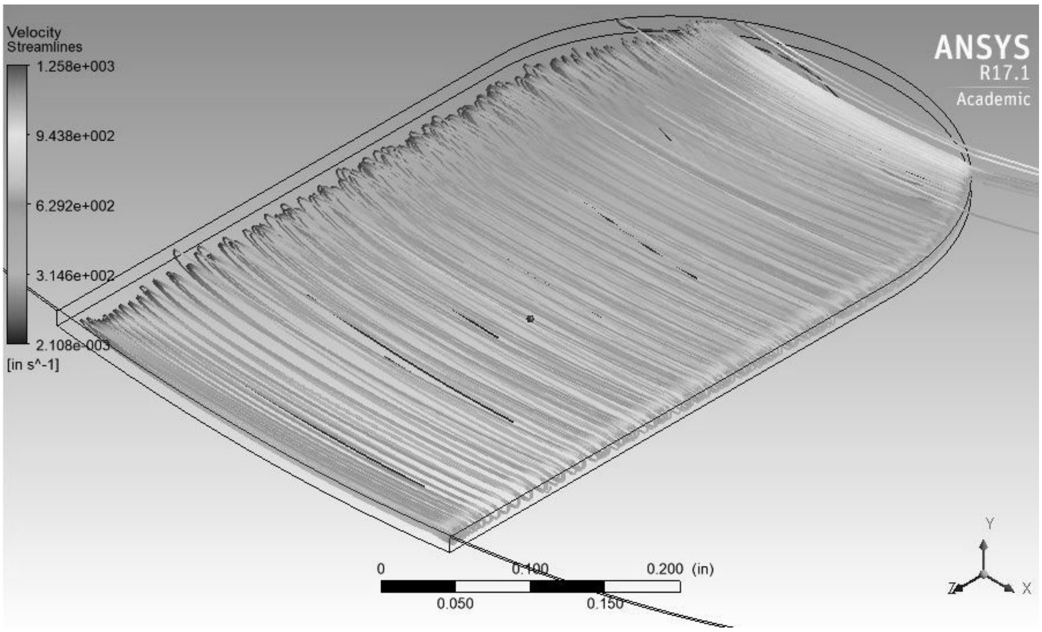

Figure 18: Isoparametric view of streamlines in pocket

This model explained 92% of the data's variation about its mean, thus capturing all of the major trends in the data. K_{yx} was fit with a linear model which included a linear interaction term between pocket depth and pocket axial length (Equation 2.6).

$$K_{yx} = A_1 + A_2 d + A_3 l_a + A_4 l_c + A_5 d l_a + A_6 l_a^2 \tag{2.6}$$

This model, while capturing the general trends, failed to capture all of the variability of the data points. This can be seen by its low adjusted R^2 value of 0.69. However, the p-value of this model was 2.0e-3 which means it is statistically relevant. Although the model has a low adjusted R^2 value, the relationships that it does contain are valid. All of the coefficients of this model are negative except for A_4. The circumferential length of the pocket increases this cross coupling term towards positive. There are several higher order terms that include the pocket axial length. This axially expanded pocket will distribute the high pressure oil farther out. Similar to K_{yy}, the complexity of the pocket flow makes accurately modeling K_{yx} significantly more challenging. Therefore more data would be required to improve this model.

The eccentricity ratio varies by just 6% of the radial clearance. The resulting regression model for eccentricity ratio is the reduced quadratic equation given in Equation 2.7.

$$\frac{e}{C_b} = A_1 + A_2 d + A_3 l_a + A_4 l_c + A_5 d^2 + A_6 l_a^2 \tag{2.7}$$

The absence of the pocket circumferential length quadratic term from this model can best be explained due to the upper limit imposed in this study. The pocket was limited to a maximum circumferential length of 12.7% of the pad's length. Due to this upper constraint, the circumferential length was limited to a smaller range. This likely kept the pocket influence constrained to a linear relationship. It would be valuable to expand the range of this design variable to see if this linear relationship would break down. The pocket was also limited to the converging portion of the fluid-film. It might also be worth examining some cases with larger circumferential pocket lengths. The relationship to circumferential length would likely require a more complex model. The pocket axial length is allowed to cover between 33% and 87% of the pad axial length. The size of this range lends itself to requiring a more complex model. The attitude angle didn't vary greatly over the whole range. The attitude angle had a 3° variation across all of the different geometries (including the smooth pad). The reason for the lack of response may be related to the bearing loading. As fixed-geometry, journal bearings are loaded, the equilibrium position would follow an arc traveling towards the leading edge of the pad [67]. If this bearing is in the light to medium loaded range of this arc, then changing the shape of the pressure profile won't have as strong of an influence. The chosen model has a low adjusted R^2 value of 0.55 but a p-value of 1.4e-3 and is given in Equation 2.8.

$$\phi = A_1 + A_2 d + A_3 l_a \tag{2.8}$$

The pocket depth will increase the attitude angle while the axial length will decrease it. One reason for the poor adjusted R^2 value could be due to the small size of the range of the responses. The numerical error from the eccentricity optimization solution may have had an increased contribution to the variability of this data. However, the eccentricity ratio had an adjusted R^2 value of 0.95 which disagrees with any numerical error from the optimization search. There is a possibility that the eccentricity ratio model is being overfitted. More data points would be required to further validate the model and test the numerical error hypothesis.

As mentioned earlier, the geometry and depth of the stadium shaped pocket have minimal influence on the power loss of the bearing. This response varied up to a 2.9% reduction of the smooth bearing's power loss across the entire range of pocket designs. The best fit model for modelling the power loss was a reduced linear model (Equation 2.9).

$$\xi = A_1 + A_2 d + A_4 l_c \tag{2.9}$$

This model had an adjusted R^2 value of 0.74. This model is adequate for general trends but could likely be improved with additional data points. An increase in pocket circumferential length or depth were both found to cause a reduction in power loss. The increased depth would result in a lower velocity gradient at the shaft surface causing a reduction in power loss. The axial length of the pocket was found to have statistically negligible effect on the power loss. This absence was unexpected as the increased area of the pocket would be expected to decrease the velocity gradient, and thus the shear stress, on the surface of the rotor. Owing to the stadium-shape, vorticity in the loading direction occurs in both of the axial edges of the pocket as shown in Figure 17. The size of these vortices is strongly related to the circumferential length of the pocket, as this defines the radius of the end semi-circles. The current hypothesis is that the influence of these vortices on the power loss is much stronger than the increased area of the pocket. These vortices may also help to explain the power loss reduction found above and in Heinrichson [14]. These hypotheses were not explored in this study and is an area requiring further research.

2.5 Conclusions

In this study a CFD model was developed for a fluid-film bearing with stadium-shaped jacking pocket. The model was validated using experimental results and a TEHD code. Then a stadium-shaped jacking pocket was added to the bearing and the pocket circumferential length, axial length, and depth were all allowed to vary. The influence of pocket depth and circumferential length was examined individually using CFD. Then design-of-experiment and linear, regression models were used to examine each of the parameters and any interaction effects.

As pocket depths increased, the pressure profile transitioned between two regimes before achieving a steady pressure profile for deep pockets. Pocket depths up to 30% of the radial clearance will cause an increase in the load capacity of the bearing and cause a 6% increase in the vertical load. As the depth increased, the pressure profile shifted. The pressure became constant across the pocket and a spike in pressure occurred behind the trailing edge of the pocket. This transition to a deep pocket completed at a pocket depth of about $7xC_b$. These deep pockets experienced a 5% drop in the vertical force generated by the bearing. Similar pressure profile shapes (with a reduced pressure due to inertial effects) were achieved by solving the Reynolds equation. This held true for depths up to $0.5 \times C_b$. This Reynolds solution breaks down for pockets deeper than this.

As the circumferential length of a deep pocket ($10 \times C_b$) decreased, the pressure profile approached that of a smooth bearing. This means that circumferentially thin pockets should have a very minimal influence on the performance of a bearing.

The stadium-shaped, jacking pocket geometry did not have a strong influence on most of the responses examined in this study. The pocket had the largest influence on the stiffness characteristics of the bearing with K_{xx} varying up to 25%. Such a large variation in K_{xx} could have a significant influence on the operating characteristics of the machine. A quadratic, linear, regression model was created for this response which was able to quite accurately cover the design space. The K_{yy} response was much more difficult to model. The reason for this may have been due to the complexity of the various flows within the pocket itself. This complexity makes the empirical modeling of the direct stiffness in line with the pocket extremely challenging. Adding additional data points and higher order models may be required to better capture this response.

This study is the first to examine how each aspect of a jacking pocket's geometry influence the operation and linear stiffness values of a fluid-film journal bearing. It examined the applicability of the Reynolds equation to solving these problems and presented some issues that can arise. It also provides valuable data which can be used for further verification and validation in future studies.

These jacking pockets did have an influence on the generated vertical forces and the stiffness characteristics of the bearing. In most cases these bearing features won't significantly compromise the overall bearing performance. However, for heavily loaded bearings with narrow safety margins and for highly sensitive machines, understanding the influence of these features on the specific design could be crucial to success. The direct horizontal stiffness of the bearing did experience a signficant variation depending on the pocket geometry. Understanding this variation can be important to the safe operation of these machines, especially if subjected to any horizontal loading.

3 Hydrodynamic Performance Characteristics of a Fluid-Film Journal Bearing with Jacking Features

Nomenclature

P Pressure
x Circumferential coordinate
C_b Bearing radial clearance
d_g Depth of diamond-shaped, jacking pockets
$\bar{d}_g$ d_g/C_b
$d_{f,g}$ Depth of hourglass-shaped, jacking groove
$\bar{d}_{f,g}$ $d_{f,g}/C_b$
$d_{f,l}$ Depth of land region inside of hourglass-shaped, jacking groove
$\bar{d}_{f,l}$ $d_{f,l}/d_{f,g}$
$l_{dd,a}$ Axial length of diamond-shaped, jacking pockets
$\bar{l}_{dd,a}$ $l_{dd,a}/l_m$
$l_{dd,c}$ Circumferential length of diamond-shaped, jacking pockets
$\bar{l}_{dd,c}$ $l_{dd,c}/l_{p,c}$
$l_{f,a}$ Axial length of hourglass-shaped, jacking groove
$\bar{l}_{f,a}$ $l_{f,a}/l_{p,a}$
$l_{f,c}$ Circumferential length of hourglass-shaped, jacking groove
$\bar{l}_{f,c}$ $l_{f,c}/l_{p,c}$
l_m Distance from diamond-shaped, jacking pocket outer corner to pad, axial center
$\bar{l}_m$ $l_m/l_{p,a}$
$l_{p,a}$ Axial length of the pad
$l_{p,c}$ Circumferential length of the pad
w_f Width of hourglass-shaped, jacking groove
$\bar{w}_f$ w_f/C_b

3.1 Introduction

For many rotordynamic machines, the bearings are often among the cheaper components. Therefore, many bearing surfaces are composed of softer material than the journal to protect the rotor from damage on contact, such as during startup or shutdown or incidental contact while running. Heavy rotors can cause damage to the soft surface materials of supporting bearings during machine startup or shutdown. The journal and bearing surfaces will travel through several different friction regimes before the film can generate enough pressure hydrodynamically to fully support the gravity load of the rotor. Prior to this, the bearing operates in the boundary or mixed lubrication regimes which have significantly higher coefficients of friction than the fully hydrodynamic regime. The high friction coupled with the heavy loads can cause extreme damage to the soft bearing surfaces. The surface of these bearings are designed to include jacking pockets or grooves to support the rotor and protect the bearing surfaces during these operations. These are machined into the face of the bearing and are connected to a feed port which is in turn connected to a high pressure oil supply. The machined jacking feature is used to distribute this oil to a large area under the rotor and support the high loads hydrostatically. This function is vital for successful operation at low speeds. Often the high pressure oil is shut off once the rotor speed is adequate to support the bearing loads hydrodynamically.

There have been an array of studies performed on these features under hydrostatic and mixed conditions. A variety of assumptions (ignored [8], smooth pad [8], Reynolds equation [9, 10]) are made to account for the hydrodynamic operation in these papers, and adequate justifications are not presented in their defense. There are also several different studies performed on thrust bearings with various jacking features [14, 15, 16, 18, 19, 20]. There have been a limited number of studies on the influence of jacking features on the operation of journal bearings. A computational fluid dynamics (CFD) study (Chapter 2) was performed on the effects of the geometry of a stadium-shaped, jacking pocket on operational and dynamic bearing characteristics. The pocket depth was varied between $0.01 \times C_b - 50 \times C_b$. The resulting hydrodynamic load was found to increase by 11% of the smooth case for a pocket depth of $0.28 \times C_b$. The load decreases as the depth of the pocket increases past this point. The hydrodynamic load reaches 6% less than the smooth case for bearings with pocket depths of $6.7 \times C_b$ or greater.

This chapter presents an extension of Chapter 2 by including two additional jacking feature geometries. The two geometries selected for this study were a pair of diamond-shaped pockets and a hourglass-shaped groove. Some initial studies were performed on these different geometries examining the influence of particular aspects of their geometries with a fixed journal position. The depth of both geometries was varied in a similar manner as the stadium-shaped pocket study. The width of the hourglass-shaped groove was also varied to better understand the transition between pockets and grooves. Then separate design-of-experiments were performed for both jacking features. The influence of the different aspects of the jacking features' geometries on the power loss, journal static eccentricity position, and direct and cross-coupled stiffnesses were examined. Linear regression models were developed for each response for each feature and the relationships are discussed in terms of the physics. This study expands upon the novel study performed in Chapter 2 by including two additional jacking features.

The objectives for this chapter were to:

1. Develop a model of a fluid-film bearing with a pair of double diamond, jacking pockets and use this model to
   (a) Develop an understanding of how the depth of the pocket influences the
      - Pressure profile throughout the film
   (b) Understand how the different aspects of the geometry of the pair of double diamond pockets (axial length, circumferential length, axial distance from centerline, pocket depth) influence the
      - The direct (K_{xx} and K_{yy}) and cross-coupled (K_{xy} and K_{yx}) stiffnesses
      - Power loss
      - Journal equilibrium position (eccentricity ratio and attitude angle)
   (c) Develop models for each of these outputs
2. Develop a model of a fluid-film bearing with a hourglass-shaped, jacking groove and use this model to
   (a) Develop an understanding of how the depth of the pocket influences the
      - Pressure profile throughout the film
   (b) Develop an understanding of how the groove width of the pocket influences the pressure profile throughout the film
   (c) Understand how the different aspects of the hourglass-shaped groove geometry (axial length, circumferential length, groove width, groove depth, contained land area depth) influence the
      - The direct (K_{xx} and K_{yy}) and cross-coupled (K_{xy} and K_{yx}) stiffnesses
      - Power loss
      - Journal equilibrium position (eccentricity ratio and attitude angle)
   (d) Develop models for each of these outputs
3. Compare the results of both of these models with the results from Chapter 2

3.2 Bearing Model

The bearing used in this study was selected from the experimental study of Fitzgerald and Neal [58]. The bearing is a two-pad, fixed-geometry bearing. Table 10 contains the bearing geometry and operating conditions. The base CFD model without a jacking feature was validated in our previous study in Chapter 2. The bottom pad is the predominant contributor to the bearing operation due to the orientation of the loading and the angular size of each of the pads. Therefore, only the bottom pad was modeled to reduce the computational time of the simulations. The maximum Reynolds number was ~ 300 so a laminar assumption was used for all the simulations in this chapter.

When the thickness of the film diverges after the location of minimum film thickness, the volume of oil in the film is insufficient to fill up the whole volume. Several studies were performed and found that the oil breaks up into streamlets with dissolved gases filling in the open channels [68]. In bearing applications, this process is known as cavitation. Modern CFD codes have the ability to perform complex two-phase flows to model the cavitation. The downside of these methods is the large increase in simulation runtimes. An extremely simple method of accounting for caviation is to assume that all negative pressure results are zero. This method does introduce some error into the simulation as mass flow rate at the beginning of the cavitated region is not preserved. While less accurate, this model was chosen for its modeling simplicity and reduced simulation time, and the amount of error introduced by this simplification is fairly small. This method has been commonly used in literature [62]. Axial symmetry was also used for all of the simulations in this study to reduce the size of the models.

3.3 Double Diamond Jacking Pockets

3.3.1 CFD Model

The first jacking feature that was examined was a pair of diamond-shaped, jacking pockets. Figure 19 shows a representation of the full pad with the double diamond pockets, as well as the axis of symmetry. These pockets are equidistant from the axial center of the bearing and are circumferentially in-line with the direction of loading. Both pockets have the same geometry. The defining characteristics for the geometry and location of the jacking feature are the pocket circumferential length ($l_{dd,c}$), the axial length of a single pocket ($l_{dd,a}$), the distance from the pocket outer most, axial corner to the plane of symmetry (l_m), and the pocket depth (d_g). All of these parameters are shown in Figure 19, aside from the pocket depth. Each of these variables was

Table 10: Fitzgerald and Neal [58] bearing geometry

Journal Diameter	mm	76.2
Axial Length	mm	38.1
Pad Thickness	mm	9.5
Radial Cb	mm	0.076
Pad Arc Length	deg	151.3
Preload		0.0
Offset		0.5
Shell Heat Conductivity	W/m-°C	50
Lubricant Density	kg/m	855
Lubricant Specific Heat	J/kg-°C	1952
Lubricant Heat Conductivity	W /m-°C	0.15
Lubricant Viscosity at 40 °C	Pa-s	0.028
Lubricant Viscosity at 99 °C	Pa-s	0.0047
Lubricant Supply Temperature	°C	50
Shaft Speed	rpm	8000
Load	kN	5.43

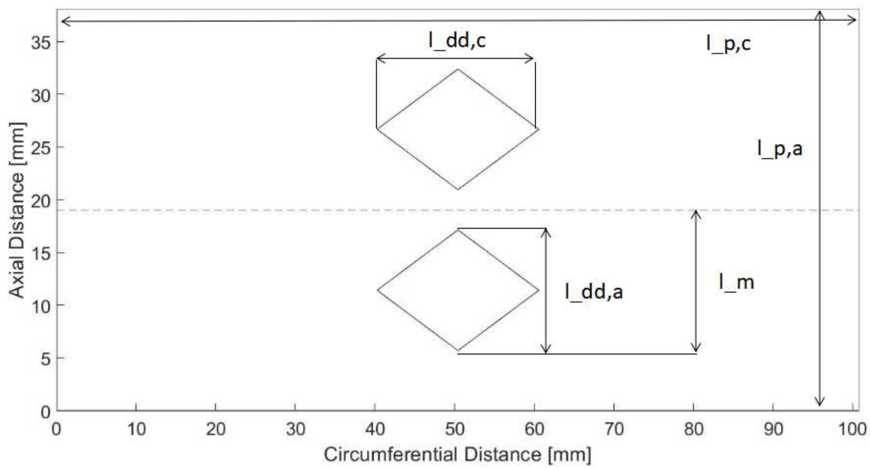

Figure 19: Pad and double diamond pocket geometries

nondimensionalized for use in this study. The nondimensional equations are presented in the Nomenclature.

To balance simulation run time and accuracy of the results, a mesh density study was performed. The representative geometry of the double diamond

Table 11: Mesh Independence Design Parameters

$\bar{d}_g$	16.5
$\bar{l}_{dd,c}$	0.126
$\bar{l}_{dd,a}$	0.682
$\bar{l}_m$	0.733
x_j/C_b	0.4085
y_j/C_b	0.4508

Table 12: Double Diamond Mesh Density Information

Number of Elements	Vertical Load	Percent Difference
-	kN	%
5.91e5	3.01	3.8
1.01e6	3.08	1.4
3.71e6	3.12	0.22
8.21e6	3.12	0

pockets used for the mesh testing are given in Table 11, along with the journal eccentricity. This eccentricity was chosen as it was the equilibrium position for the case with a smooth pad. Four different mesh densities were investigated. The resulting vertical loads are presented in Table 12, along with the number of elements in each mesh. The 1 million element mesh was chosen for this study as it allowed for a low run time with minimal losses in accuracy.

3.3.2 Pocket Depth vs Pressure Profile Study

The influence of the depth of the double diamond, jacking pockets on the centerline pressure profile and the vertical hydrodynamic force on the shaft was examined. The same jacking pocket geometry and shaft eccentricity that was used in the mesh independence study was used in this examination. The nondimensional depth of the pocket was varied from 0.01 to 50 while the rest of the pocket geometry was held constant. Figure 20 shows the bearing centerline pressure profiles for a $\overline{d_g}$ varying from 0.01 to 0.29. The pressure immediately proceeding and in the first half of the pocket decreased as the pocket depth increased. Following this region, a sharp rise in pressure

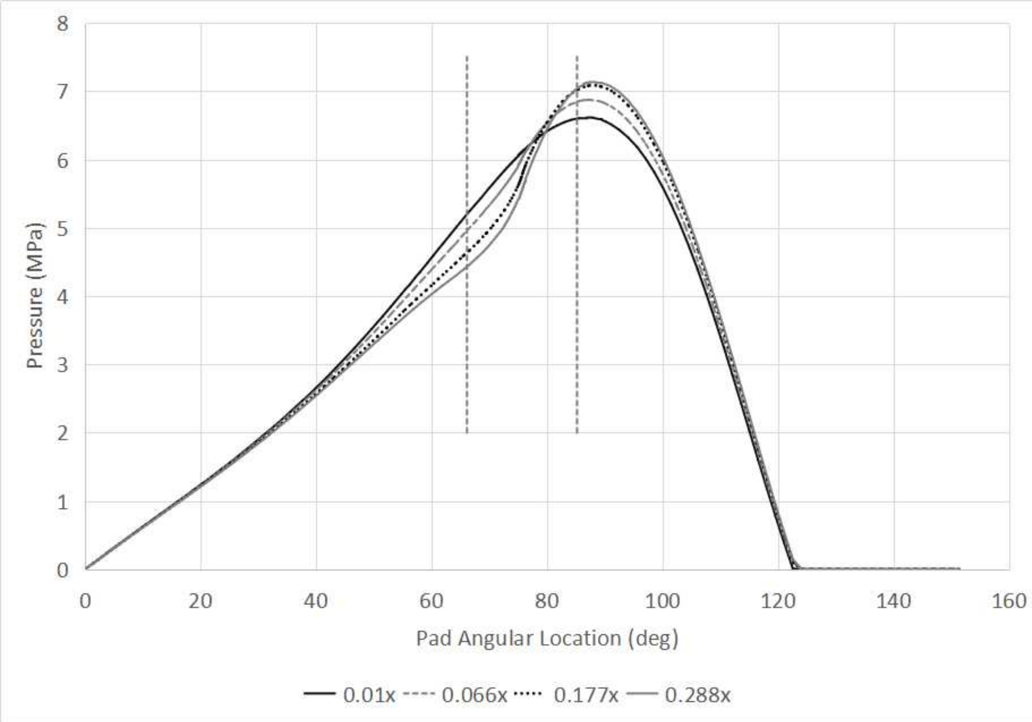

Figure 20: Centerline pressure for bearing with nondimensional jacking pocket depth varying from 0.01 to 0.29

occurred, resulting in a maximum increase in the peak pressure of 6% for the 0.29 case. This peak occurred slightly behind the groove, at the same location as seen in the smooth case ($\overline{d_g} = 0.01$). Figure 21 shows the pressure profile as $\overline{d_g}$ is increased up to 0.6. The initial pressure drop continued, but the peak pressure started to drop as well. The peak pressure location also shifted further downstream of the pocket.

Figure 22 shows the centerline pressure profile results as the pocket depth was increased to $6.3 \times C_b$. As the depth increased further, the pressure proceeding to the pocket experienced a small increase in pressure, while the pressure at the center of the pocket dropped. This resulted in two pressure peaks, one at the leading edge of the pocket and another one slightly downstream of the pocket. The downstream peak pressure continued to drop as the pocket deepened down to a 20% reduction from the smooth case. Figure 23 shows the pressure profiles of the flow running through the center of the pocket corresponding to Figure 22. The centerline pressure at circumferentially corresponding to the center of the groove experienced a discontinuous gradient. This was most likely due to the collision of two vertices. Pockets deeper than $6.7 \times C_b$ ceased to have any additional influence on the pressure

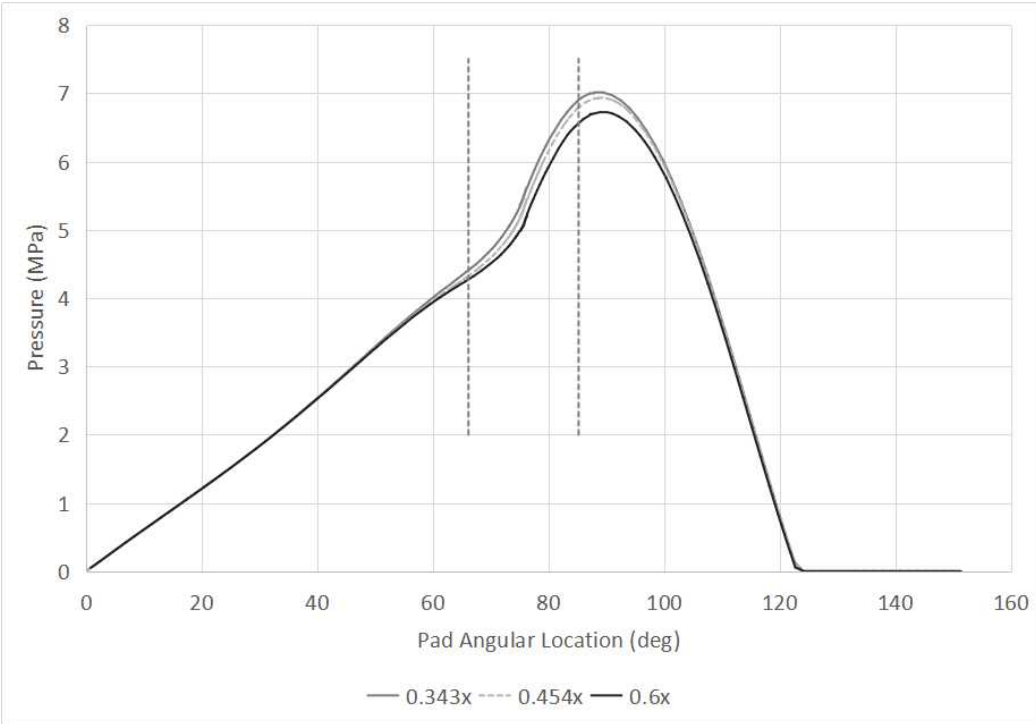

Figure 21: Centerline pressure for bearing with nondimensional jacking pocket depth varying from 0.34 to 0.60

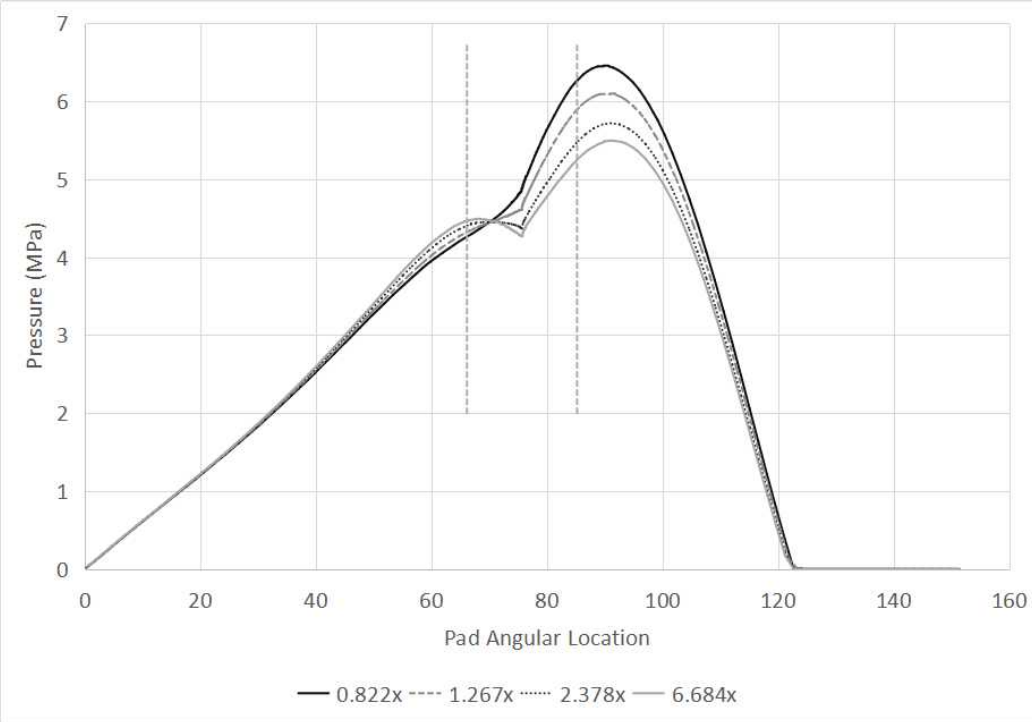

Figure 22: Centerline pressure for bearing with nondimensional jacking pocket depth varying from 0.82 to 6.7

profiles and the vertical hydrodynamic forces. Branagan [63] found a similar limit by applying short bearing theory to a bearing with a circumferential scratch. This limit also corresponds well with what was found in Chapter 2. Figures 24 and 25 show the pressure profile of the film for two of the groove depths. The peak pressure is reduced while a more uniform pressure from the groove region occurs farther downstream and upstream of it, as well as further axially.

The pressure profile predominately shifted between two regimes (Figure 20 and Figure 22). In Chapter 2, these two regimes were distinct with an exact, nondimensionalize depth of the stadium-shaped, jacking pocket of 0.28 at which the flow shifted between them. In this study, that transition was less distinct, and there were a small range of depths (0.34 $\times$ C_b- 0.6 $\times$ C_b where trends from both of the regions occurred. This transitional regime was captured in Figure 21.

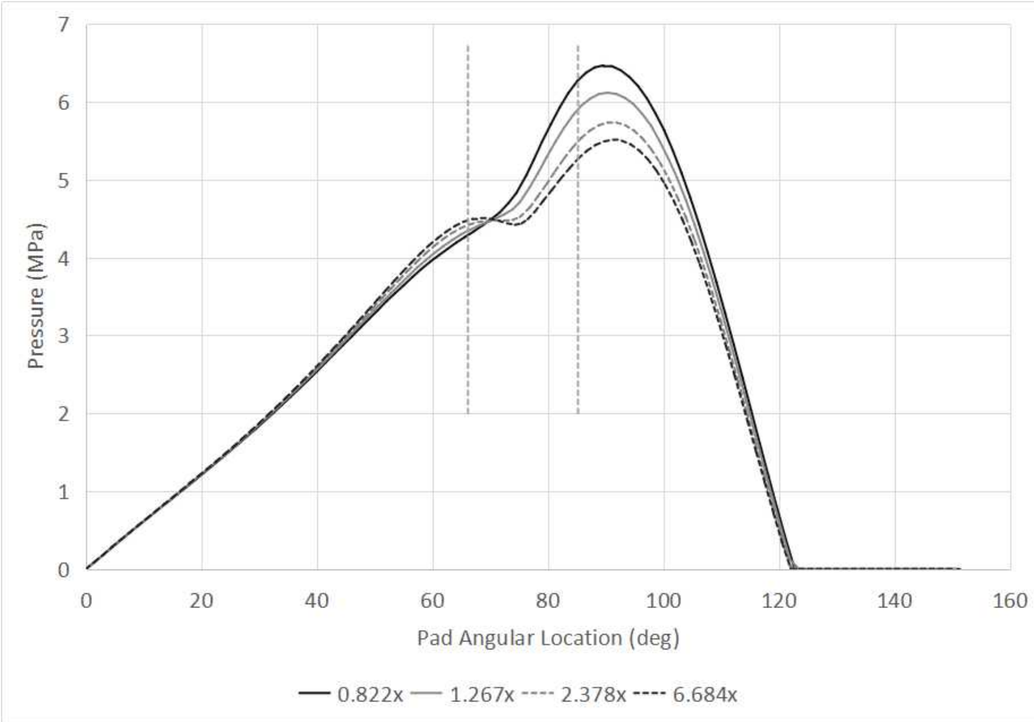

Figure 23: Pocket centerline pressure for bearing with nondimensional jacking pocket depth varying from 0.82 to 6.7

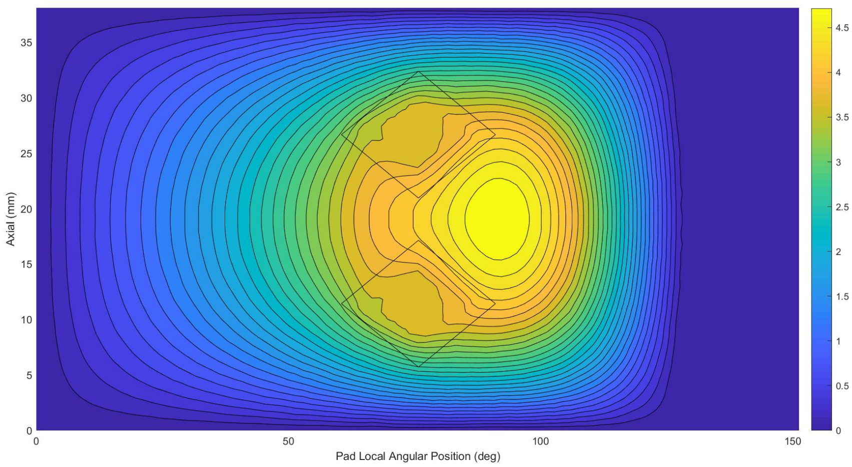

Figure 24: Film pressure for pair of diamond-shaped, jacking pockets with nondimensional depths of 0.5

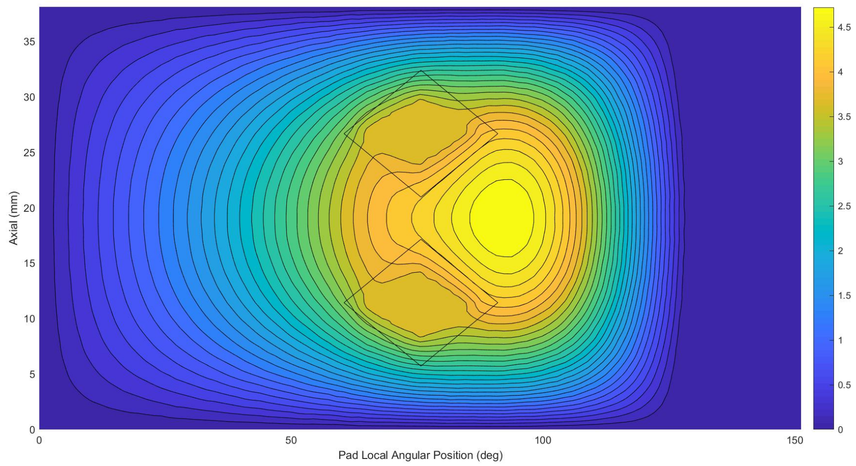

Figure 25: Film pressure for pair of diamond-shaped, jacking pockets with nondimensional depths of 2.38

3.3.3 Design-of-Experiments and Linear Regression Models

A design-of-experiments was utilized to better categorize the influence of the double-diamond jacking pockets on the bearing performance. The jacking pocket's geometric design variables were varied over the ranges shown in Table 13.

The seven responses that were examined were power loss, eccentricity ratio, attitude angle, and both the direct and cross-coupled stiffness terms. A central composite design (CC) [64] was performed at five different levels (different values for each design parameter). A CC design was chosen to allow the fitting of regression models, which included curvature and first order interaction effects between the design parameters. This design resulted in twenty five different geometric cases. Differing from the above pocket depth study, the equilibrium position for each bearing was found using the Nelder-Mead algorithm [65]. The resulting sum of forces were reduced to below 0.5% of the applied load for each case. Finding the equilibrium allows for an improved understanding of actual running conditions. The method of calculating the stiffnesses and the power loss are described in Chapter 2. Across the span of responses, three of the pocket designs were found to be outliers based on the distribution of externally studentized residuals across all of the responses. Each one of the outliers had a very large spread between the pockets ($\bar{m}$) and a short circumferential length ($\bar{l}_{dd,c}$). The wide pocket spread moves the pockets farther from the high pressure region of the

Table 13: Double Diamond Design Parameters

Parameters	Upper Bounds	Lower Bounds
$\bar{d}_g$	0.01	20
$\bar{l}_{dd,c}$	0.05	0.15
$\bar{l}_{dd,a}$	0.25	0.9
$\bar{l}_m$	0.25	0.9

pad at the axial center, while a short circumferential length can reduce the overall effectiveness as demonstrated in the previous study (Chapter 2) on stadium-shaped, jacking pockets. The combination of these things resulted in a reduction in the influence of the pocket geometry resulting from the reduced overall pocket influence on bearing operation.

A summary of the span of the bearing response is shown in Table 14. All of the cases showed a decrease in power loss when compared with the smooth bearing case. This agrees with what was seen in Chapter 2 as well as with Heinrichson's findings [14]. This is due to the pocket's presence decreasing the cross film velocity gradient which reduces the shearing on the surface of the journal. The drop in power loss was rather small owing to the relatively low surface area of the pockets when compared with the rest of the pad area. All of the stiffnesses showed an increased variation over the whole range of responses when compared to the stadium-shaped pocket design-of-experiment. This is likely due to the larger range of pocket depths used in this study. In Chapter 2, The pockets' depth was limited to the second pocket depth regime and deep pockets. Expanding this range to include the first regime should greatly increase the spread of the stiffness responses as the pressure lift due to shallow pockets would be captured.

A least-squares linear regression model was developed for each the seven different bearing responses [66]. An R^2 value is a measure of a model's ability to accurately predict the variability in the data. The addition of each new term will improve the R^2 value at least a little. An adjusted R^2 value accounts for this by adding a penalty for each new term to prevent statistically insignificant terms. A model that predicts 80% of the variation of the response will have an adjusted R^2 value of 0.80. This also means that 20% of the variation can not be explained by the model. Another analysis of variance (ANOVA) statistic is the p-value. This represents the likelihood that the relationships in the model can be attributed to chance. A confidence interval of 95% that the model can not be attributed to chance results in a

Table 14: Double diamond pocket DOE response summary

Response	Units	Min.	Max.	Std. Dev.
Kxx	N/mm	9.53e4	1.43e5	7467
Kxy	N/mm	1.21e4	3.84e4	4544
Kyx	N/mm	-2.97e5	-2.11e5	16509
Kyy	N/mm	9.29e4	1.31e5	5014
ξ	W	1.13e3	1.15e3	1.79
e/C_b	-	0.581	0.600	6.52e-4
ϕ	degrees	45.7	47.9	0.133

Table 15: Response Data for Smooth Bearing

Response	Units	Value
K_{xx}	N/mm	1.27e5
K_{xy}	N/mm	2.40e4
K_{yx}	N/mm	-2.78e5
K_{yy}	N/mm	1.06e5
ξ	W	1.16e3
e/C_b	-	0.55
ϕ	degrees	47

Table 16: R^2 Values for Best Fit Linear Regression Models

Response	R^2	Adjusted R^2	p-value
K_{xx}	0.66	0.60	3.15e-4
K_{xy}	0.36	0.20	1.09e-1
K_{yx}	0.59	0.52	1.34e-3
K_{yy}	0.74	0.57	6.80e-3
ξ	0.90	0.86	1.88e-6
e/C_b	0.998	0.996	4.23e-10
ϕ	0.96	0.94	2.03e-7

Table 17: Regression model coefficients for power loss and eccentricity

	ξ	e/C_b	ϕ
A_1	1.38e3	0.579	47.0
A_2	0.752	2.18e-3	0.365
A_3	-3.58	1.26-2	-0.235
A_4	-7.18	0.117-2	0.433
A_5	3.94	3.13e-3	0.547
A_6	8.00	-1.90-2	0.294
A_7	-	4.15e-2	-0.498
A_8	-	-5.29e-3	0.446
A_9	-	-	-1.94

p-value of 0.05. A p-value can be obtained for each individual coefficient, as well as for the model as a whole. The regression model for each response was developed using forwards regression by adding new terms based on their individual p-value. All of the models presented in this chapter had p-values below the standard limit for statistical significance of 0.05. The R^2 values, adjusted R^2 values, and p-values for each model are presented in Table 16. The coefficients for each of the different regression models are presented in Tables 17 and 18.

For the direct horizontal stiffness, the data showed an overall variation of 38% of the smooth case, although the standard deviation was only 6%. A model was developed with linear relationships to each of the the design

Table 18: Regression model coefficients for stiffness coefficients

	K_{xx}	K_{yx}	K_{yy}
A_1	1.19e5	-2.57e5	1.15e5
A_2	2.28e4	-3.15e4	-1.05e3
A_3	-7.15e3	1.73e4	-6.70e3
A_4	-1.15e4	2.60e4	-3.35e3
A_5	-	-	2.61e3
A_6	-	-	-1.87e4
A_7	-	-	-2.40e4
A_8	-	-	-1.08e4

variables with the exception of the pocket depth as shown in Equation 3.1.

$$K_{xx} = A_1 + A_2\bar{l}_{dd,a} + A_3\bar{l}_{dd,c} + A_4\bar{l}_m \tag{3.1}$$

Both the circumferential length of the pocket and the distance between the pockets decrease the horizontal stiffness while the axial length increases it. An increased circumferential pocket length will allow the high pressure to be distributed towards the leading and trailing of the pad. This higher pressure will increase the stiffness of the film. The influence is limited, as the pocket does not extend far from the vertical axis. The previous study in Chapter 2 found similar correlation for both of the corresponding design parameters to axial and circumferential lengths of the stadium-shaped pocket. The adjusted R^2 value of this model was 0.6 meaning that the model only explained 60% of the variation in the data. This model did have a p-value of $3.15e-4$ meaning that the relationships captured by the model are statistically significant. Figure 26 shows a plot of the externally studentized residuals compared with the assumed normal probability distribution. The plotted line is the idealized case. A good model would expect to see a random distribution on either side of this case. However, the data shows an arcing shape that differs from the normal distribution. These results, coupled with the low adjusted R^2 values, shows that the model is failing to capture some important relationships between the design parameters.

The direct vertical stiffness showed variation of 36% and a standard deviation of 5% with respect to the smooth case's K_{yy} response. Two outliers were found for this response. These outliers had wide pocket distribution and short circumferential lengths which greatly reduced the influence of these pockets on the pressure distribution, resulting in negligible influence on the vertical

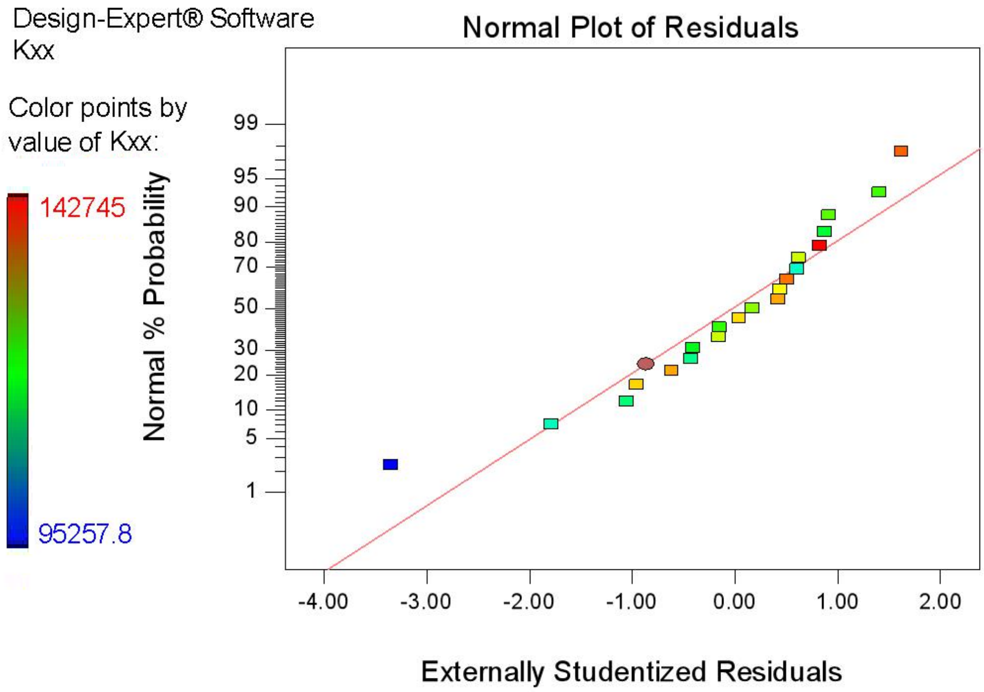

Figure 26: Plot of Kxx externally studentized residuals compared with the assumed normal probability distribution around the predicted

stiffness. Equation 3.2 presents a reduced, quadratic model for the vertical stiffness. All of the terms in the model reduced the vertical stiffness, with the exception of the first order pocket spread term. There were interaction terms between the pocket spread and both the depth and the axial length. The second of these terms is likely due to the nondimensionalization of the axial length. An increase in the spread of the pockets will cause an increase in the overall axial length of the pocket.

$$\begin{aligned} K_{yy} = A_1 + A_2\bar{d}_g + A_3\bar{l}_{dd,a} + A_4\bar{l}_{dd,c} + A_5\bar{l}_m \\ +A_6\bar{d}_g\bar{l}_m + A_7\bar{l}_{dd,a}\bar{l}_m + A_8\bar{l}_{dd,c}^2 \end{aligned} \tag{3.2}$$

Only 57% of the variability in the data was captured by the model based on the adjusted R^2 value. This means that the model did not capture all aspects of this response's behavior. The p-value was $1.34e-3$ which signifies that it was highly unlikely that the trends captured in this model were attributed to chance. Figure 27 shows the externally studentized residuals compared with the assumed normal probability distribution for K_{yy}. This data fell along a line which differs from the idealized case. A second line trend seems to occur at lower values but a limited number of data points makes this more uncertain. The current model for the direct vertical stiffness did not capture all of the trends in the data.

K_{xy} had the largest variation of all of the responses with an overall variation of 110% and a standard deviation of 19% of the smooth case. Unfortunately a reasonable model was unable to be developed for this response. The best calculated model had a p-value of 0.11 which means that there was an 11% likelihood that the model could be attributed to chance. This was below the standard 95% confidence interval. The K_{yx} response varied by 31% of the smooth case response and had a standard deviation of 6%. A first-order, regression model with all terms for each of the design parameters except pocket depth was fit to the data and is presented in Equation 3.3.

$$K_{yx} = A_1 + A_2\bar{l}_{dd,a} + A_3\bar{l}_{dd,c} + A_4\bar{l}_m \tag{3.3}$$

Unfortunately an adequate empirical regression model for describing the double diamond jacking pockets' influence on the bearing stiffness was not found based on these design variables. The adjusted R^2 values for each of the responses was at or below 0.60. These models were inadequate as at best they described up to 60% of the variation in the data. However, all of these models, with the exception of K_{xy} had p-values smaller than 0.05. This means that while each of the models failed to fully model the response, the models were statistically significant. One reason for the low adjusted R^2 values was the complexity of the flow around these pockets. This complexity occurred

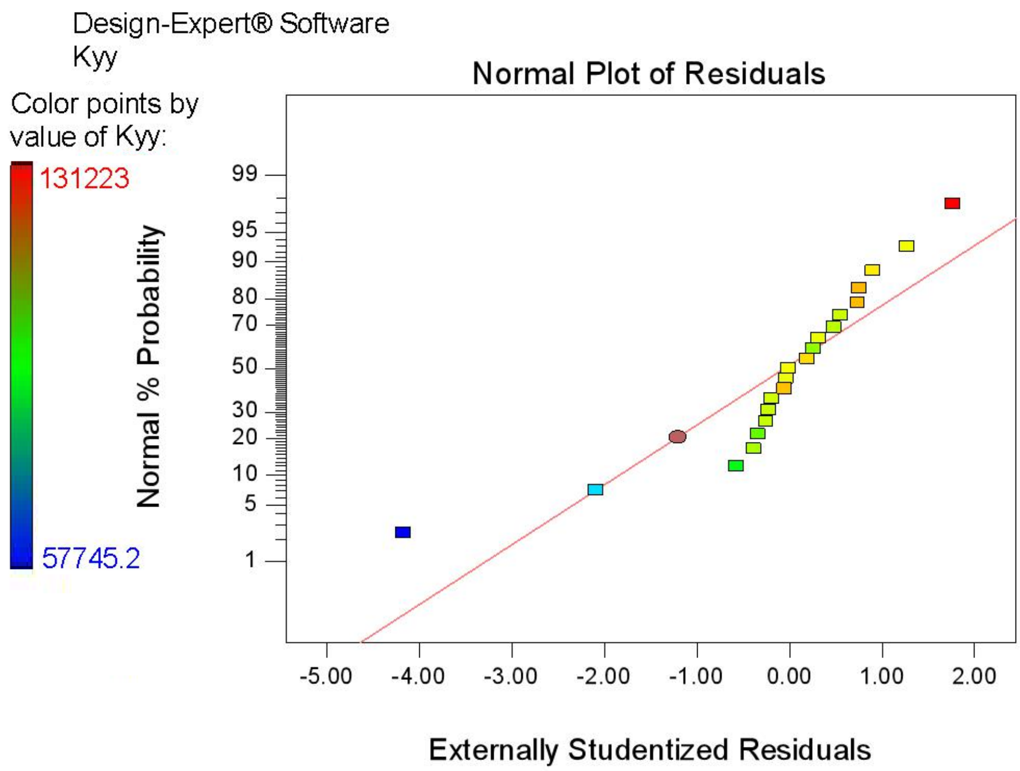

Figure 27: Plot of Kyy externally studentized residuals compared with the assumed normal probability distribution around the predicted

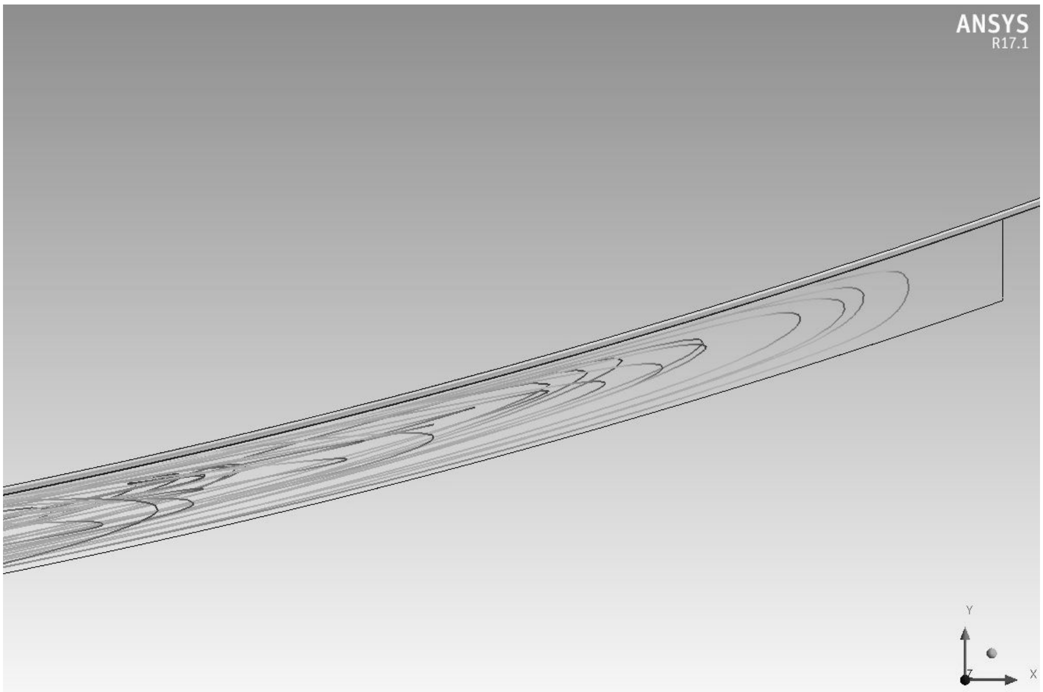

Figure 28: Radial vorticity at trailing edge of diamond pocket

as a result of the orientation of the diamonds in relationship to direction of the flow in the film. Figures 28-30 show this flow for three different pocket shapes. Significant vorticity in all three dimensions was occurring in the pocket, especially along the trailing edge of the pocket.

The power loss had an overall variation of 1.7% and a standard deviation of 0.15% of the smooth case power loss. Overall the pocket geometry had a minimal influence on the power loss of the bearing. This agrees with the results presented in Chapter 2. The variation seen in this study was less than was seen with the stadium-shaped, jacking pocket (Chapter 2). This is attributed to the reduced area of the double diamond pocket designs and the shift of the pockets away from the axial centerline. A reduced quadratic model was developed and is shown in Equation 3.4. The dimensionless pocket depth had the largest influence on the power loss, followed by the distance between the pockets. This model had an adjusted R^2 value of 0.86. The model described the variation of the data well, although more data points could be used to improve its predictive capabilities.

$$\xi = A_1 + A_2\bar{d}_g + A_3\bar{l}_{dd,c} + A_4\bar{l}_m + A_5\bar{d}_g\bar{l}_m + A_6\bar{d}_g^2 \tag{3.4}$$

The eccentricity ratio had a variation of 3.4% of the smooth case with a standard deviation of 0.1%, while the attitude angle varied up to 4.7% and

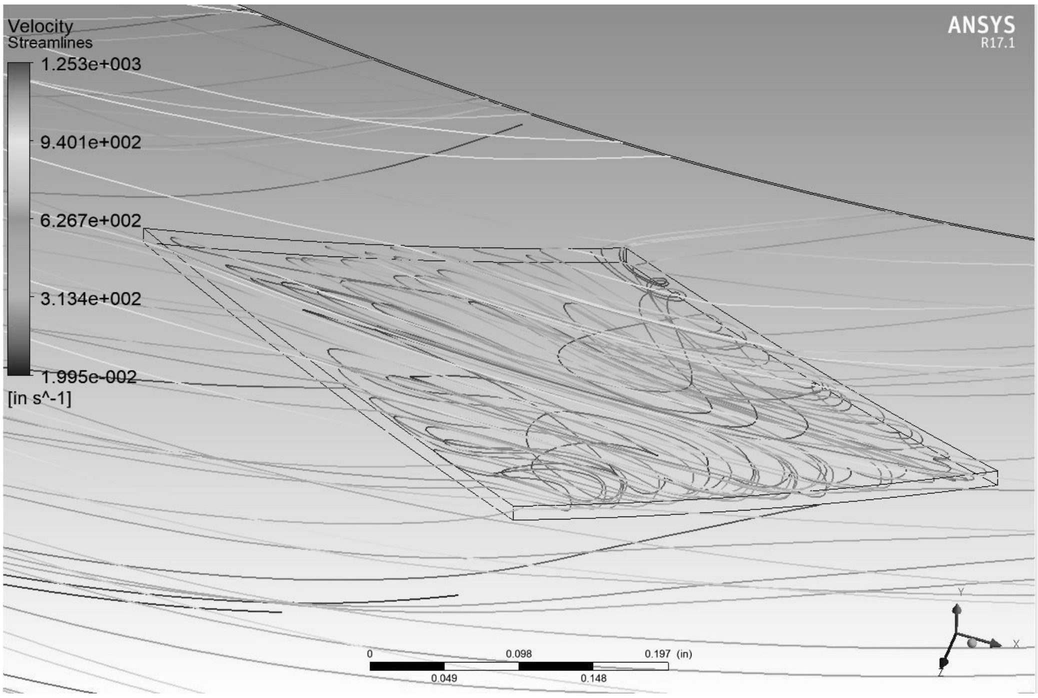

Figure 29: isometric view of streamlines in a diamond pocket

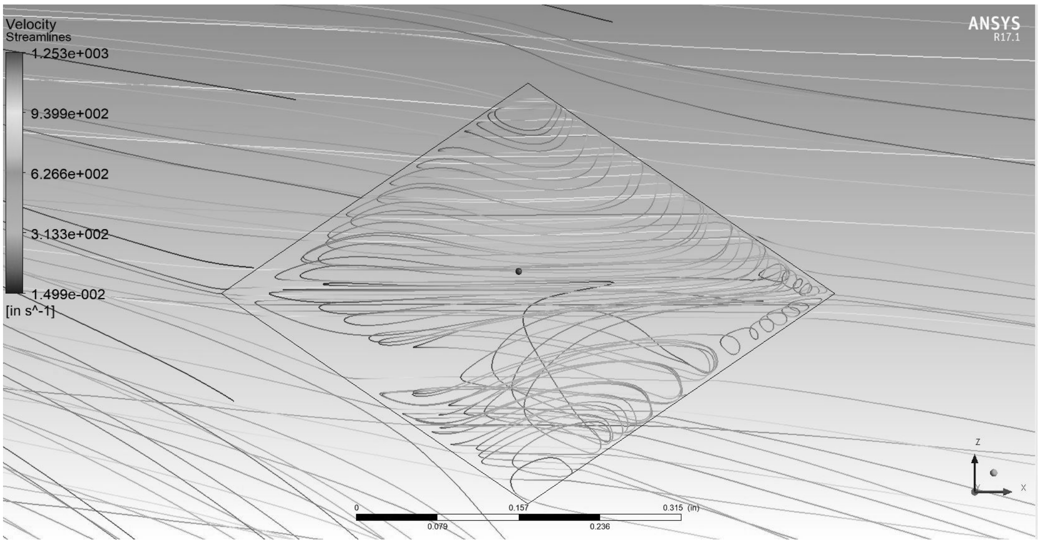

Figure 30: Streamlines running across and in a diamond pocket.

had a standard deviation of 0.3%. The attitude angle changed by slightly more than 2 degrees over the whole range. Two outliers were excluded from these results. One of the outliers had a very shallow pocket and was in the regime 1 where additional lift is generated. The other pocket had an extremely wide axial spread on the pockets. This meant it had a significantly reduced influence on the load carrying portion of the bearing at the axial center. When these cases were included the eccentricity ratio actually varied by 10% of the smooth case response. The model for the eccentricity ratio is given in Equation 3.5. The equation was a reduced quadratic model with two monovariate quadratic terms and 4 interaction terms. The adjusted R^2 value was 0.996. This model can explain over 99% of the variation of the data across the design range. The pocket depth had a large influence on the eccentricity ratio. The shallow pockets generated additional lift while the deeper pockets caused a loss in the pressure generation. The distance between the pockets also had a large influence on the eccentricty ratio. The larger distance between the pockets moved the pockets farther away from the pressure generating region of the pad minimizing the influence of the pockets.

$$\begin{aligned} e/C_b = A_1 + A_2\bar{d}_g + A_3\bar{l}_{dd,a} + A_4\bar{l}_{dd,c} \\ +A_5\bar{l}_m + A_6\bar{d}_g^2 + A_7 bar l_{dd,c}^2 + A_8\bar{l}_m^2 \end{aligned} \tag{3.5}$$

The regression model for the attitude angle is given in Equation 3.6 and had an adjusted R^2 of 0.94. This is a good model as it explains 94% of the variation of the data.

$$\begin{aligned} \phi = A_1 + A_2\bar{d}_g + A_3\bar{l}_{dd,a} + A_4\bar{l}_{dd,c} + A_5\bar{l}_m \\ +A_6\bar{d}_g\bar{l}_{dd,c} + A_7\bar{l}_{dd,a}\bar{l}_{dd,c} + A_8\bar{l}_{dd,a}\bar{l}_m + A_9\bar{l}_{dd,a}^2 \end{aligned} \tag{3.6}$$

3.4 Hourglass-Shaped Jacking Groove

3.4.1 CFD Model

The second jacking feature geometry examined in the chapter was an hourglass-shaped groove. Figure 31 shows the groove and some of the defining geometric parameters, along with the axis of symmetry. The entire feature was defined by the circumferential length ($l_{f,c}$), the axial length ($l_{f,a}$), the width of the groove (w_f), the groove depth ($d_f g$), and the depth of the contained land region (d_{fl}). This land region was composed of the two triangular regions contained by the groove. These are sometimes machined to a depth between the pad surface and the groove depth. The geometry features were non-dimensionalized in this study. These nondimensional parameters are defined in the Nomenclature.

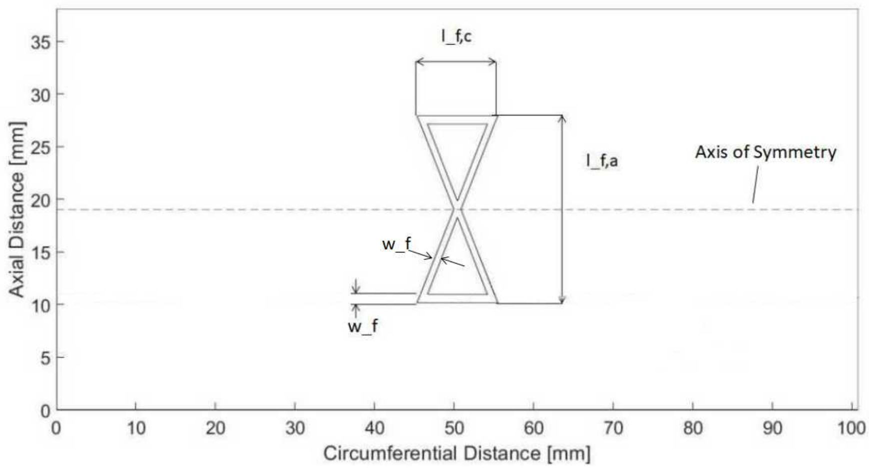

Figure 31: Pad and hourglass-shaped groove geometry

Table 19: Hourglass-Shaped Groove Mesh Independence Design Parameters

$\bar{d}_{f,g}$	10
$\bar{d}_{f,l}$	0.05
$\bar{l}_{f,a}$	0.575
$\bar{l}_{f,c}$	0.1
$\bar{w}_f$	10
x_j/C_b	0.4085
y_j/C_b	0.4508

Table 20: Hourglass Mesh Density Information

Number of Elements	Groove Line Peak Pressure	Percent Difference
-	MPa	%
2.99e5	6.11	1.2
1.70e6	6.14	0.72
2.14e6	6.15	0.55
9.74e6	6.18	0

A mesh independence study was performed to balance the accuracy of the results with simulation runtime. The hourglass-shaped, jacking groove geometry is given in Table 19, along with the eccentricity position of the rotor. The number of elements and the peak pressure circumferentially inline with the center of the bottom of the hourglass shape are shown in Table 20 for several meshes of varying densities. The 1.7 million element mesh was chosen to reduce the runtime while still achieving accurate results.

3.4.2 Groove Depth vs Pressure Profile Study

A study was performed on the influence of the groove's depth on the pressure profile. The geometry of the jacking groove is the same as presented in Table 19. This table also contains the journal eccentricity that is used in each of the following simulations in this study. The nondimensional groove depth ($\bar{d}_{f,g}$) was varied between 0.1 to 10. Figures 32-33 show the resulting centerline pressure profiles. The pressure profile shifted between two different regimes. Figure 32 shows the first regime where the pressure drops at the leading edge of the jacking groove followed by a rapid rise in pressure. Figure 33 shows the second regime which is characterized by a constant pressure across the groove and a pressure spike following the groove. The load capacity of the bearing decreases in this regime. These results match those seen in Section 3.3.2 for the pair of double diamond pockets and in Chapter 2 for the stadium-shaped pocket. Both the hourglass-shaped groove and the stadium-shaped pocket had very distinct regimes, while there was some overlap of these regimes in the case of the double diamond jacking pockets. Figures 34 and 35 show the pressure profile of the film for two of the groove depths. The peak pressure is reduced while a more uniform pressure from the groove region occurs farther downstream and upstream of it, as well as further axially.

3.4.3 Groove Width vs Pressure Profile Study

Another study was performed on the influence of the hourglass-shaped groove width on the pressure profile. The same operating variable, design parameters, and automatic mesh generation options were used in this study as presented in Section 3.4.1. The nondimensional groove width was varied from 1.67 to 16.3. The centerline pressure profile is plotted in Figure 36. As the groove was widened, the higher pressure at the center of the pad was bled off towards the axial edges of the pad along the trailing arms of the hourglass. This phenomena can be seen in the streamlines shown in Figure 37. Vortices in the groove carry the flow out towards the trailing corners.

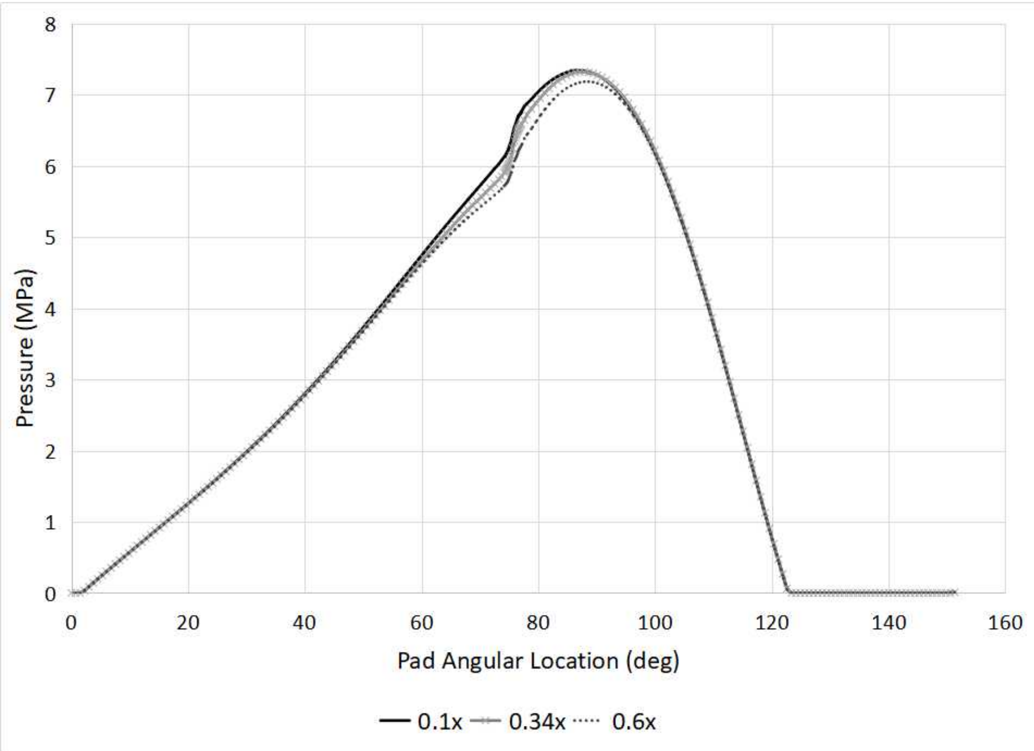

Figure 32: Centerline pressure profile with nondimensional jacking grove depth varying from 0.1 to 0.6

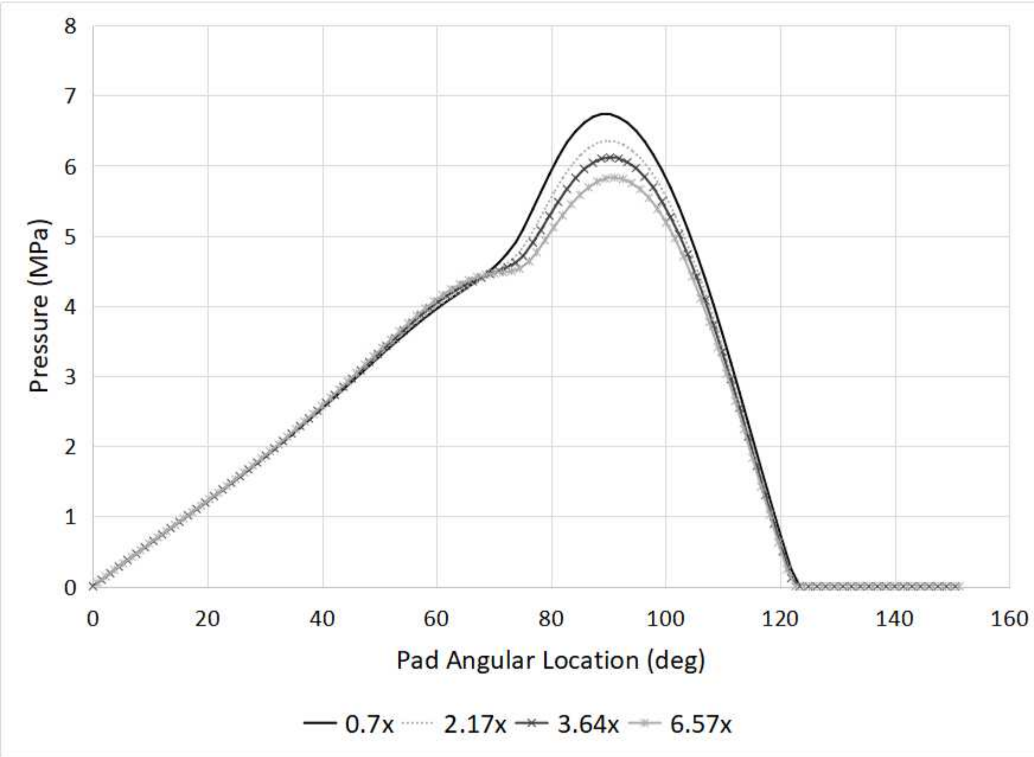

Figure 33: Centerline pressure profile with nondimensional jacking grove depth varying from 0.7 to 6.6

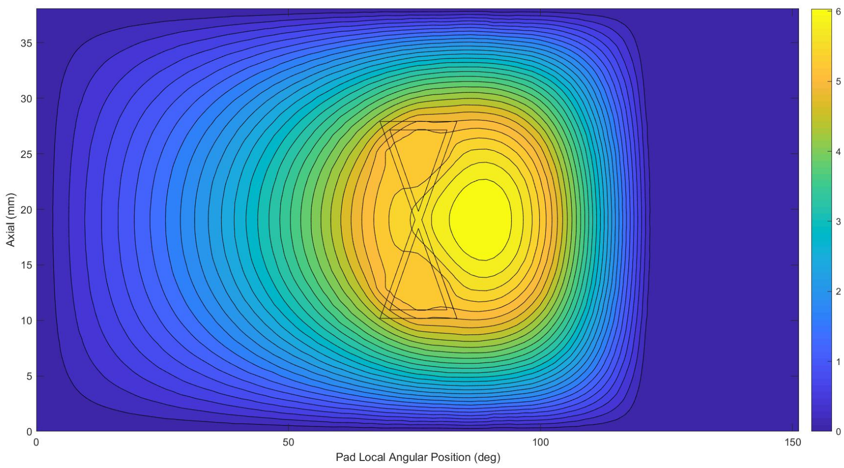

Figure 34: Film pressure for hourglass-shaped, jacking groove nondimensional depth of 0.34

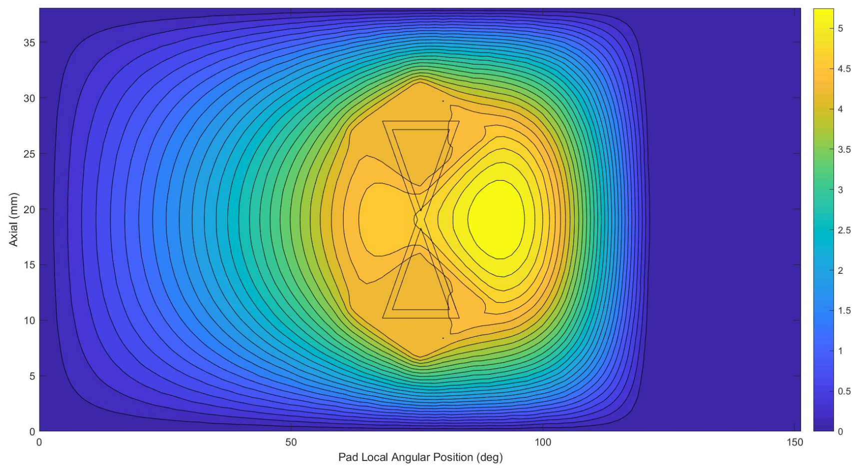

Figure 35: Film pressure for hourglass-shaped, jacking groove nondimensional depth of 3.64

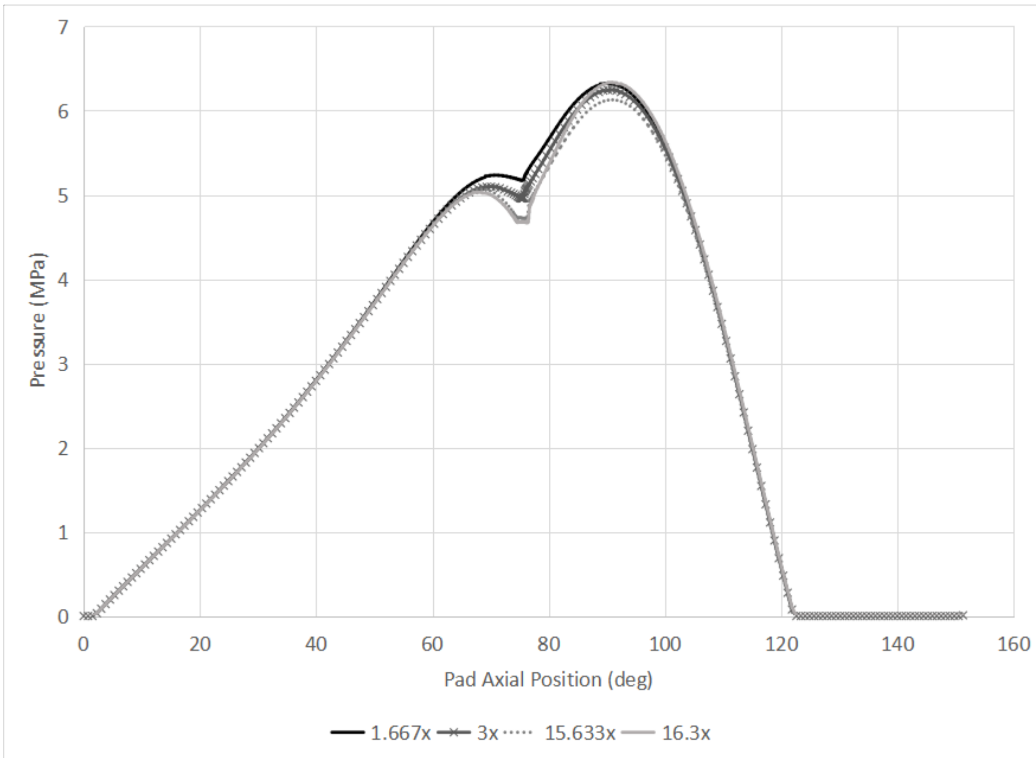

Figure 36: Centerline pressure for bearing with nondimensional jacking groove width varying from 1.67 to 16.3

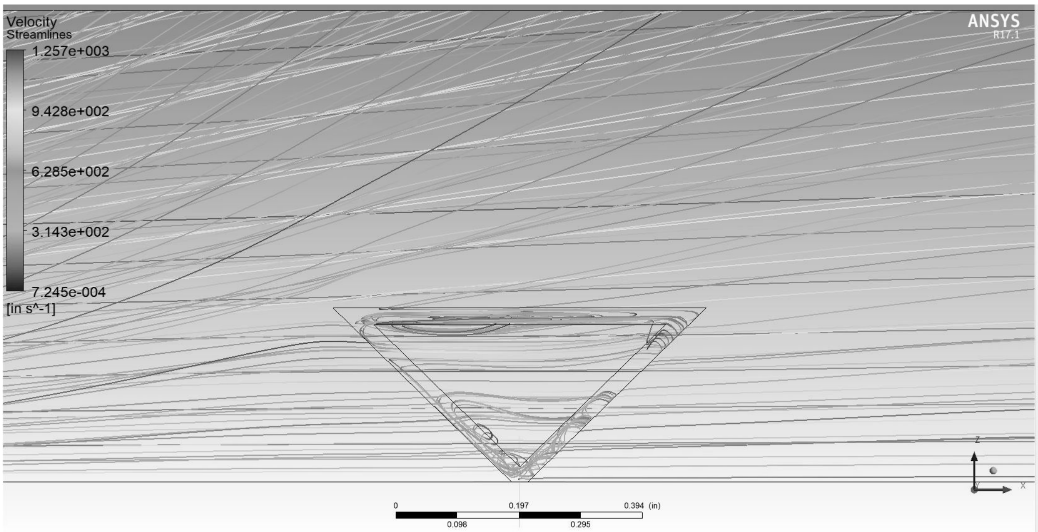

Figure 37: Bottom view of streamlines in a bearing including an hourglass-shaped jacking groove

Table 21: Hourglass Shape Design Parameters

Parameters	Equation	Upper Bounds	Lower Bounds
$\bar{d}_{f,g}$	$d_{f,g}/C_b$	0.1	20
$\bar{d}_{f,l}$	$d_{f,l}/C_b$	0.01	1
$\bar{l}_{f,c}$	$l_{f,c}/l_{p,c}$	0.05	0.15
$\bar{l}_{f,a}$	$l_{f,a}/l_{p,a}$	0.25	0.9
$\bar{w}_f$	w_f/C_b	5	20

3.4.4 Design-of-Experiments and Linear Regression Models

The next study was to use a design-of-experiment to test the bearing operation sensitivity to geometric changes of the hourglass-shaped groove. The bounds of the design parameter are presented in Table 21.

The same seven responses used for the pair of diamond jacking pockets Section 3.3.3 were examined here. A CC design [64] was performed which resulted in twenty seven different groove geometry cases. As in Section 3, the Nelder-Mead algorithm [65] was used to find a equilibrium position of the shaft. Four of the data points had issues converging to a stable equilibrium point. These four points were ignored in this study.

A summary of the responses is shown in Table 22. The power loss was lower across all the designs than seen in the smooth bearing case (Table 15).

Table 22: Hourglass-shaped, jacking groove DOE response summary

Response	Units	Min.	Max.	Std. Dev.
Kxx	N/mm	9.55e4	1.20e5	1385
Kxy	N/mm	2.26e4	2.67e4	393
Kyx	N/mm	-2.73e5	-2.10e5	2036
Kyy	N/mm	9.55e4	1.08e5	842
ξ	W	1136	1152	0.678
e/C_b	-	0.546	0.572	6.33e-4
ϕ	degrees	45.64	48.44	0.104

Table 23: R^2 Values for Best Fit Linear Regression Models

Response	R^2	Adjusted R^2
K_{xx}	0.96	0.95
K_{xy}	0.75	0.72
K_{yx}	0.98	0.98
K_{yy}	0.81	0.80
ξ	0.99	0.97
e/C_b	0.99	0.98
ϕ	0.96	0.95

This agrees with what was found by Heinrichson [14], and in Chapter 2 and in Section 3.3.3. Overall the range of responses were quite similar to that seen by the pair of diamond jacking pockets. However, the hourglass-shaped groove had much smaller standard deviation for the stiffnesses.

Linear, regression models were developed for each of the seven responses. The same methodology was used as performed in Section 3.3.3. Two points were determined to be outliers based on the distribution of externally studentized residuals across all of the responses. One of these outliers had a shallower depth than the rest of the cases. The other outlier had a shorter circumferential length. As the circumferential length of the hourglass becomes shorter, it will eventually approach an axial groove, which will have a minimal influence on the pressure profile as shown in Chapter 2. The R^2 values, adjusted R^2 values, and p-values are presented in Table 23. The coefficients for each of the different models are presented in Tables 24 and 25.

Table 24: Regression model coefficients for power loss and eccentricity

	ξ	e/C_b	ϕ
A_1	1.14e3	0.559	47.5
A_2	-0.630	2.18e-3	0.448
A_3	-2.12	9.20e-3	0.793
A_4	-1.00	3.22e-3	-0.133
A_5	-7.55	1.02e-3	0.346
A_6	-0.645	2.68e-3	-0.442
A_7	-2.50	3.40e-3	-0.343
A_8	-1.95	1.96e-3	-
A_9	-3.46	-	-
A_{10}	4.38	-	-
A_{11}	2.78	-	-

Table 25: Regression model coefficients for stiffness coefficients

	K_{xx}	K_{xy}	K_{yx}	K_{yy}
A_1	1.11e5	2.25e4	-3.11e5	9.88e4
A_2	2.24e3	2.44e4	6.16e5	-3.27e3
A_3	-1.25e4	1.26e3	7.97e3	-
A_4	-3.01e3	-	-	-

The direct horizontal stiffness had a variation of 19% of the smooth case across the whole range but a standard deviation of only 1.1%. After the reduction of the full quadratic regression model for K_{xx}, there were no interaction terms with statistical significance. This model is shown in Equation 3.7.

$$K_{xx} = A_1 + A_2\bar{d}_{f,g} + A_3\bar{l}_{f,c} + A_4\bar{l}_{f,c}^2 \tag{3.7}$$

This model excellently accounted for the variability of the data as seen by its adjusted R^2 of 0.95. This model was dependent only on the depth of the groove and the circumferential length of the hourglass shape. The circumferential length had a stronger influence on the direct horizontal stiffness than the groove depth, for both linear and a quadratic terms. Both of the length terms decreased the stiffness term, while the groove depth increased the stiffness.

The direct vertical stiffness varied by 12% with a standard deviation of only 1% of the smooth case. The regression model was a simple first-order model dependent only on the circumferential length of the hourglass shape (Equation 3.8).

$$K_{yy} = A_1 + A_2\bar{l}_{f,c} \tag{3.8}$$

This model was able to capture some of the major trends in the data but only captured 80% of the variability, as seen by its adjusted R^2 value. The expansion of the lower pressure region, as seen in Figure 38 caused a reduction in the horizontal stiffness of the bearing. The pressure build up across region in between the two circumferentially oriented grooves was more limited. Expanding the axial distance between these two sections of the groove, increased the area axially of this lower pressure but did not have as significant effect on the upstream or downstream pressures. Expanding these sections circumferentially, caused a circumferential expansion of this lower pressure region. This moved the higher pressures on either side circumferentially of this region farther away from the direction of loading. This translation of peak pressure can be seen in Figure 38. This translation also caused a reduction in the peak pressure and some of the pressure in the groove region. The drop in the peak pressures resulted in a reduction in the stiffness of the film.

The lower model quality of the vertical stiffness matched the K_{yy} model quality presented in Chapter 2, which was explained by the complexity of the flow in and around the groove. Figures 39, 37, and 40 show the steamlines around the hourglass-shaped groove of various geometry. The diverse flow patters occurred directly in line with the negative y-axis, causing a directly impact on the horizontal stiffness of the bearing. This makes the modeling of

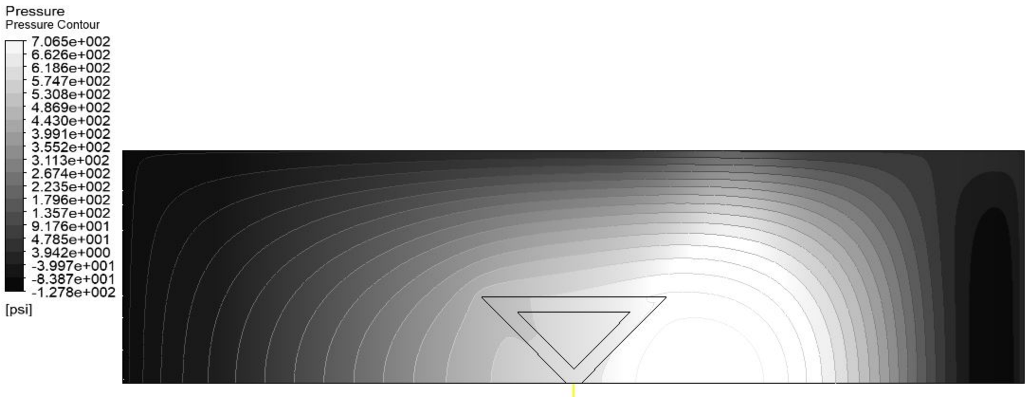

(a) Short circumferential groove

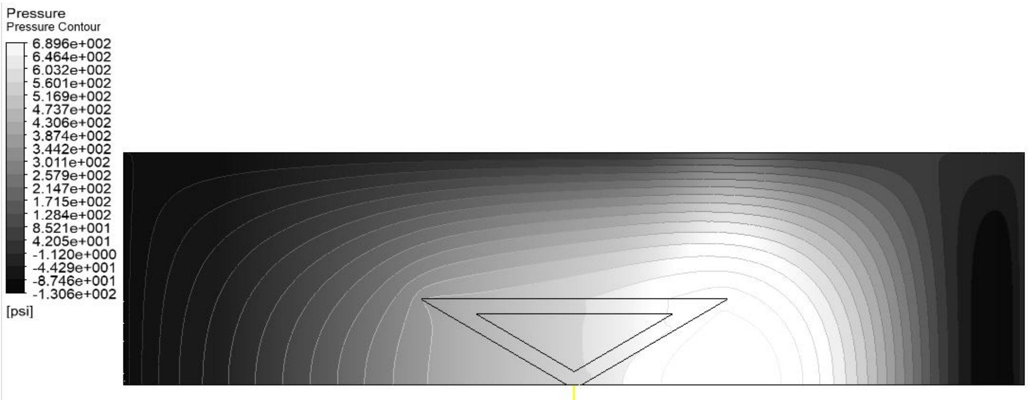

(b) Long circumferential groove

Figure 38: Pressure profiles with varying circumferential length of the hourglass-shaped groove

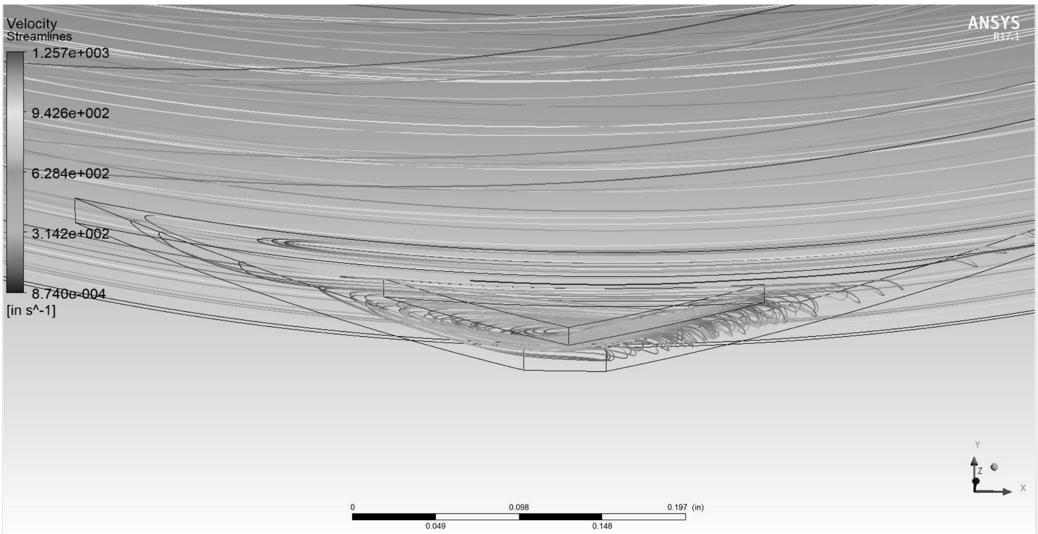

Figure 39: Streamlines in and around a hourglass-shaped groove showing radial vorticity

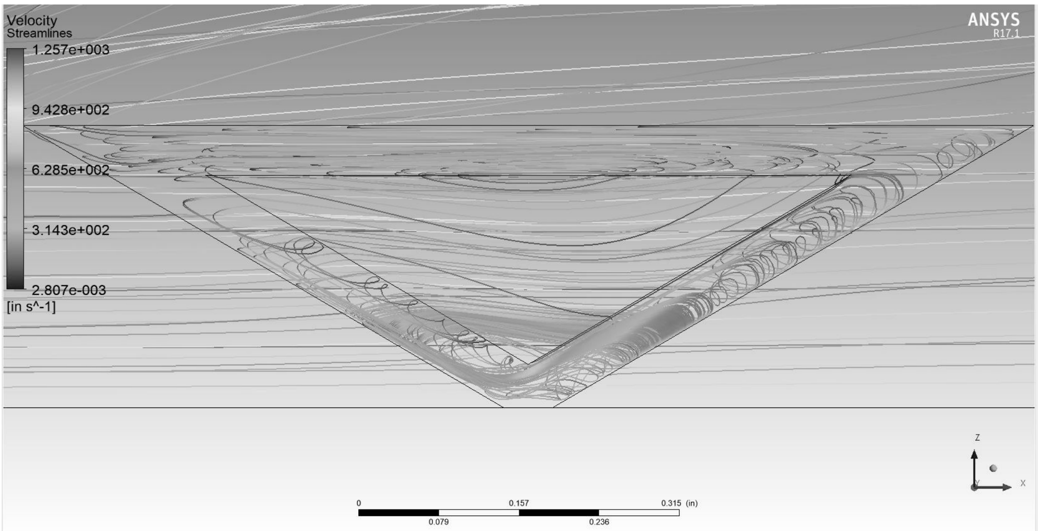

Figure 40: Bottom view of streamlines through a hourglass-shaped jacking groove

this parameter more challenging. Further data points are required to improve the predictive capability of this model.

K_{xy} had a variation of 17% of the smooth case response across the whole range and a standard deviation of only 2%, whereas K_{yx} varied by 23% across the whole range with a standard deviation of 1%. The resulting form of the best fit, regression model was the same for both of the cross coupled stiffnesses and is given in Equation 3.9. The coefficients for the models were different though, as shown in Table 25. The K_{yx} model predicted the variability of the data with an adjusted R^2 of 0.98. However, the K_{xy} model exhibited an adjusted R^2 value of 0.7. These models were only dependent upon the circumferential length of the hour-glass and the width of the groove. An increase to both of these factors increased both of the cross coupled terms.

$$K_{xy}||K_{yx} = A_1 + A_2\bar{l}_{f,c} + A_3\bar{w}_f \tag{3.9}$$

The power loss had very limited response to the variation in the geometry of the hourglass-shaped, jacking groove. A variation of 1.4% of the smooth case power loss was seen across the whole range with a standard deviation of 5.9e-2%.

$$\begin{aligned} \xi = A_1 + A_2\bar{d}_{f,g} + A_3\bar{d}_{f,l} + A_4\bar{l}_{f,c} + A_5\bar{l}_{f,a} + \\ A_6\bar{w}_f + A_7\bar{d}_{f,g}\bar{l}_{f,a} + A_8\bar{d}_{f,l}\bar{l}_{f,c} + A_9\bar{l}_{f,c}\bar{l}_{f,a} + \\ A_{10}\bar{d}_{f,l}^2 + A_{11}\bar{l}_{f,c}^2 \end{aligned} \tag{3.10}$$

The eccentricity ratio had a variation of 4.7% while the attitude angle had a variation of 5.9% of their corresponding responses for the smooth case. These two responses had standard deviations below 0.2%. Reduced quadratic models were used to describe these responses, which are presented in Equations 3.11 and 3.12. Both of these models predict most of the variability in the data, as seen by their high adjusted R^2 values of 0.98 and 0.95, respectively.

$$\begin{aligned} e/C_b = A_1 + A_2\bar{d}_{f,g} + A_3\bar{l}_{f,c} + A_4\bar{l}_{f,a} + \\ A_5\bar{w}_f + A_6\bar{d}_{f,g}\bar{w}_f + A_7\bar{l}_{f,a}^2 + A_8\bar{w}_f^2 \end{aligned} \tag{3.11}$$

$$\begin{aligned} \phi = A_1 + A_2\bar{d}_{f,g} + A_3\bar{l}_{f,c} + A_4\bar{l}_{f,a} + \\ A_5\bar{d}_{f,g}\bar{l}_{f,c} + A_6\bar{d}_{f,g}^2 + A_7\bar{l}_{f,a}^2 \end{aligned} \tag{3.12}$$

3.5 Conclusions

In this study, the influence of the geometries of both a pair of diamond pockets and an hourglass-shaped groove on bearing performance was examined. CFD was utilized to develop an understanding of the bearing operation. A study was performed by varying the depth of both of the jacking features and comparing the different pressure profiles. A similar study was performed by varying the width of the groove for the hourglass shape.

Design-of-experiment was performed for the two jacking features, and linear regression models were developed for each of the different bearing responses.

The pressure profiles of the pair of diamond pockets, the hourglass-shaped groove, and the stadium-shaped pocket, all shifted between two regimes as the depth of the feature increased. The flow trends were similar for each geometry. The first regime saw a drop in pressure occurring immediately prior to the leading edge of the feature. This was followed by a rapid increase in the pressure across the pocket or groove. The second regime was characterized by a constant pressure across the feature and the peak pressure occurring just downstream. For both the hourglass shape and stadium shape, the two regimes had a distinct boundary with a certain depth at which the profile changed regimes. This depth was $0.6 \times C_b$ for the hourglass shape, and $0.28 \times C_b$ for the stadium shape. The double diamond had a range of depths between the two regimes where behavior from both of the regimes was seen. The pressure at the leading edge of the pocket continued to drop as the peak pressure started decreasing as well. This range occurred at pocket depths varying from $0.34 \times C_b$ - $0.60 \times C_b$. For all three jacking feature geometries, as pocket depths approached $6.7 \times C_b$ the changes in the pressure profile decreased. Pocket depths beyond this value ceased to have any further influence on the pressure profile. This limit agrees with the study on circumferential scratches by Dr. Branagan [63].

The presence of jacking features had minimal influence on the power loss in the bearing and journal equilibrium position. This held true for all three designs. However, it can change the stiffness characteristics by a significant amount. The geometry of the pair of double diamonds pockets had variation in K_{xx}, K_{yy}, K_{xy}, and K_{yx} of 38%, 36%, 104%, and 31%, respectively. Failing to understand the influence of this design can introduce a high degree of cross coupling in the system. This can contribute significantly to rotordynamic instability. The geometry of the stadium-shaped pocket from Chapter 2 had variation in K_{xx}, K_{yy}, K_{xy}, and K_{yx} of 27%, 6%, 8%, and 12%, respectively. The pocket depth in Chapter 2 was more limited than the studies performed in this chapter. It is hypothesized that this is the reason that the variation is so much higher for the pair of diamond pockets than for the stadium-shaped pocket. The hourglass-shaped groove had variation in K_{xx}, K_{yy}, K_{xy}, and K_{yx} of 23%, 12%, 26%, and 20%, respectively. This jacking feature has much less of an effect on the film stiffness than the pair of diamond pockets (and potentially the stadium-shaped pocket). The variation in stiffness caused by the groove can still be important to understand to ensure overall machine stability.The variation in the direct stiffness terms can influence the location of the system critical speeds, which can result in higher than acceptable vibration in the machines.

This study builds upon the prior novel study presented in Chapter 2 by analyzing two additional jacking feature designs. The two regimes happen regardless of geometry type, and the transition between the two regimes occurs in the same range of depths. Deep pockets in which the pressure profile ceases to change occurred at approximately $6xC_b$ for all three cases. Lastly, it was demonstrated that the presence of jacking features in journal fluid-film bearings can have an appreciable influence on the stiffness of the film and should be accounted for to ensure safe machine operation. This chapter broadens the applicability of Chapter 2 as these trends hold true for varying size, shape, and number of pockets and for complicated grooves.

4 Thermoelastohydrodynamic Analysis of Journal Bearings with Rectangular Jacking Pockets

4.1 Introduction

Fluid-film bearings are vital components for the safe and successful operation of many industrial rotordynamic machines. In many larger operations, the price of the rotors are orders of magnitude more expensive than the bearings themselves. In these cases, the bearing surfaces are made with a softer sacrificial material to protect the journal during contact and to fully envelop hard particulates that could damage the rotor surface.

During startup (and shutdown) of these machines, the friction that occurs at the bearing surface transitions through several different regimes. Very high friction occurs in the initial stages when metal-to-metal contact is occurring. As the rotor speed increases, the friction reduces as the contact shifts to a mixed lubrication regime. The oil fills up the gaps between the rotor and bearing, though contact still occurs between the asperities of both surfaces. When the rotor spins at a high enough rate to generate a fully formed hydrodynamic film, low friction occurs.

For heavily loaded bearings, the high frictions that occurs in the early stages of startup and late stages of shut down are high enough to cause complete bearing failure due to excessive wiping of the soft surface material. Often high pressure oil is supplied to the bearing surface to hydrostatically support the bearings during these operations. This oil is fed to the pad using oil ports. These oil ports are connected to machined pockets or grooves that are designed to distribute the oil beneath the journal to enable hydrostatic lift. These machined features are vital for low speed operations. After the film is hydrodynamically capable of supporting the loads on the bearing, the high pressure oil is often shutoff to reduce power losses in the system.

Several studies were performed on these features under both hydrostatic and mixed conditions. There were a variety of different assumptions used (ignored [9], smooth pad [8], Reynolds equation [10]) in the literature to account for these features under hydrodynamic operation and rarely were adequate justifications presented in their defense. Several different studies were performed on the hydrodynamic performance of these features on thrust bearings [14, 15, 16, 18, 19, 20].

The number of studies that analyzed these feature's influence on fluid-film, journal bearings is greatly limited. Two computational fluid dynamics (CFD) studies on the influence of the geometry of several different jacking feature designs on dynamic performance of the bearings are presented in this dissertation (Chapter 2 and Chapter 3). The first study was focused on a stadium-shaped/rectangular jacking pocket design. The pocket depth was varied between $0.01 \times C_b - 50 \times C_b$. The resulting hydrodynamic force was found to increase by 11% of the smooth case for a pocket depth of $0.28 \times C_b$. The force decreased as the depth of the pocket increases beyond this. The hydrodynamic force reached 6% less than the smooth case for bearings with pocket depths of $6.7 \times C_b$ or greater. A design-of-experiment was performed on the bearing and used to develop regression models for several different bearing performance characteristics. The second study examined a pair of diamond shaped jacking pockets and an hourglass-shaped groove. The groove was found to have a less of an effect on the bearing performance when compared with the pockets. For all the designs, as the feature depths increased beyond $6.6 \times C_b - 7 \times C_b$, the influence on the film pressure became negligible.

This study presents an examination of the use of Reynolds equation in analyzing fluid-film bearings which include jacking pockets. The stadium-shaped, jacking pockets from the previous CFD study (Chapter 2) were used. A new tool was developed to solve the Reynolds equation while allowing for axial variation in the film thickness. Several different methods are presented with the goal of reducing the simulation runtime while still achieving accurate results. These methods were applied to a range of pocket depths and compared with the previous CFD results. A discussion is included on the applicability and the advantages of the different methods. Lastly, the best method was compared with several of the pocket designs that were developed in the design-of-experiment performed on the stadium-shaped pocket previously. The Reynolds equation results were compared directly with the CFD results with identical film geometries. An optimization was then performed on the Reynolds solution to find an equilibrium journal position. These new results along with the new journal equilibrium position are compared with the CFD results.

The objectives for this chapter were to:

1. Develop a suitable method for applying the Reynolds equation to fluid-film, journal bearings containing jacking features with
    - Accurate results
    - Reasonable runtimes
2. Validate the method using CFD results from Chapter 2
3. Compare optimized CFD results with optimized Reynolds equation results

Table 26: Fitzgerald and Neal [58] bearing geometry

Journal Diameter	mm	76.2
Axial Length	mm	38.1
Pad Thickness	mm	9.5
Radial Cb	mm	0.076
Pad Arc Length	deg	151.3
Preload		0.0
Offset		0.5
Shell Heat Conductivity	W/m-°C	50
Lubricant Density	kg/m	855
Lubricant Specific Heat	J/kg-°C	1952
Lubricant Heat Conductivity	W /m-°C	0.15
Lubricant Viscosity at 40 °C	Pa-s	0.028
Lubricant Viscosity at 99 °C	Pa-s	0.0047
Lubricant Supply Temperature	°C	50
Shaft Speed	rpm	8000
Load	kN	5.43

4.2 Bearing Model

The bearing from the experimental study of Fitzgerald and Neal [58] was chosen as the baseline for this study. The bearing is a two-pad, cylindrical bore bearing with geometry characteristics and operating conditions presented in Table 26 and a bearing cross section illustrated in Figure 41.

A model of this bearing was developed using MAXBRG, a thermoelastohydrodynamic (TEHD) code developed at ROMAC laboratory [59]. This code solves the modified 2D Reynolds equation, energy equation, and elasticity equations. The maximum Reynolds number in the film was $\tilde{3}00$ so the flow was assumed to be laminar. The temperature results from MAXBRG were compared with Fitzgerald and Neal's [58] experimental results in Figure 42. The results for the loaded pad are in good agreements, although MAXBRG does slightly overpredict the peak temperature.

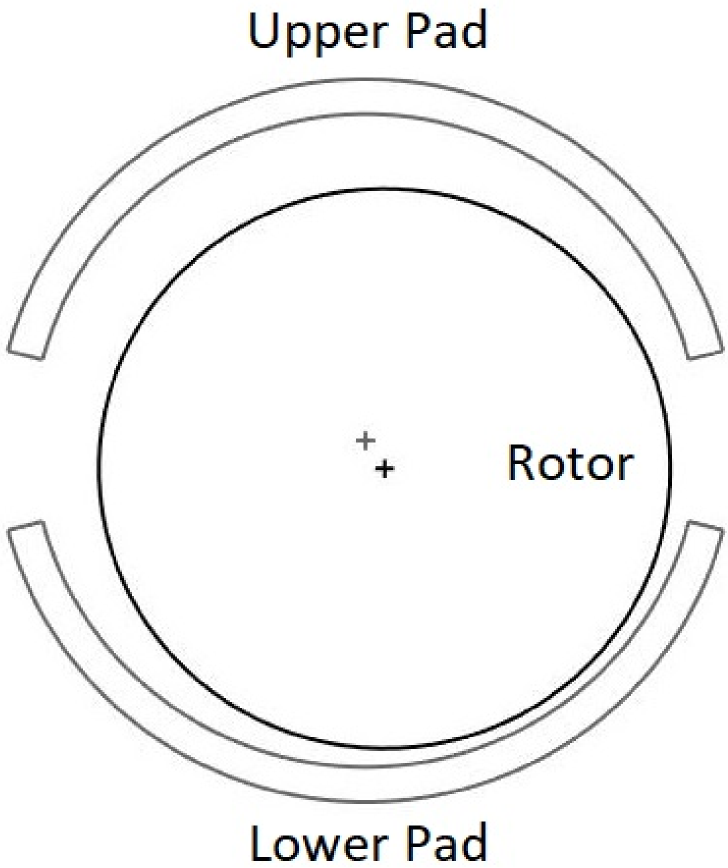

Figure 41: Lateral cross section of two-pad, cylindrical bore bearing from Fitzgerald and Neal [58]

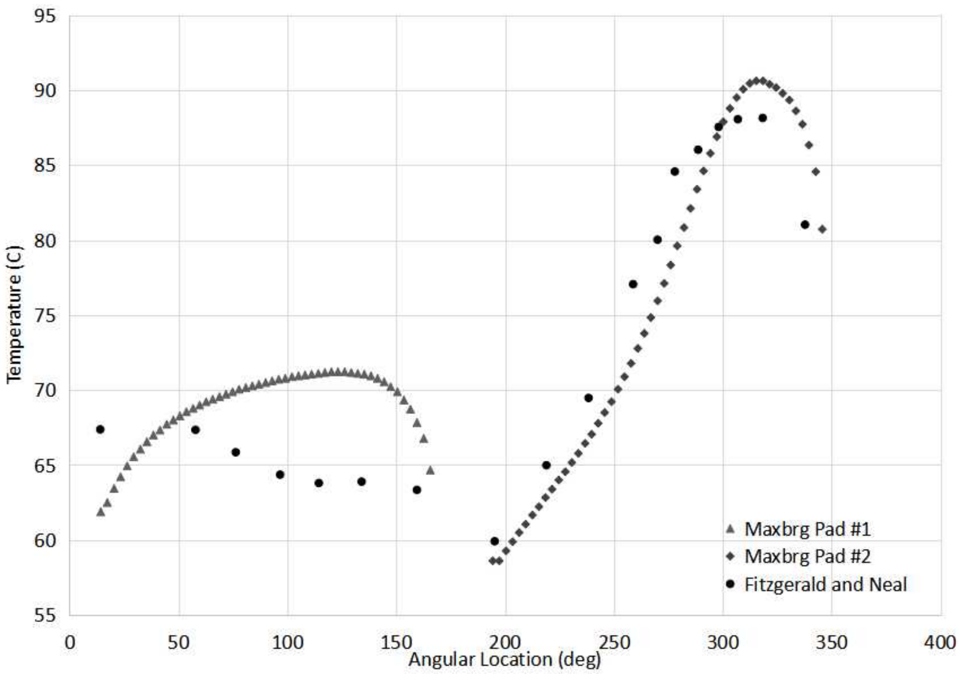

Figure 42: Comparison between experimental results[58] and 2-D TEHD solver

4.3 CFD Model

4.3.1 Smooth Bearing

An isothermal model was developed of the loaded pad of the Fitzgerald and Neal [58] bearing using ANSYS CFX. The top pad was neglected as the bottom pad was solely responsible for supporting the bearing loads. As the bearing and journal geometry created an axially symmetric fluid film, a symmetry boundary condition was applied along the axial centerline of the bearing. This line of symmetry can be seen in Figure 44. This assumption helped to reduced the size of the CFD model and shorten the simulation time. The flow was assumed to be laminar based on the low Reynolds number.

When the flow in a fluid-film, journal bearing gets past the minimum film thickness location and enters the diverging region, the amount of oil in the film is insufficient to fill the available volume. This additional volume is predominantly filled by the release of entrapped gases in the oil. It has been shown that the oil streamlets form as the film breaks up. In bearings, this process is called cavitation [68]. Current CFD software allows for full analysis of the two-phase flow in the diverging region. However, this significantly increases the runtime of the simulations. Another method is to assume that the negative pressures results are zero. While this method does not preserve mass conservation in the cavitated region and can introduce some errors in the pressure proceeding this region, it has been commonly used in literature [62] as it allows for much quicker simulations. The errors introduced by this simplified method are small, so it was used to decrease the simulation runtime.

The experimentally validated MAXBRG model was rerun with the isothermal assumption and using the same cavitation method to validate the CFD model. The results of both of these cases are presented in Figure 43. The peak pressure of the CFD results was approximately 20% higher than the peak pressure calculated by MAXBRG. The Reynolds equation assumes that the inertial effects in the film are negligible. The fluid density in the CFD model was set to 1% of the actual fluid density to approximate this assumption. These results are also shown in Figure 43. The CFD results with negligible inertia showed excellent comparison with the MAXBRG results, though there is a slight shift in the angular location of the peak pressure. As the model was validated with MAXBRG, the inertia was added back into the CFD model.

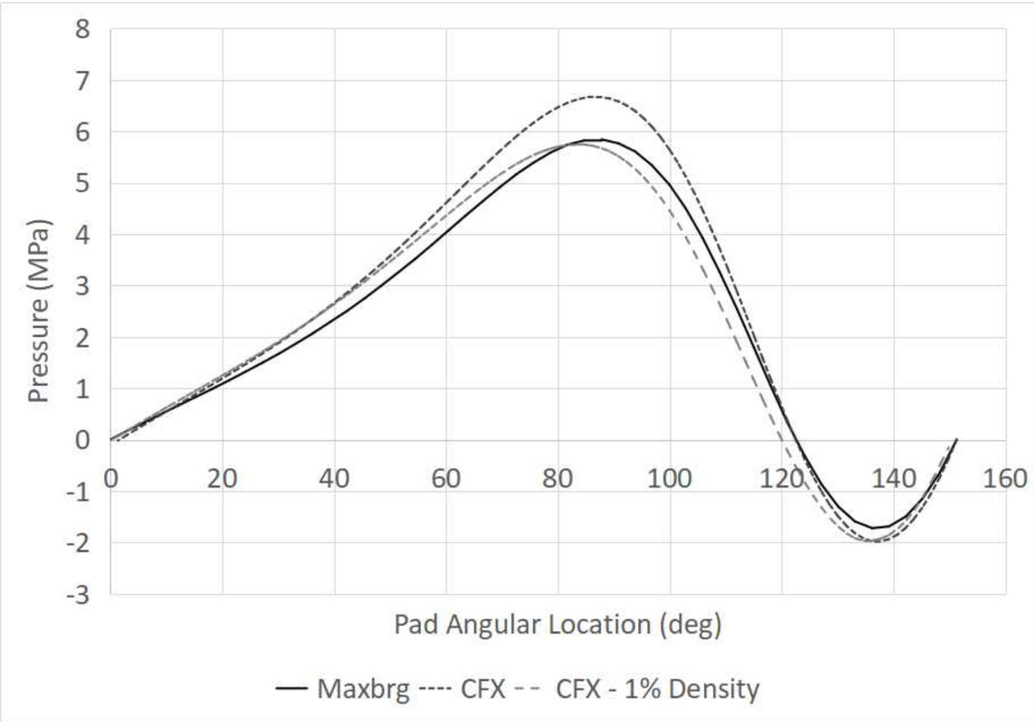

Figure 43: Comparison between 2-D TEHD solver and CFD model

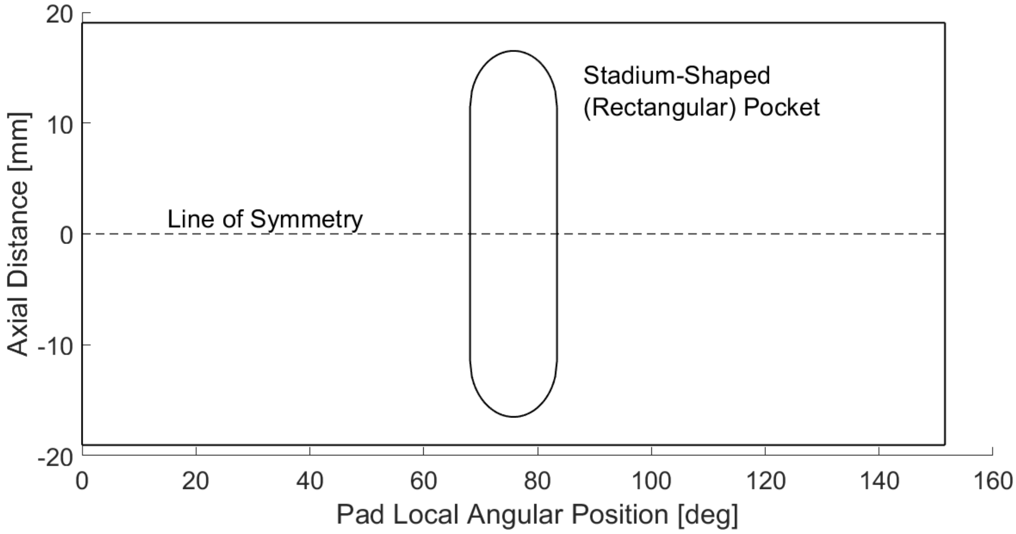

Figure 44: Two-dimensional view of bottom pad surface including a stadium-shaped/rectangular jacking pocket

4.3.2 Bearing with Stadium-Shape Jacking Pocket

After the base CFD model was validated, a stadium-shaped jacking pocket was added to it. This pocket was located axially centered on the pad and inline with the gravity loading. Figure 44 shows a two-dimensional representation of the pad surface including a stadium-shaped jacking pocket, along with the line of symmetry. The pocket geometry was defined by the axial length of the pocket (l_a), circumferential length of the pocket (l_c), and the pocket depth (d). The line of symmetry, shown in Figure 44, was used to reduce the model size.

A reasonable simulation runtime was necessary for this model due to the need to find a journal equilibrium position in some of the following studies. Performing such an optimization requires a series of simulations to be performed. Therefore, a mesh independence study was performed on the CFD model to balance the simulation time and results' accuracy. The journal position and jacking pocket geometry used in this mesh independence study are presented in Table 27. The journal position that was used was selected as it was the equilibrium position found for the case with the smooth pad surface. The results are presented in Table 28. Large changes in the peak pressure did not occur as the mesh density increased to the finer meshes. The 3 million element mesh was chosen to ensure accuracy of the results while also minimizing the runtime of the simulations.

Table 27: Fixed Eccentricity Position and Stadium-Shaped Jacking Pocket Geometry for Mesh Independence Study

x_j/C_b	0.4085
y_j/C_b	0.4508
l_a/L_a	0.47
l_c/L_c	0.12
d/C_b	10

Table 28: Mesh Independence Study

Number of Elements	Peak Pressure (MPa)	Percent Change (%)
225,000	5.88	-1.38
3,000,000	5.84	-0.61
9,000,000	5.80	-

4.4 Thermohydrodynamic Model

4.4.1 Thermohydrodynamic Equations

A TEHD solver was developed to analyze the capabilities of the Reynolds equation in solving for the performance of bearings with jacking features. This new code is largely based off of MAXBRG [59] and is called MAXBRG3D. MAXBRG solves the Reynolds equation, the energy equation, and the elasticity equations in two-dimensions. The new code has been expanded to account for all three dimensions in the energy and elasticity equations, as well as introducing axial variation into the Reynolds equation.

MAXBRG solves the modified, two-dimensional Reynolds equation given in Equation 4.1 with the turbulence factors given in Equations 4.2-4.5 [59].

$$\frac{\partial}{\partial x}\{h^3\Gamma(x,z)\frac{\partial p}{\partial x}\} + \frac{\partial}{\partial z}\{h^3\Gamma(x,z)\frac{\partial p}{\partial z}\} = -UG(x,z)\frac{\partial h}{\partial x} \tag{4.1}$$

$$\Gamma(x,z) = \int_0^1 \left[\xi_2(x,y,z) - \frac{\xi_2(x,1,z)}{\xi_1(x,1,z)}\xi_1(x,y,z)\right] dy \tag{4.2}$$

$$G(x,z) = \frac{1}{\xi_1(x,1,z)}\int_0^1 \xi_1(x,y,z)dy \tag{4.3}$$

$$\xi_1(x,y,z) = \int_0^y \frac{1}{\mu_e(x,y',z)} dy' \tag{4.4}$$

$$\xi_2(x,y,z) = \int_0^y \frac{y'}{\mu_e(x,y',z)} dy' \tag{4.5}$$

MAXBRG3D solves the same modified Reynolds equation but adds axial variation by expanding the film thicknesses equation. This film thicknesses equation is given in Equation 4.6. A new term (f_a) has been included which is a function of axial and circumferential position. This term was used to account for jacking pockets and can be used for other axially varying features as well.

$$\begin{aligned} h(\theta) = c_p - X_j cos(\theta) - Y_j cos(\theta) - \\ (c_p m) cos(\theta - \theta_p) - f_a(\theta, z) \end{aligned} \tag{4.6}$$

MAXBRG3D calculates the maximum Reynolds number in the bearing. If the flow is above a user specified value then the code will use Reichardt's formula [38] to calculate the eddy viscosity. These equations are shown in Equation 4.7 and Equation 4.8. These equations are valid for fully developed turbulence. A scaling factor is used to handle the transition from laminar to turbulence [69]. The results in this study had maximum Reynolds numbers of 300 which is well in the laminar regime.

$$\mu_e(x,y,z) = \mu\Big(1 + \frac{\epsilon_m}{\nu}\Big) \tag{4.7}$$

$$\frac{\epsilon_m}{\nu} = \kappa\Big[y^+ - \sigma_l^+ tanh\frac{y^+}{\sigma_l^+}\Big] \tag{4.8}$$

Under normal flow conditions, MAXBRG assumes no axial temperature variation. This assumption is based on the significantly higher circumferential velocities along with the high radial heat dissipation [70]. However, the assumption breaks down with the inclusion of axially varying features in the bearing. Therefore, MAXBRG3D solves the full energy equation given in Equation 4.9.

$$\begin{aligned} \rho C_p \left(u\frac{\partial T}{\partial x} + w\frac{\partial T}{\partial z} \right) = \frac{\partial}{\partial x}\left(k\frac{\partial T}{\partial x}\right) + \frac{\partial}{\partial y}\left(k\frac{\partial T}{\partial y}\right) + \\ \frac{\partial}{\partial z}\left(k\frac{\partial T}{\partial z}\right) + \mu_e\left[\left(\frac{\partial u}{\partial y}\right)^2 + \left(\frac{\partial w}{\partial y}\right)^2\right] \end{aligned} \tag{4.9}$$

MAXBRG3D utilizes 9 node, two-dimensional elements for the Reynolds equation and 27 node, three-dimensional elements for the energy and elasticity equations. Quadratic shape elements are used to describe the behavior of

Table 29: Mesh Densities and Approximate Solution Time

Number of Elements	Number of Nodes	Approximate Solution Runtime (s)
336	1.42e3	18
792	3.29K	96
1.58K	6.53K	750
10.5e3	42.4K	42e3
29.4e3	118K	259e3

the nodal values throughout each of the elements. Another advantage of these shape functions was the ability to model of complicated pocket shapes without drastically increasing the mesh size. The CFD stadium-shaped, jacking pocket study in Chapter 2 contained a small discussion of the use of Reynolds equation in analyzing bearings with jacking pockets. This work utilized linear shape functions. It is hypothesized that the use of quadratic functions will limit the errors seen previously with deep pockets.

4.5 MAXBRG3D Mesh Density Study

A hydrodynamic study was done to better understand the influence of the mesh density on the results of the Reynolds equation. The same stadium geometry and journal eccentricity position were used as were presented in Table 27. Five meshes were used varying from three hundred to twenty nine thousand elements. The number of nodes in each mesh increase at a higher rate than the number of elements. Therefore the greater mesh densities can be taxing to the available computational resources, especially memory, and can have very large runtimes. Table 29 shows the different meshes along with approximate runtimes for a single solution of the Reynolds equation. These five meshes were used to examine bearings with pockets of three different depths. A shallow pocket depth of $0.28 \times C_b$ was chosen as this was the case with the highest load capacity (Chapter 2). A deep pocket $6.6 \times C_b$ deep was chosen as this was the limit at which the pressure change became negligible. Lastly, a depth of $1.1 \times C_b$ was selected as it lies between the deep and shallow pocket cases. Figure 45-47 show the resulting centerline pressures for each mesh alongside the CFD results.

Based on Figure 46 a good solution for a shallow pocket was achieved with a mesh of 1500 elements. The 300 and 700 element meshes show fairly good results, although they slightly overpredict the peak pressure. The $1.1 \times C_b$

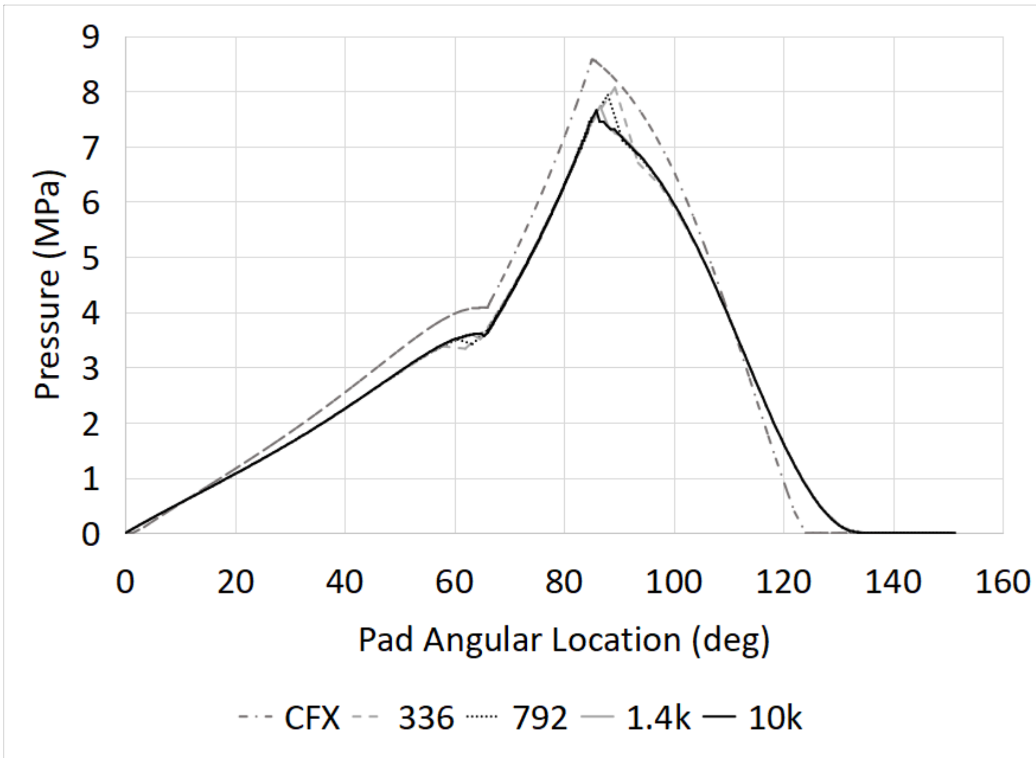

Figure 45: Centerline pressure of pad with $0.28 \times C_b$ depth stadium-shaped, jacking pocket for various mesh densities

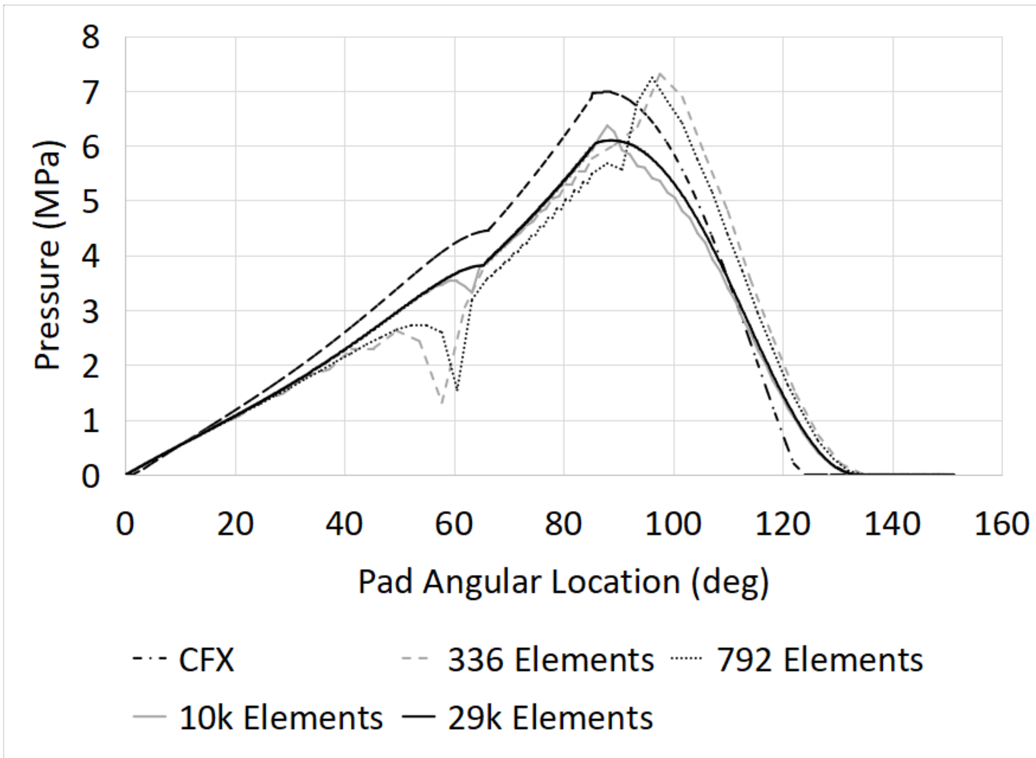

Figure 46: Centerline pressure of pad with $1.1 \times C_b$ depth stadium-shaped, jacking pocket for various mesh densities

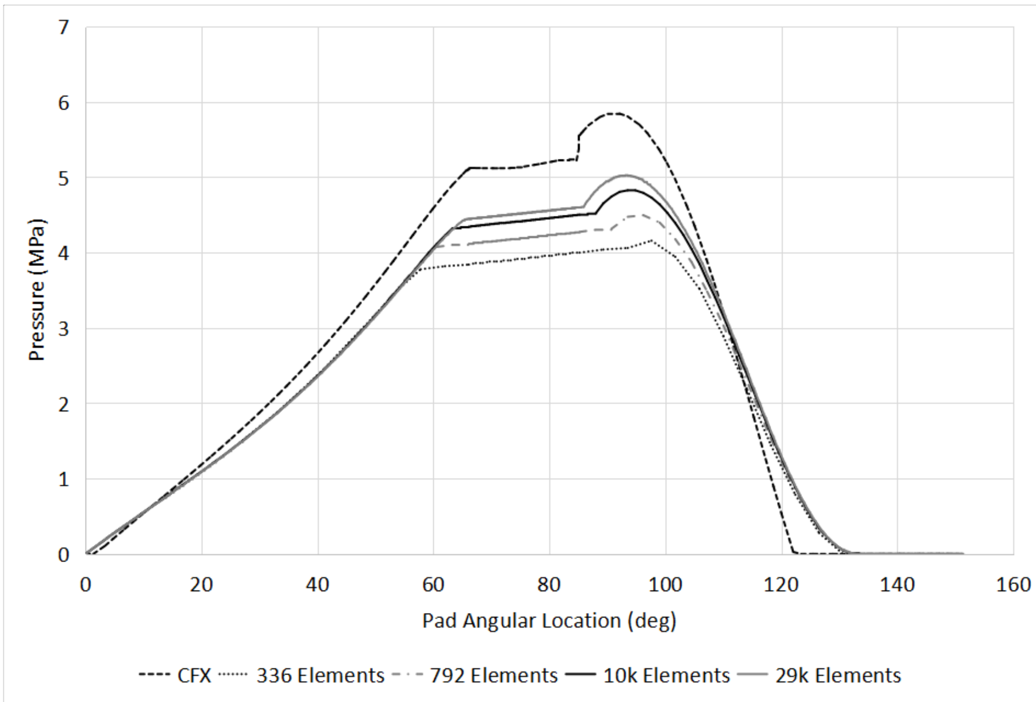

Figure 47: Centerline pressure of pad with $6.6 \times C_b$ depth stadium-shaped, jacking pocket for various mesh densities

deep case was the most mesh density dependent of the three cases. It required approximately twenty nine thousand elements for a good solution. The ten thousand element mesh had fairly good results but had a higher peak pressure and had a low pressure point right at the leading edge of the pocket. Figure 46 shows that both of these trends are numerical in nature. As the mesh density increases, they disappear. As seen in Figure 47, the deep pocket results require a mesh of around ten thousand elements before the change in solution isn't significant. The coarse meshes underpredict the pressure across the pocket and reduce the pressure rise downstream of the pocket.

4.5.1 Step Scaling Method

A numerical method was investigated for getting solutions for deep pockets in a more reasonable amount of time. The film thickness is a nodal value which has a distinct value at each of the 9 nodes in the two-dimensional Reynolds equation mesh. The quadratic shape functions are used to determine the film thickness throughout the element. Based on the film thickness equation (Equation 4.6) and the axial functions used to account for the jacking groove, the nodes on the border of the pocket have film thickness of at least the pocket depth greater than their neighbors that are not in the pocket. A three-dimensional visualization for neighboring elements at the pocket border is shown in Figure 48. Six of the nodes in the element 1 are outside of the pad and have a larger height (lower film thickness) than the remaining three nodes which are on the border of the pocket. These nodes at the border have the pocket depth added onto the film thickness that occurs due to the journal eccentricity. A curve is shown which approximates the pad height across the element 1. Across the first half of this element, there is a slight decrease in film thickness (increase in pad height) due to the quadratic shape functions. As the elements on the border of the pocket decrease in size, this loss in film thickness decreases.

A method referred to as step scaling was proposed to achieve an approximate solution with fewer elements. This method involves separating the mesh into two regions: the pocket region and the land region. These two mesh regions can be solved separately but coupled together by using a pressure boundary condition. This separation is done by allowing the shared nodes on the border of the pocket to have two values for the film thickness. When adding element 1 to the global matrix, the pocket depth is not included in the film thickness calculation. However, the depth is included when the elemental matrix for element 2 was calculated. Figure 49 shows a similar three-dimensional visualization. Each of the shared nodes on the pocket border have two distinct film thickness values. This method does not

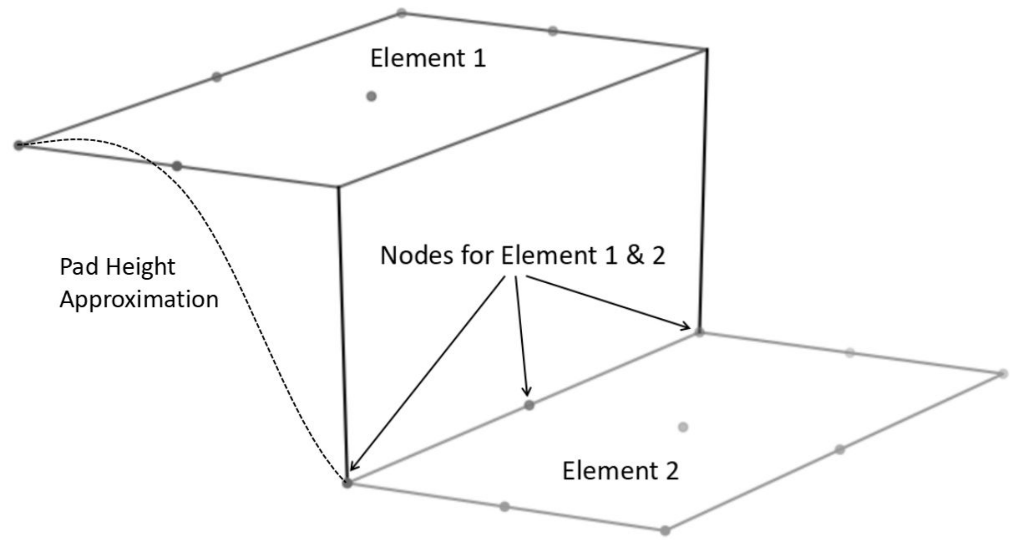

Figure 48: Pocket edge with no step scaling

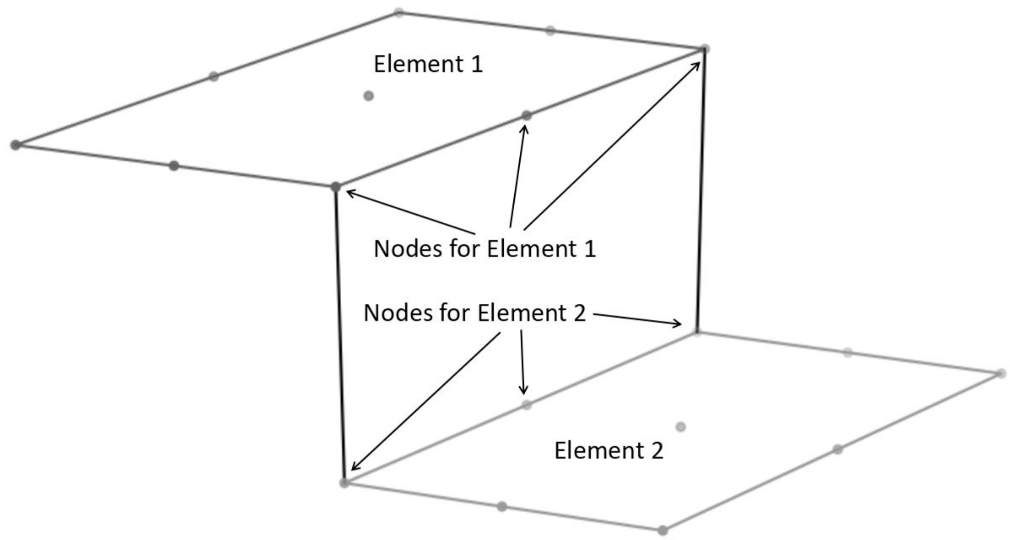

Figure 49: Pocket edge with step scaling

preserve the mass flow continuity around the edge of the pocket.

As deep pockets do not experience large pressure changes across the pocket, it was hypothesized that this method would be best suited for approximating bearings with these pockets. Figure 50 shows the centerline pressures for each of the different meshes while utilizing the step scaling method. All

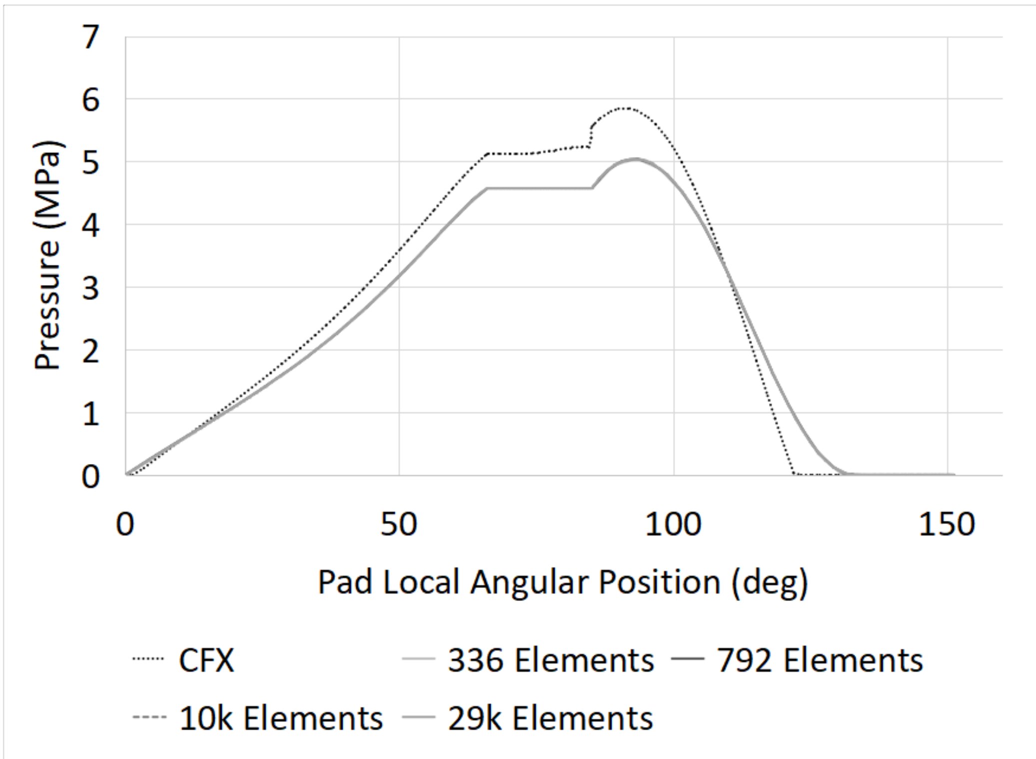

Figure 50: Centerline pressure of pad with $6.6 \times C_b$ depth stadium-shaped, jacking pocket for various mesh densities with full step scaling

of the different meshes resulted in the exact same solution. This allows the use of the sparse mesh, which greatly reduces the required runtime. This solution did result in a completely constant pressure across the pocket whereas the CFX solution did have a slight increase across the pocket. This trend of identical solutions held true across the whole range of depths for all of the meshes using this method. This method could be applied with even fewer elements than is presented in this dissertation with the same results.

4.5.2 Mesh Distribution

To solve the flow using finite element analysis, the pad surface was meshed by breaking the mesh into 5 different regions that are shown in Figure 51. The area inside the pocket (region 3) was meshed uniformly on an isometric square and mapped to the stadium shape. The regions above and below the pocket (regions 4 and 5) were meshed in the same way. The regions upstream and downstream of the pocket (regions 1 and 2) were meshed with a uniform distribution circumferentially. However, the axial distribution corresponded

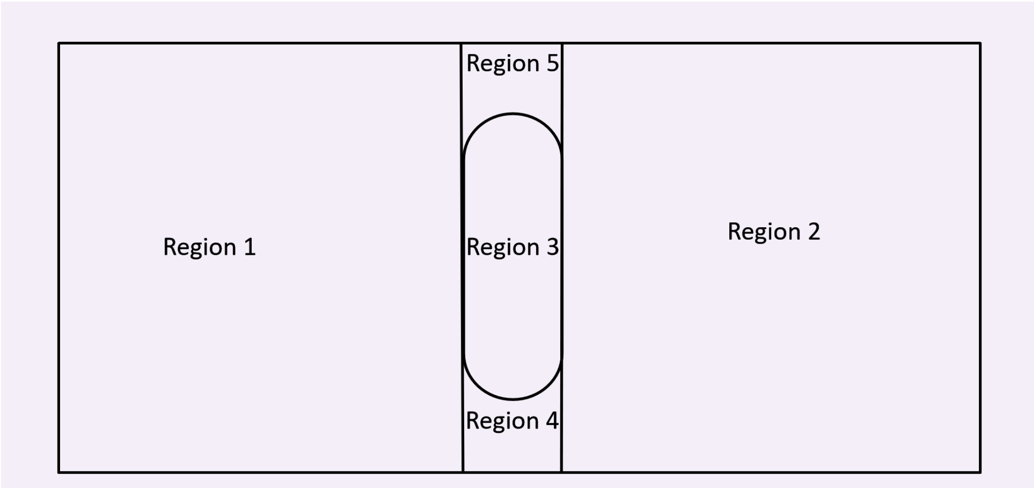

Figure 51: Map of different regions used to mesh the stadium shaped jacking pocket on the pad surface

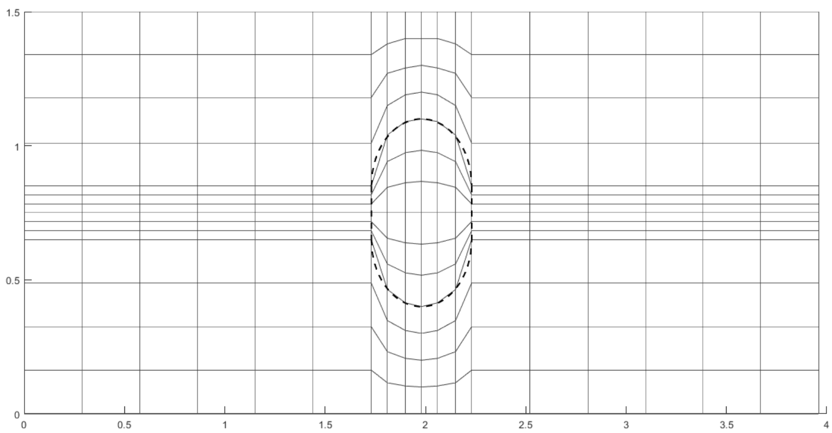

Figure 52: Mesh of pad surface with stadium-shaped jacking pocket with no element biasing

to the axial distribution of regions 3, 4, and 5. This resulted in a tight band of elements to either side circumferentially of the leading and trailing edges of the pocket. Figure 52 shows an example mesh.

Another method that was examined to allow the use of sparser meshes was to bias all of the elements towards the pocket. In each of the four regions bordering the pocket, a bias was applied to shift more of the elements towards the pocket. Regions 1 and 2 were biased circumferentially, while regions 4

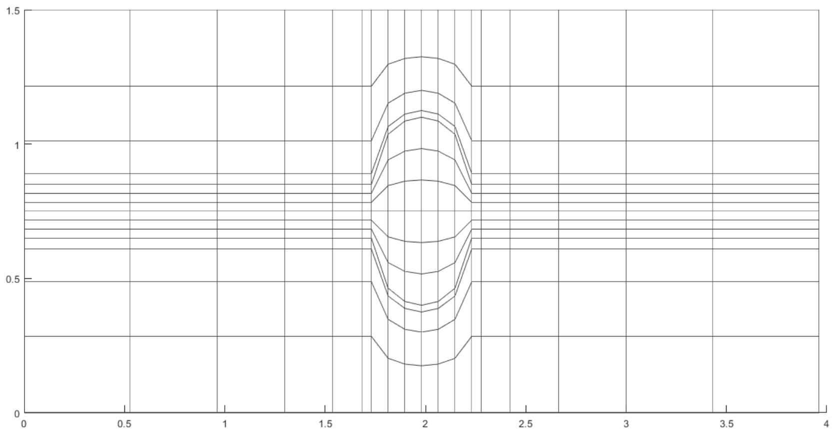

Figure 53: Mesh of pad surface with stadium-shaped jacking pocket with element biasing toward the pocket

and 5 were biased axially. The bias that was used was a quadratic function. The resulting mesh is shown in Figure 53. A small band of elements can be seen on all sides of the pocket. These smaller elements decrease the loss of film thickness that is introduced by the use of quadratic elements (Figure 48).

A similar mesh independence study was performed for each of three different depths. The centerline pressure results of this study are shown in Figure 54-56. The shallow pocket now achieves a stable solution with the 300 element mesh as seen in Figure 54. This represents a 98% reduction in simulation runtime. Figure 55 shows the solution for the $1.1 \times C_b$ deep pocket. In this case, the 792 element mesh resulted in a stable solution. The solution using 336 element mesh was good but still had some slight numerical oscillation occurring in the pressure rise across the pocket. This resulted in a 99.7% reduction in simulation time compared with the unbiased mesh results. The deep pocket results are presented in Figure 56. The 300 element mesh is an excellent solution and had minimal differences from any of the finer meshes. The unbiased mesh required at least 1500 elements. The same 98% reduction in run time as seen in the $0.28 \times C_b$ deep pocket occurs when using the biased mesh with the deep pocket.

4.6 Thermal Model

Based on several CFD simulations, a trend was noticed of fairly constant average film temperature across the pocket. Based on this a simplified ther-

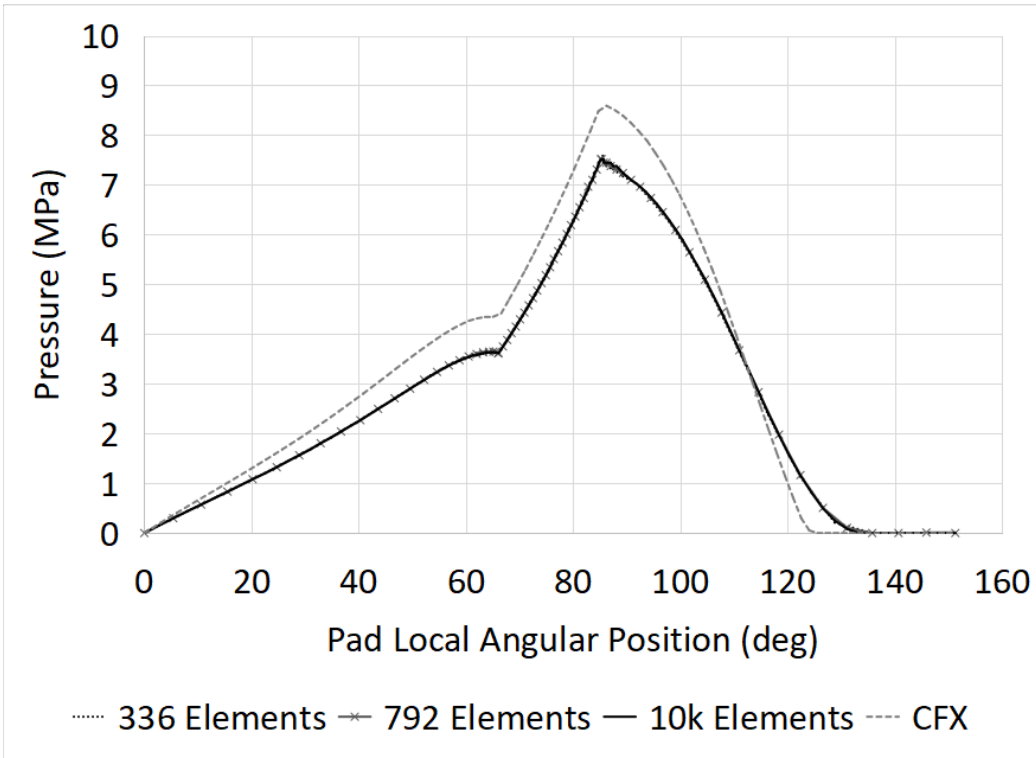

Figure 54: Centerline pressure of pad with $0.28 \times C_b$ depth stadium-shaped, jacking pocket for various mesh densities with biased mesh

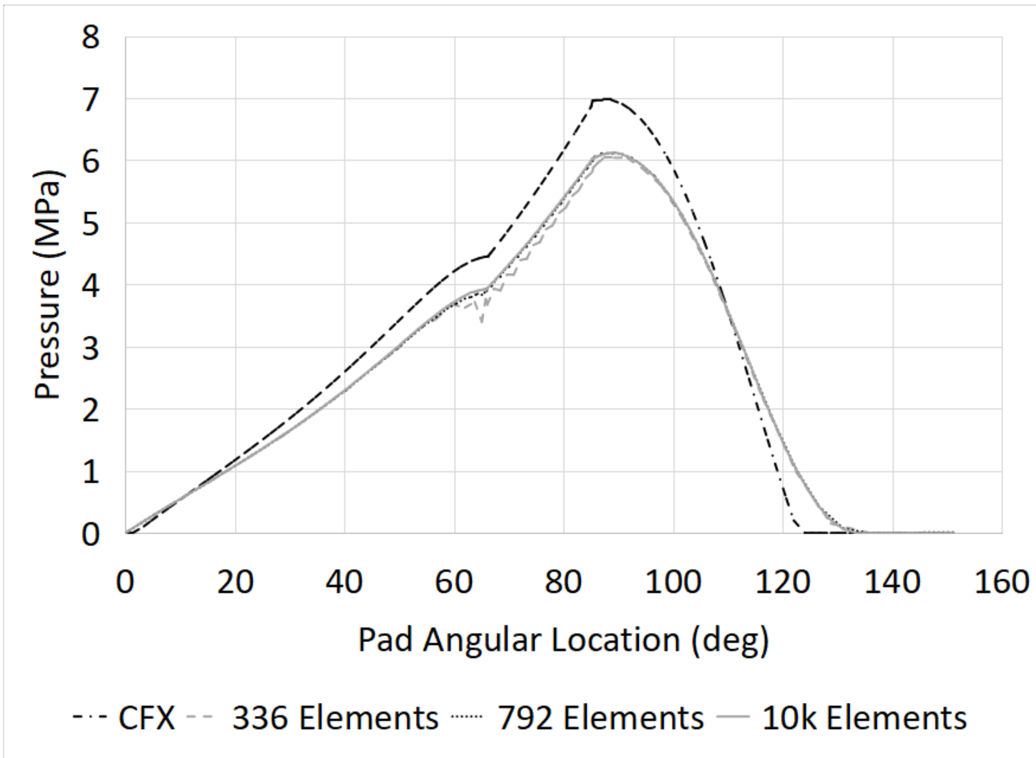

Figure 55: Centerline pressure of pad with $1.1 \times C_b$ depth stadium-shaped, jacking pocket for various mesh densities with biased mesh

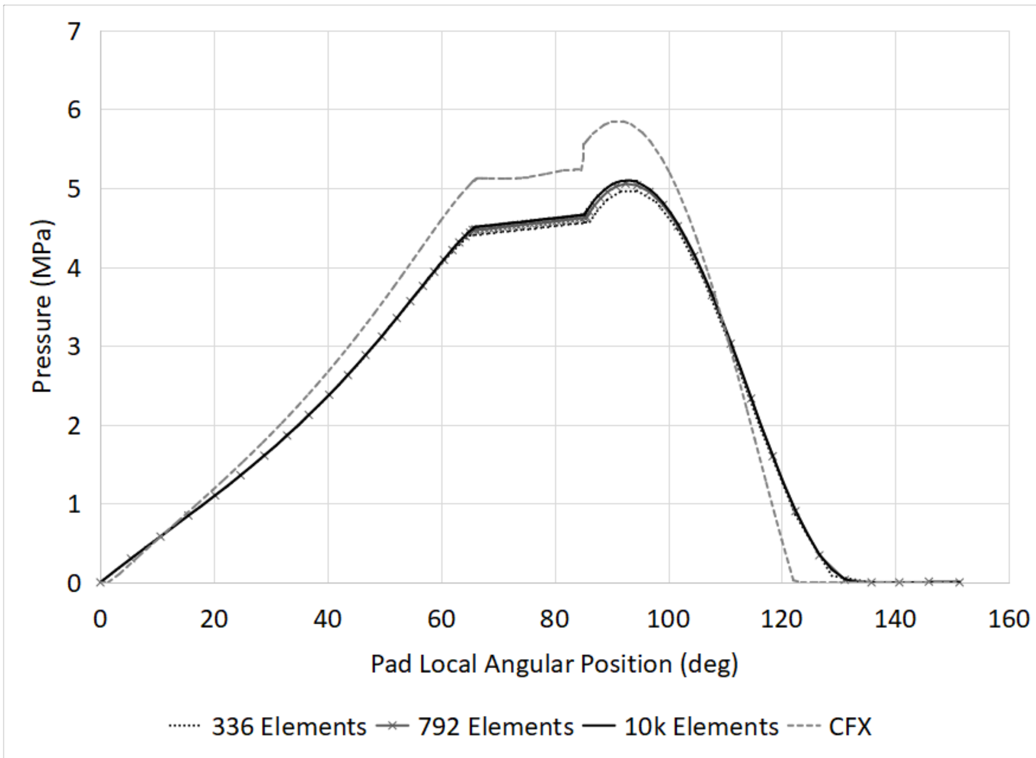

Figure 56: Centerline pressure of pad with $6.6 \times C_b$ depth stadium-shaped, jacking pocket for various mesh densities with biased mesh

mal solution is proposed to achieve accurate results without having to model the complex velocity in the pocket. The 3D energy equation (Equation 4.9) was solved ignoring the presence of the pocket and the heat generation term in the flow above the pocket.

4.7 Varying Depth Studies

4.7.1 Pinned Eccentricities Study

In the previous CFD study on stadium-shaped jacking pockets, the influence of the pocket depth was examined across a range of pocket depths. This same study was repeated using MAXBRG3D. The pocket geometry and position of the journal are the same as used in the mesh independence study (Table 27). The pocket depth was varied from $0.01 \times C_b$ to $6.6 \times C_b$. The CFD cases were rerun with 1% of the fluid density (negligible inertial effects) to make better comparisons with the Reynolds equation results. The whole range of pocket depths were simulated in MAXBRG3D using the three methods mentioned above and compared with CFD.

Initially in the CFD results, the load capacity of the bearing increased as the pocket depth increases. This increase in load peaked at a depth of $0.28 \times C_b$. After this, the load capacity droped by 11% at a pocket depth of $6.6 \times C_b$ and deeper. Figure 57 and Figure 58 show how the step scaling method performed across the range of depths, along with the CFD results. The step scaling completely failed to capture the first regime where the pressure increased. The slope of the pressure across the pocket immediately started falling towards a constant pocket pressure. The final pressure profile is achieved at a depth of about $3 \times C_b$ in contrast with the $6.6 \times C_b$ seen using CFD. Based on this, this method is not valid for modeling jacking pockets unless the pockets are deep.

The next plots (Figures 59-60) show a comparison between the results of the unbiased and the biased meshes. The unbiased cases were run using either the twenty nine thousand element or the ten thousand element meshes. These high density meshes were required to get smooth results for depths between $0.5 \times C_b$-$3.0 \times C_b$. The biased case was run using the 700 element mesh. The results for these two different meshes were identical with the exception of the case with a pocket depth of $0.5 \times C_b$. This depth required the 1400 element mesh while utilizing biasing. Figures 59-60 show the curves across all of the depths range. The results were the same for all cases. As both methods achieve similar results, the biased mesh is recommended due to its greatly reduced runtime.

Figure 61 shows the first regime comparing CFD with the MAXBRG3D

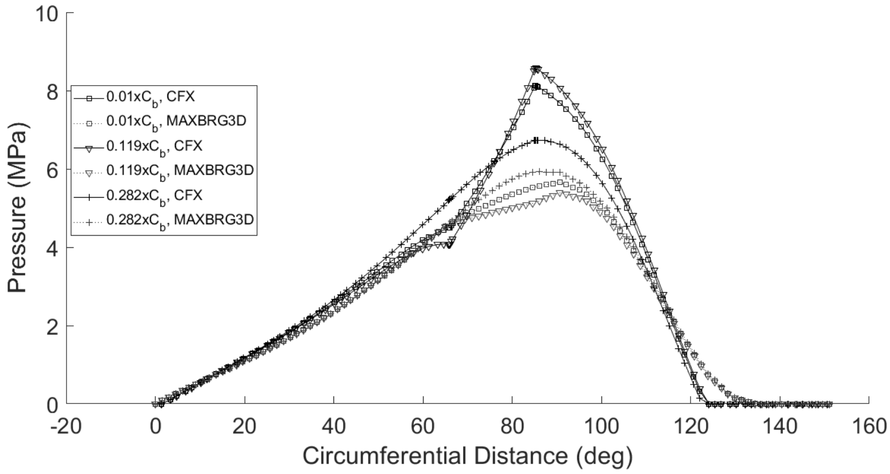

Figure 57: Pressure profiles in regime 1 using CFD and MAXBRG3D with step scaling method

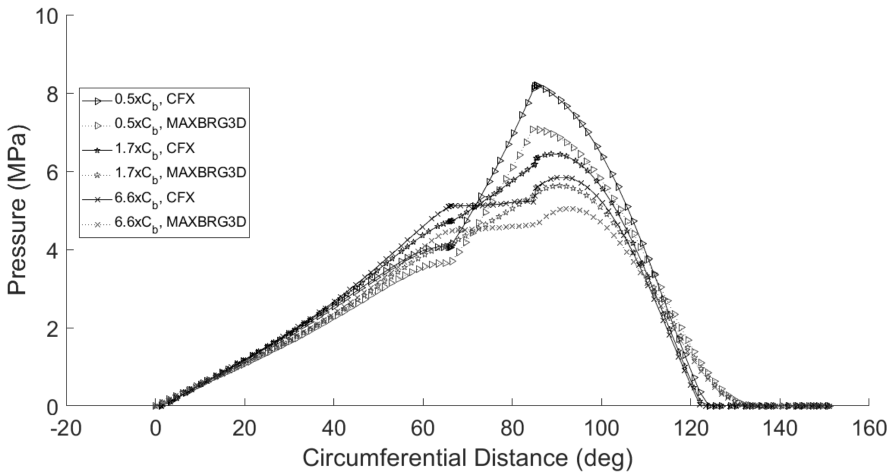

Figure 58: Pressure profiles in regime 2 using CFD and MAXBRG3D with step scaling method

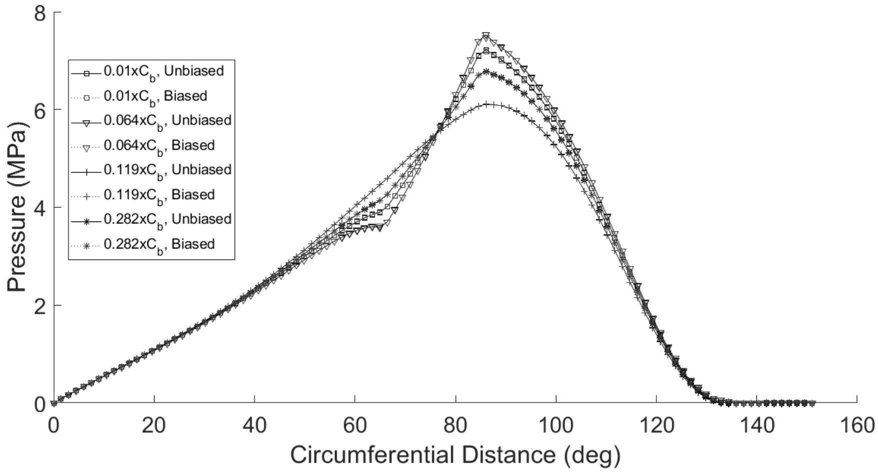

Figure 59: Pressure profiles in regime 1 using MAXBRG3D with biased and unbiased meshes

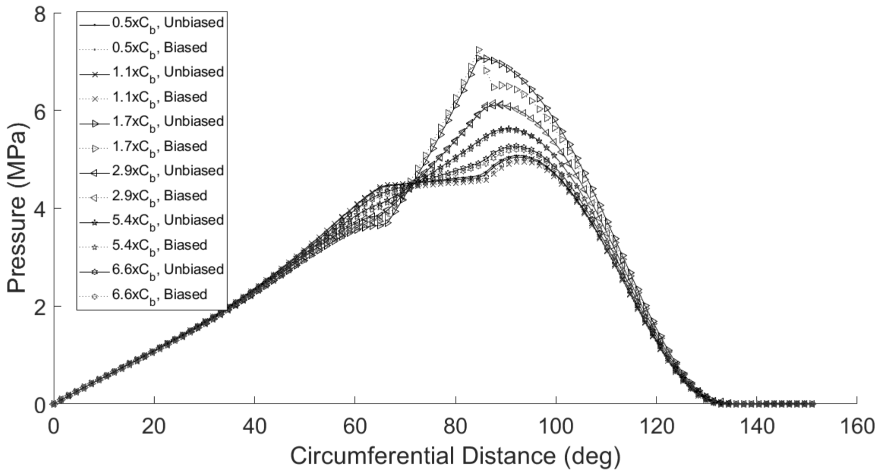

Figure 60: Pressure profiles in regime 2 using MAXBRG3D with biased and unbiased meshes

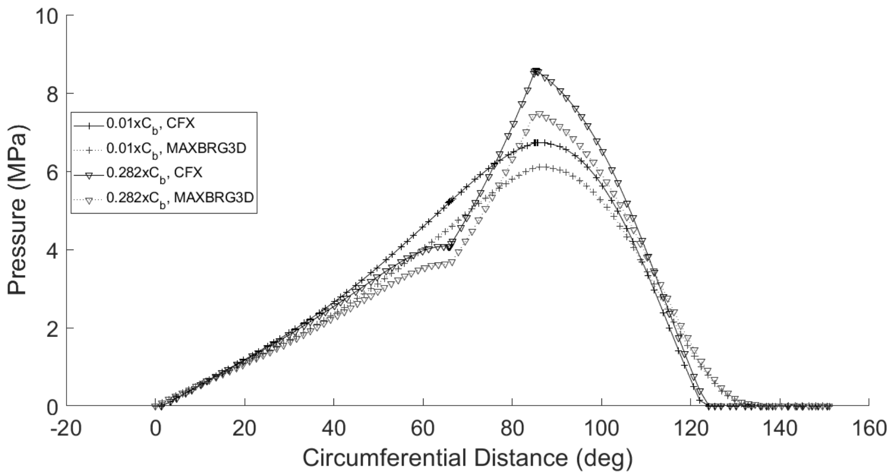

Figure 61: Pressure profiles in regime 1 using CFD and MAXBRG3D with biased mesh

results using the biased mesh. The results are very similar in shape, although pressures developed using the Reynolds equation were almost exactly 90% of the CFD results. Figure 62 plots this comparison of the biased mesh with the CFD results multipled by a factor of 0.9. These results matched up very well. The second regime is plotted in Figure 63 for the actual CFD results. Again the trends calculated by the Reynolds equation correlated very well to the CFD results but were 10% lower. The 0.9 factor yielded similar results across this regime as well.

The Reynolds equation is capable of capturing all of the trends seen in CFD. It did underpredict the film pressure by about 10% of the CFD pressure. Solving the Reynolds equation using the step scaling method around the border of the pocket, while the fastest method requiring the fewest elements, only produces good results for bearings with deep pockets ($> 6.6{\times}C_b$). The biased mesh is the superior method for using the Reynolds equation for analyzing bearings with jacking pockets for pockets of all depths. It allowed for the sparsest meshes and could accurately solve for the whole range of depths. This method optimizes simulation time with accurate results.

4.7.2 Optimized Eccentricities Study

A design-of-experiments was used in Chapter 2 to examine the bearing performance of the Neal and Fitzgerald [58] bearing with a stadium-shaped, jacking pocket using CFD. Fifteen different stadium-shaped, jacking pocket geometries were developed. The Nelder-Mead algorithm was used to find the

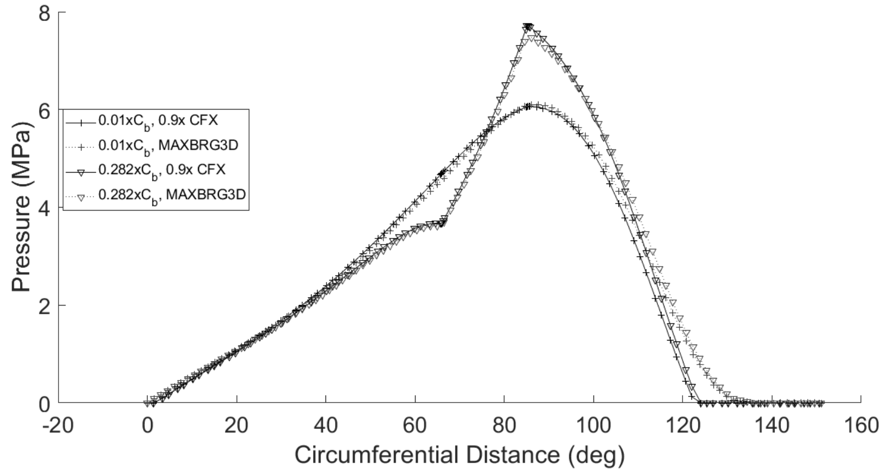

Figure 62: Pressure profiles in regime 1 using CFD multiplied by a factor of 0.9 and MAXBRG3D with biased mesh

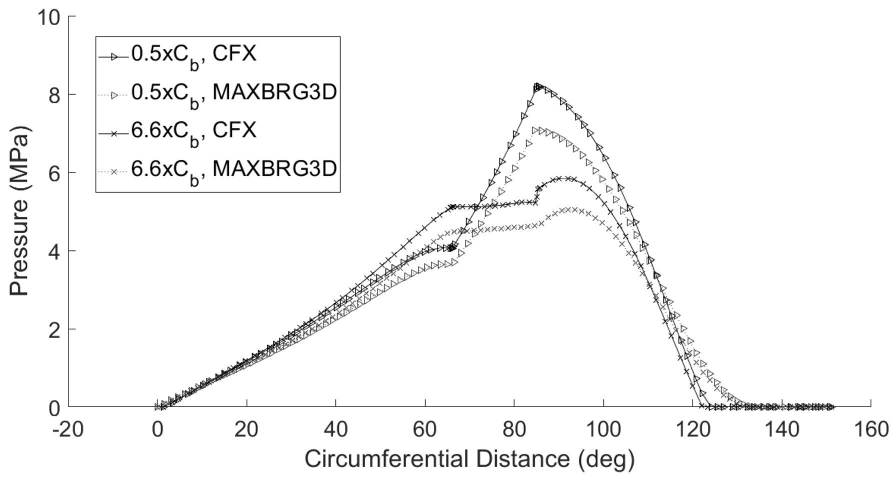

Figure 63: Pressure profiles in regime 2 using CFD and MAXBRG3D with biased mesh

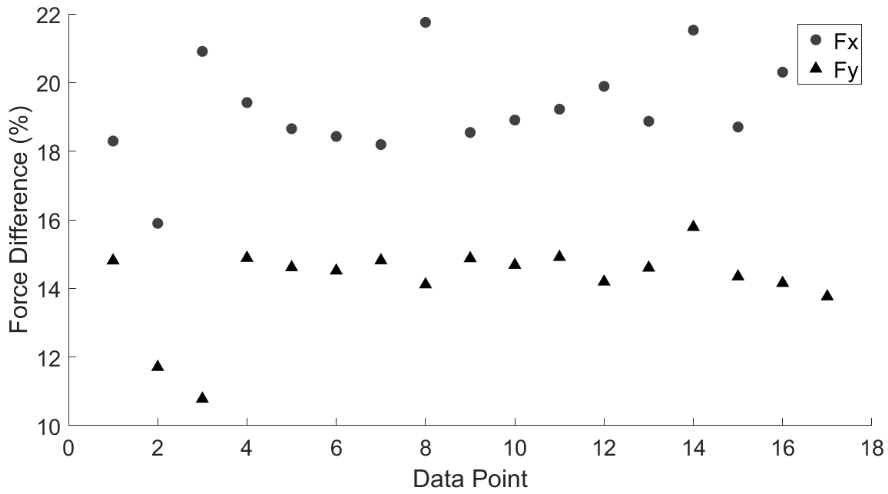

Figure 64: Difference between the hydrodynamic forces predicted by CFD versus MAXBRG3D when pinned at the same journal eccentricity

steady-state, journal equilibrium position. Fluid inertia was included in this model.

MAXBRG3D was run with the same fifteen jacking pocket geometries. Initially it was run with the journal eccentricity position set to the values found previously using CFD. The pressure profiles and hydrodynamic forces were expected to be lower than the CFD results based on the lack of inertia in MAXBRG3D. The difference between the MAXBRG3D results and CFD results as a percent of the CFD are presented in Figure 64. The horizontal force varies between 18-22% aside from the one outlier at 16%. The vertical forces varied between 14-15% with two outliers at 12% and 11%.

In the second portion of this study, MAXBRG3D was allowed to iterate on the solution to find an equilibrium position for the rotor. The eccentricity positions found using MAXBRG3D were expected to be larger than those found using the CFD. As the journal was closer to the pad surface this resulted in lower film thicknesses and higher pressures. This increase in pressure was expected to offset the pressure increase due to inertia found in the CFD. Figure 65 shows the eccentricity positions, nondimensionalized by the radial clearance, of each of the different designs. The scale on both axes has been increased for better clarity. The lack of inertia causes a drop in the eccentricity in the y-direction of about $0.04 \times C_b$, along with a slight shift in the x-direction. The dimensionless eccentricity varied by 0.037-0.032, while the attitude angle varied by $2.07 - 3.09°$. The eccentricity positions did not change significantly in any of the cases and would be unlikely to have

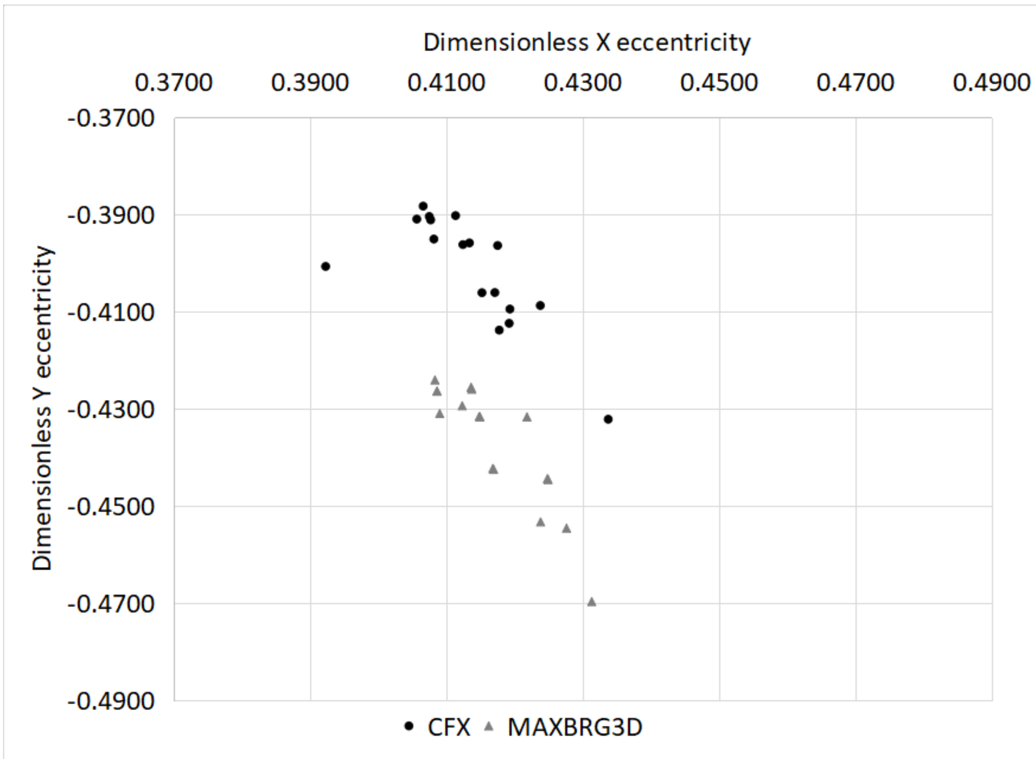

Figure 65: Difference between the equilibrium journal positions predicted by CFD versus MAXBRG3D

Table 30: Fixed Eccentricity Position and Stadium-Shaped Jacking Pocket Geometry for Mesh Independence Study

Case Number	$\bar{l}_a/L_a$	$\bar{l}_c/L_a$	$\bar{d}/C_b$
1	0.41	0.13	7.6
3	0.87	0.10	5.3
9	0.41	0.13	2.9

a significant effect on the thermodynamics of the bearing, which is often the main concern with lower film thicknesses.

The centerline pressure profiles of three of the cases are presented in this chapter. These cases along with their geometry are presented in Table 30. They were chosen as they well represented the range of different responses. The centerline pressure profiles are shown in Figures 66-68. The MAXBRG3D results have the same profile shape as the CFX when

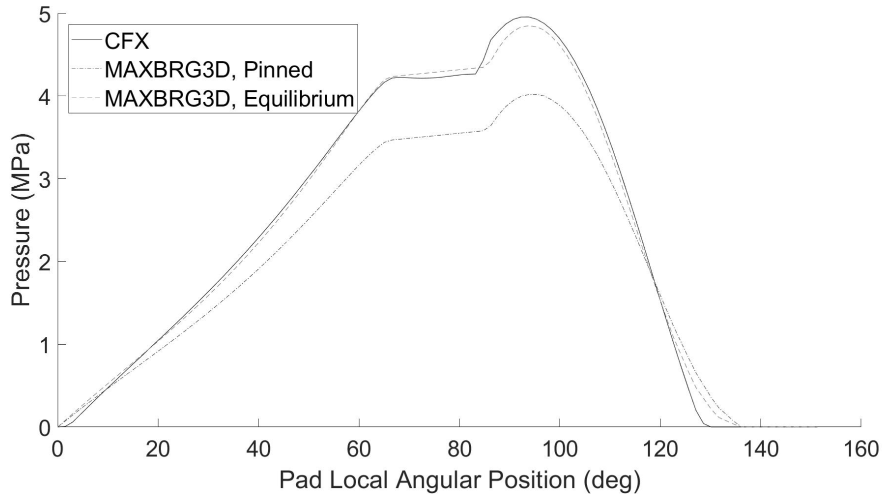

Figure 66: MAXBRG3D and CFD centerline pressures for bearing with case number 1 pocket geometry

pinned at the same eccentricity, despite the overall lower pressures. When MAXBRG3D is allowed to iterate to an equilibrium solution, the pressure profiles match up almost exactly. In case number 3, the pressure profile drops as it enters the pocket. The axial length of the pocket design was very long, and the pocket served to move fluid from the high pressure region in the center of the bearing to the lower pressure areas along the axial edges. This caused the drop in the pressure seen in Figure 67.

4.8 Conclusions

The goal of this chapter was to further the understanding about the validity of using the Reynolds equation to solve for fluid-film, journal bearings including jacking features. This was achieved by comparing results of the Reynolds equation to results from an experimentally verified CFD model. The two-pad bearing contained a single stadium-shaped, jacking pocket on the bottom, loaded pad.

Several different meshing methods for use with the Reynolds equation were examined to find a good solution in a reasonable amount of time. The first method involved using evenly distributed elements across the pad, while still placing nodes around the pockets' border. The second method (step scaling method) involved solving for the pocket region and the land region separately with a shared boundary condition at the border of the pocket. The last method was to bias the elements in the land region towards the

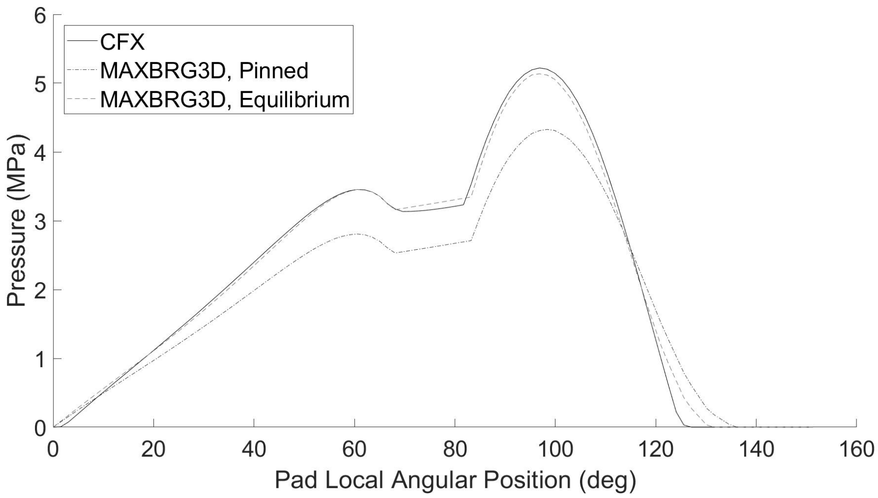

Figure 67: MAXBRG3D and CFD centerline pressures for bearing with case number 3 pocket geometry

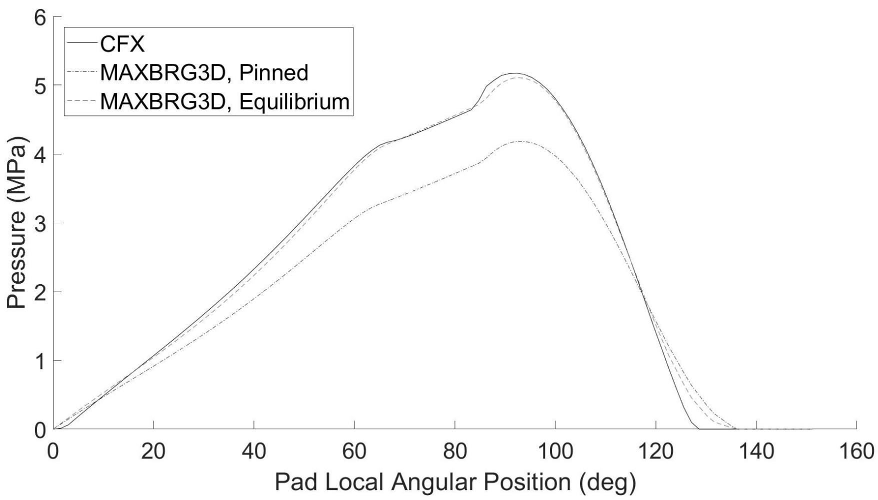

Figure 68: MAXBRG3D and CFD centerline pressures for bearing with case number 9 pocket geometry

pocket. A series of mesh density studies of each of the different methods was performed. The biased mesh and the step scaling method could converge to stable solutions with significantly fewer elements. Each of these methods were then used to examine the pressure profile as the pocket depth varied from $0.01 \times C_b$ - $6.6 \times C_b$. The step scaling method did not correlate well with any of the CFD data besides the deep pocket case ($6.6 \times C_b$). Both the biased and unbiased mesh solutions achieved similar results, although the unbiased mesh was significantly more dense and took much longer to run. Biasing the elements was found to be crucial to getting accurate solutions in a reasonable amount of time for anything besides deep pockets. This biasing reduces the size of the elements around the border of the pocket which reduces the error introduced by the step change in film thickness due to the quadratic shape functions.

Lastly several different pocket geometries were examined, with both pinned and optimized equilibrium shaft positions, and compared with CFD results. Although the Reynolds equation underpredicts the pressure in the bearing for a fixed film shape, it does capture the shape of the profile accurately. The prediction will be excellent when the Reynolds solution can iterate to find an equilbrium journal position. This will be slightly higher than the eccentricity found by iterating on the CFD solution, which includes the inertial effects. This increase, however, is not significant and is conservative in terms of safe bearing performance. This means that the film thickness will be slightly smaller and will result in slightly hotter bearing temperatures. These new temperatures won't be significant but will result in a slightly safer bearing design.

This chapter demonstrates how the Reynolds equation can successfully be used to capture the physics that occur in a fluid-film, journal bearing containing jacking pockets. Biasing should be used to ensure that thin elements exist around the border of the pocket while not requiring extremely large meshes. Although the Reynolds equation underpredicts the pressure in the bearing for a given journal position, this difference doesn't exist when the journal is allowed to find its own equilibrium position. The change in journal position will result in a slightly more conservative bearing design.

5 Turbulence Modeling in Thin Film Applications

Nomenclature

y^+_{mesh} Nondimensional distance from wall of first element layer in the mesh
τ_{ij} Turbulence shear stress
μ_t Turbulence eddy viscosity
S_{ij} Mean rate of strain tensor
ρ density
k Turbulence kinetic energy
δ_{ij} Kronecker delta
y^+ Nondimensional distance from wall
u_* Friction velocity
y Distance from wall
ν Kinematic viscosity
ω Specific rate of dissipation
ϵ Rate of dissipation of turbulent energy
C_b Bearing radial clearance
h Film thickness

5.1 Introduction

Turbulence can be an important feature that many studies have ignored or considered improperly. Turbulence is a deviation from the stable laminar flow conditions, in which the fluid moves in layers, to a more irregular flow. While a turbulent flow is characterized by randomness with respect to both time and spatial coordinates, it can be characterized by statistically distinct average values [23]. Turbulence is caused by high friction forces at a wall or between different fluid layers of varying velocities. The viscosity of the fluid dampens out turbulence as more viscous fluids can absorb more of the kinetic energy [24]. Predicting the transition from laminar to turbulent flow is difficult and not well understood. Turbulence can have a significant influence on the operation of fluid-film journal bearings. This is especially true for bearings operating at high speeds or which use low viscosity fluids, such as water, as the working fluid. Turbulence will begin to occur locally in flows with Reynolds numbers of 2000 and higher, where $Re = r\omega h/\nu$ is the local Reynolds number [26, 27].

Initially while performing the CFD studies in Chapter 2, it was hypothesized that the jacking pocket might induce turbulence in the film due to the increased film thickness. Therefore the initial model of Fitzgerald and Neal [58] bearing was created with a SST k-ω turbulence model. This turbulence model was chosen based on its common use in literature and the y^+_{mesh} values in the mesh. The pressure profile using this model resulted in a 20% drop in the peak pressure, which disagreed with what has been reported in literature[32, 33, 25]. Based on this disagreement, an investigation was performed on the appropriate use of different turbulence models in fluid-film bearings.

The onset of turbulence causes an increase in the heat transfer in the film resulting in lower film temperature. Szeri [28] found that the onset of turbulence causes a decrease in the maximum pad temperature. Hopf and Schüler [29] confirmed this behavior and found that this drop in temperature occurs in the vicinity of the minimum film thickness where the largest variation in temperature exists. They attributed this behavior to the mixing and increased heat transfer in the presence of high thermal gradients. Therefore, turbulent bearings will often run with lower peak temperatures than laminar bearings. However, as the turbulence increases this cooling effect is offset by an increase in heat generation [26, 30, 31]. Turbulence will usually result in an improvement in the load capacity of the bearing due to the increased radial motion in the film acting on the journal. As a result of the change in temperature and the improved load capacity, the turbulence will alter the equilibrium position of the rotor [32, 33, 25]. This, along with the thermal changes of the fluid characteristics, will alter both the stiffness and damping characteristics of the film. Turbulence also causes an increase in the power loss of a bearing which can be up to 1000 horsepower in bearings larger than 31 inches in diameter [34].

To solve the inherent closure problem that occurs in turbulence problems, Boussinesq [35] related turbulence shear stress to the mean flow variables using Equation 5.1.

$$\tau_{ij} = 2\mu_t S^*_{ij} - \frac{2}{3}\rho k \sigma_{ij}, \tag{5.1}$$

where τ_{ij} is the Reynolds stress tensor, μ_t is a proportionality constant called the eddy viscosity, S^*_{ij} is the trace-less mean strain rate tensor, ρ the fluid density, k is the turbulent kinetic energy, and δ_{ij} is the Kronecker delta. This relationship is used in a branch of turbulence models known as eddy viscosity models. The primary distinction between the different eddy viscosity models is the method by which the eddy viscosity term is calculated. These models are categorized by the number of differential equations that are required to solve for the eddy viscosity. Zero-equation models relate the eddy viscosity algebraically to various flow parameters. One-equation models add a differential equation to solve for the turbulent kinetic energy (k). Two-equation models add an additional equation that solves for some form of the turbulent dissipation (ϵ, ω). Both the one and two-equation models algebraically relate these new turbulent parameters to the eddy viscosity.

In his dissertation in 1970, Hanjalick [40] developed a turbulence model with two partial differential equation which are solved for the turbulent kinetic energy (k) and the turbulent dissipation rate (ϵ). These values are algebraically used to solve for the turbulent eddy viscosity term. To apply the model to the viscous sublayer, Jones and Launder [41] added viscous diffusion, Reynolds number dependent functions, and additional terms to take into account the nonisotropy of the dissipation processes. This model is known as the k-ϵ turbulence model and was further validated in Launder and Sharma [42].

In 1988, Wilcox [43] made a review of the current two-equation turbulence models and determined that these models failed to accurately predict boundary layer flow in the presence of an adverse pressure gradient and developed a new model to better account for this short coming. This model was further improved to account for misalignment of the Reynolds stress tensor and the mean strain rate tensor principle axes [44] and is known as the k-ω turbulence model. Menter [45, 46] further developed the model developed by Wilcox [43] to remove the dependence on arbitrary free stream values. This was achieved by using the Wilcox [43] model for the first 50% of the boundary layer and then transitioning the model to a k-ϵ model [41] in a k-ω formulation. This model is known as the Baseline(BSL) k-ω model. Menter [45, 46] made further modifications to the BSL model to allow this altered model to account for transport of shear stresses in the presence of an adverse pressure gradient in the boundary layers. This new model is called the Shear Stress Transport (SST) k-ω model.

In 1997 Mentor [47] combined Bradshaw's assumption [48], in which the turbulent kinetic energy is assumed to be proportional to the turbulent shear stresses, with the k-ϵ turbulence model to develop a one-equation turbulence model known as the Eddy Viscosity Transport model. Reynolds equation uses a thin film approximation to reduce the Navier-Stokes equations into a single differential equation. There have been numerous modifications made to the Reynolds equation to incorporate a turbulence model. A zero-equation, eddy viscosity model is usually used [49, 50, 51].

With the increase in computational power, the use of computational fluid dynamics (CFD) to solve the full or steady Navier-Stokes equations in the analysis of the operation of fluid-film bearings has become more prevalent. The proper use of turbulence models is important in fully understanding the behavior of the bearing. Unfortunately, many of the papers utilizing CFD neglect to mention the Reynolds number and turbulence model that were used. Those papers which do specify a turbulence model tend to heavily favor the two-equation turbulence models although a justification for this choice is generally not given. For example, Ravikovich et. al. [52] performed a steady-state CFD study on three different bearings which used water, oil, and gas as the operating fluid. They used the SST k-ω turbulence model for all of the bearings despite the large variance in Reynolds numbers. The oil bearing was operating at a Reynolds number below 5, while the water and gas bearings operated at Reynolds numbers above $1e7$. Ghezali et. al. [53] analyzed the flow in a hydrostatic bearing with Reynolds numbers varying from 500-3500. Again the SST k-ω turbulence model was used for all of the analysis. Worse, many authors do not provide enough information to calculate the Reynolds number of the bearing flow. Edney et. al. [54], Uhkoetter et. al. [55], Manshoor et. al. [56], and Fu and Untaroiu [22] all used k-ϵ models. These studies examined oil flow in a variety of bearing types. (hydrostatic bearings [22], fixed-geometry bearings [55, 56] and six-pad, tilting-pad bearings [54]). However, inadequate information was provided to calculate the Reynolds numbers. This missing data makes examining the validity of the chosen turbulence model impossible.

The two-equation, turbulence model is the primary turbulence model used in CFD in literature. This was often done with little justification of the choice of model and often presented with inadequate data for calculating the Reynolds number. Therefore, this chapter presents a study of three different turbulence models, along with the laminar model, over a wide range of Reynolds numbers with the goal of trying to better determine the applicability of each model. A discussion is presented on different flow conditions in tight clearances, as seen in fluid-film bearings. To accomplish this, a CFD model was developed of a four-pad tilting pad-bearing and validated against experimental results [57]. The CFD model was used to examine a 2-equation turbulence model (k-ω SST), a 1-equation model (eddy viscosity transport), a zero-equation model, and a laminar model under a broad range of Reynolds numbers. The Reynolds number is varied from 10 to 40e3. This chapter presents an argument against using the more complicated turbulence model for all flow conditions in thin film applications, which has been the trend in the literature.

The objectives for this chapter were to:

1. Discuss the issues with modeling turbulence in fluid-film bearing applications

2. Compare the results across a broad range of Reynolds numbers of using CFD with a

- laminar model
- zero-equation turbulence model
- one-equation turbulence model
- two-equation turbulence model

3. Examine the the appropriate range of Reynolds number for the applicability of each of the different models

5.2 Theoretical Comparisons

Boundary layers form along the surfaces of the bearing and journal. These boundary layers are formed of three distinct layers. Closest to the wall is the viscous sublayer. The lower velocities due to the no-slip condition on the wall result in lower Reynolds number and predominantly laminar flow. The next region is the buffer layer. The flow in this region is neither fully turbulent nor fully laminar. The last sublayer of the boundary layer is the log-law region.

An important parameter pertaining to the sublayers is the nondimensional distance from the wall. One method of defining a non-dimensional distance for a wall-bounded flow is by using y^+ defined in Equation 5.2

$$y^+ = \frac{u_* y}{\nu}, \tag{5.2}$$

where u_* is the friction velocity, y is the distance from the wall, and ν is the local kinematic viscosity. The variable, y^+_{mesh} is also typically used in numerical modeling in reference to a mesh where y. Equation 5.2 is still used but y is redefined as the height of the first element layer. Each turbulence model has an acceptable range for the y^+_{mesh}.

Von Karman's theory states that the viscous layer exists in the region with a y^+ value less than 5. The buffer layer occurs in the region with a y^+ between 5 and 30, and beyond that is the log-law region. Due to the incorporation of the Reynolds number into the y^+ value, this theory holds for flows across the spectrum of Reynolds numbers.

The k-ω SST[45, 46] (2-equation) model requires a y^+_{mesh} below the viscous layer or less than 5. However, it is generally recommended that this value actually be less than that so that there are multiple elements in the viscous layer. Conversely the k-ϵ turbulence model [41] requires a y^+_{mesh} above the buffer layer or greater than 30.

Turbulence modeling in machine components with very tight clearances can develop into several different flow profiles depending upon the speeds and dimensions involved. Considering the flow between two flat plates of differing velocities with a small clearance, Figures 69-71 shows the different flow

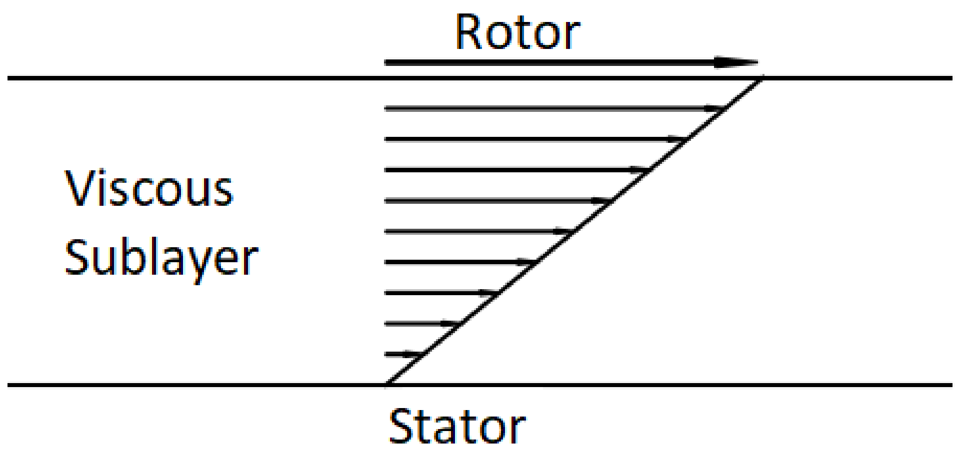

Figure 69: Flow profile of flow where viscous sublayers on the walls contact

profiles that can occur. In cases of relatively low speed and tight clearances (Figure 69), the viscous sublayers from both walls fill the entire clearance and laminar flow occurs across the film. This case can be modeled easily using standard laminar assumptions. When the involved velocities or clearances increase, there will be room for the entirety of both viscous sublayers and only a single buffer layer (Figure 70). This buffer layer is composed of the interaction between the buffer layers from each wall. The turbulent kinetic energy becomes important in this flow regime. However, the turbulent dissipation term will be significantly less than seen in fully turbulent flow. The last case (Figure 71) occurs under higher velocities and clearances. This case has a turbulent core in the center of the flow and a buffer and viscous sublayer on each wall. Now the turbulent dissipation becomes important as energy is dissipated from the system. It is important to know whether a turbulent core has formed to model the turbulence in machine components with extremely tight clearances. If the turbulent core does not form, then the turbulent dissipation term should not be included in the turbulence model.

Because of the highly varying film thickness in a bearing ($0 < h < 2C_b$ for a cylindrical bore, fixed geometry bearing), the local Reynolds number can vary significantly. The flow in the film can have both turbulent flow and laminar flow in different regions of the film. This makes modeling the flow in many bearings challenging as most models require a single turbulence model or laminar assumption for the whole flow. The ability of a turbulence model to accurately predict flow in both the laminar and turbulent regions would be extremely useful in the modeling of fluid-film bearings.

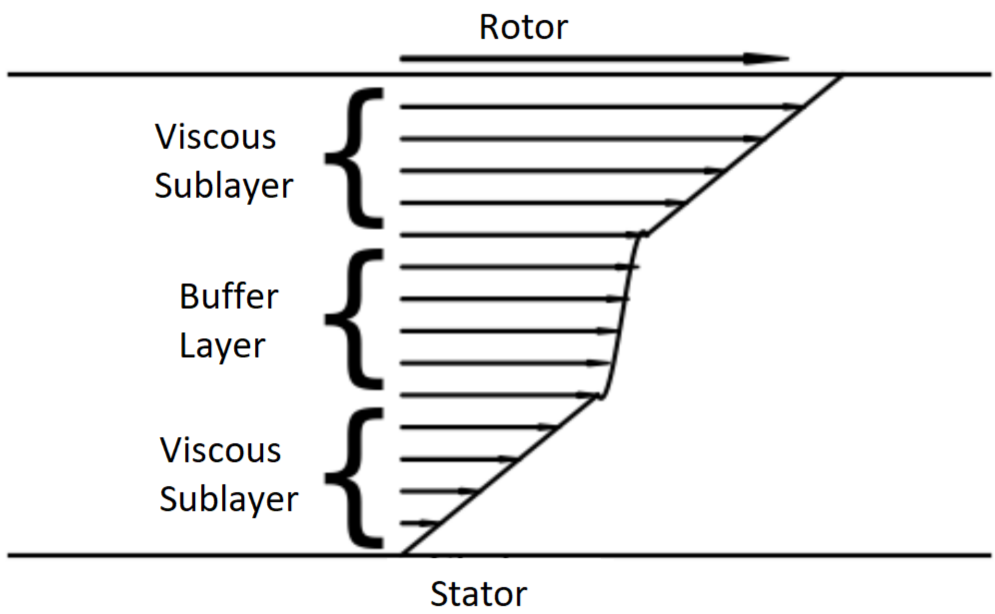

Figure 70: Flow profile of flow where boundary layers from the walls contact

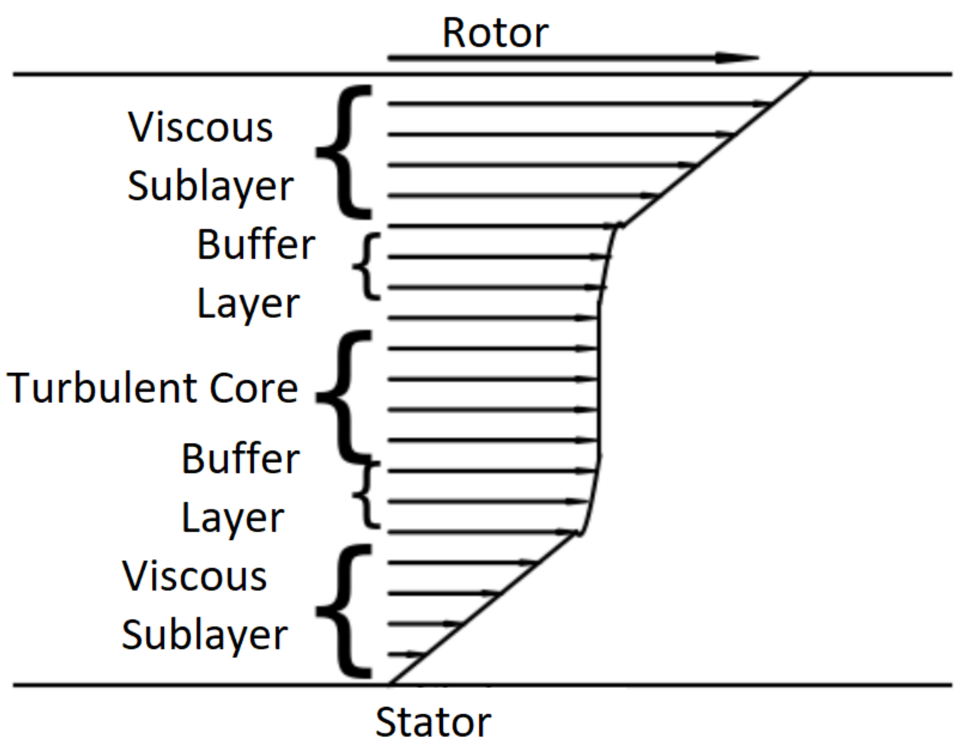

Figure 71: Flow profile of flow with turbulent core

Table 31: Taniguchi [57] bearing geometry

Journal Diameter	mm	479
Axial Length	mm	300
Pad Thickness	mm	11
Radial Cb	mm	0.612
Pad Arc Length	deg	80
Preload		0.0
Offset		0.5
Shell Heat Conductivity	W/m-°C	50
Lubricant Density	kg/m	855
Lubricant Specific Heat	J/kg-°C	1952
Lubricant Heat Conductivity	W /m-°C	0.15
Lubricant Viscosity at 40 °C	Pa-s	0.028
Lubricant Viscosity at 99 °C	Pa-s	0.0047
Lubricant Supply Temperature	°C	40
Shaft Speed	rpm	3000
Load	kN	180

5.3 CFD Bearing Model

For this study, ANSYS CFX was used to analyze the different turbulence models over a broad range of Reynolds numbers. Four turbulence models were chosen with varying complexity. The k-ω SST (2-equation) model [45, 46], the eddy viscosity transport model [47] (1-equation model), a zero-equation model based on a variation of the Prandtl-Kolmogorov expression, and a laminar model were chosen in this study. The application of these turbulence models to fluid-film, tilting-pad bearings using oil as the working fluid was examined. A bearing model was constructed based on the experimental study of Taniguchi et. al. [57]. The bearing is a four-pad, tilting pad bearing and its geometric parameters and operating conditions are given in Table 31 and a cross section is shown in Figure 72. A CFD model was created of pad 3 using ANSYS CFX. Due to the nature of tilting pad bearings with the load between pads, it was assumed that this pad will be supporting half of the rotor load and have a horizontal force equal but opposite to that experienced on pad 4 [71]. Using the experimental film thickness data, an operating eccentricity and pad tilt angle were calculated.

Figure 73 presents some experimental and numerical results from Taniguchi et. al. [57]. The drop in the maximum temperature around 3000 rpm oc-

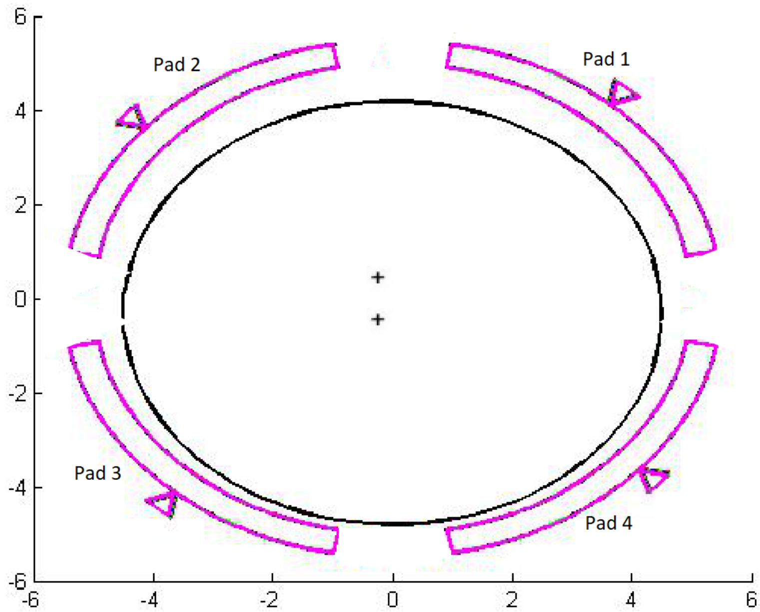

Figure 72: Taniguchi et. al. [57] Cross Section

curred due to the onset of turbulence [28, 29]. The operating conditions at the turbulence onset (grey oval in Figure 73) were chosen to allow easy validation of the model with the results that were presented and to enable tuning of the model between laminar and turbulent flow conditions.

As this study was focused mainly on the turbulence flow models, an isoviscous, isothermal model was used. Axial symmetry along the center of the bearing was assumed to reduce the size of the model. The model was set up to easily transition between a laminar assumption or a zero-equation, one-equation, or two-equation turbulence model. A structured mesh was used composed of quadrilateral elements. Figure 74 shows a close-up view of the leading edge and axial symmetry edge for the 3 million element mesh.

Results of a mesh density study using the one-equation turbulence model are presented in Table 32. Increasing the mesh density from 3 million elements to 12 million elements yielded a change of less than 5%. Therefore, the 3 million element mesh was chosen for this investigation. This mesh was further refined for some of the cases with lower Reynolds numbers. The results from the 3 million element mesh were compared with the experimental results in Figure 75. The numerical results show generally good agreement with the experimental results. The CFD results underpredict the peak pressure by about 6% and fails to capture the pressure ram near the pad inlet. This inability to capture the pressure ram effect was expected as the flow

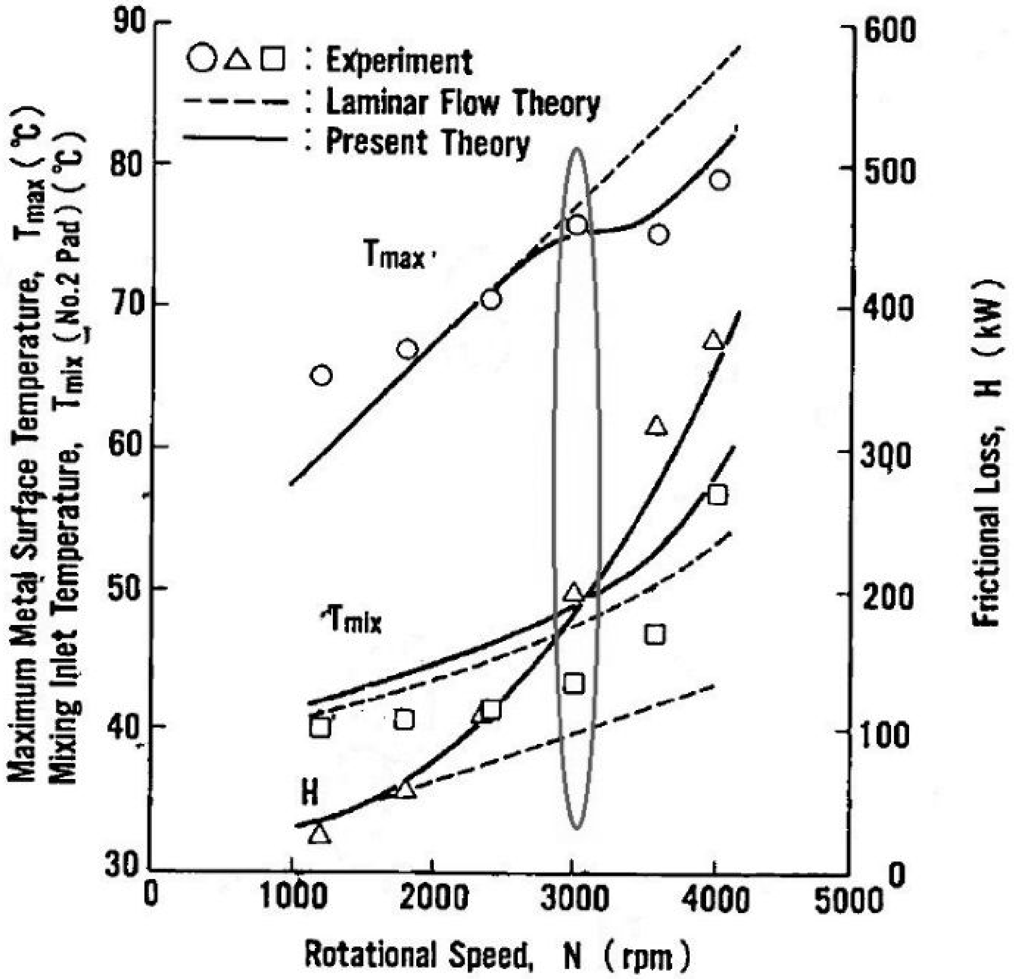

Figure 73: Taniguchi et. al. [57] Experimental and Numerical Results

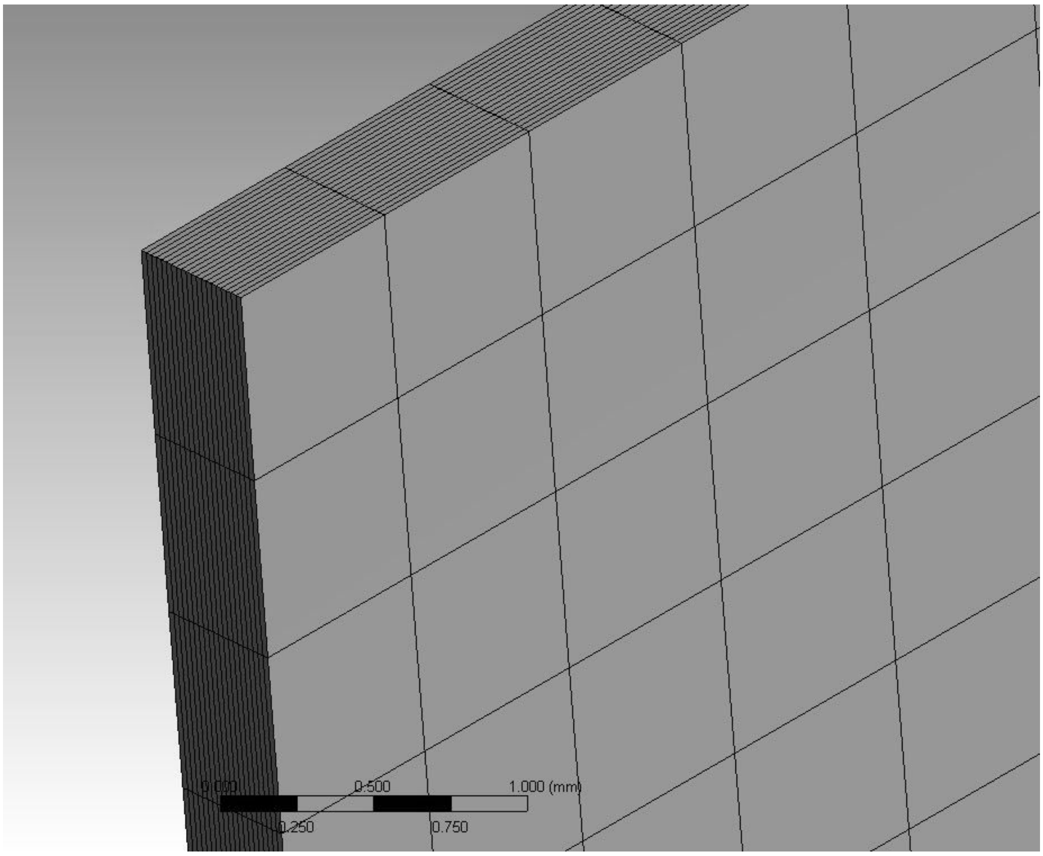

Figure 74: Close-up of 2.9 Million Element Mesh

Table 32: Mesh Densities for Pad 3 CFD Model using 1-Equation Turbulence Model

Number of Elements	Maximum Pressure	Percent Difference (%)
1.7 Million	6.47	-
2.9 Million	3.71	42.7
12 Million	3.54	4.64

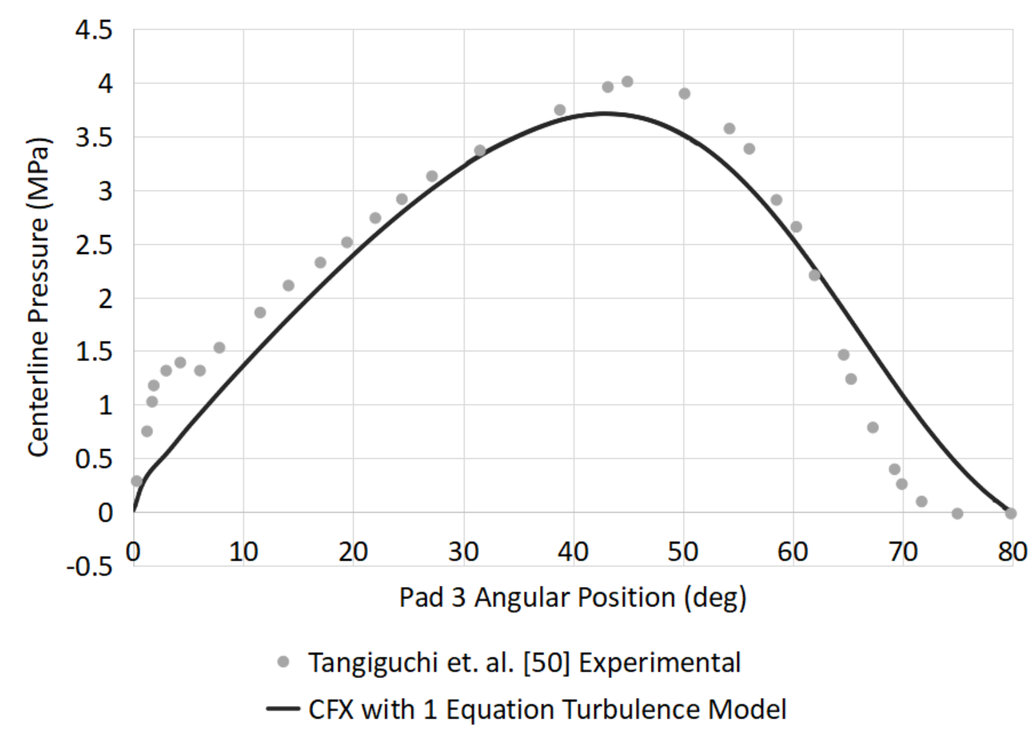

Figure 75: Pad 3 Centerline Pressure Comparison

region preceding the pad was not included in the model.

5.4 Results

After validating the base CFD case against the experimental data from Taniguchi et. al. [57], the influence of Reynolds number on the film hydrodynamic load of the different turbulence models was examined. The Reynnolds number was varied from 10 to 40e3 by varying the oil viscosity from 1.196

to 2.989e-4 Pa-s. Low Reynolds numbers were included in this range as it would be highly advantageous in the modeling of fluid-film bearings for a turbulence model to capture both the laminar and turbulent flow behavior. The resulting vertical load data is shown in Figure 76. The y axes show both the minimum and maximum Reynolds numbers that occur in the bearing based on the minimum and maximum film thicknesses. The applied load on pad 3 for the actual oil viscosity is also shown. The zero-equation model vastly overestimated the results in the laminar regime and was not in agreement with the other turbulence models in the laminar regime. The two-equation model did not predict an increase in the hydrodynamic load until the Reynolds numbers in the bearing varied between 1000-2400. These Reynolds numbers are much higher than those at which turbulence occurs in bearings [31, 72, 57]. When the onset of turbulence should be occuring, the two-equation model is still underpredicting the laminar solution. This was contrary to what is commonly seen in bearing operations [32, 33, 25]. The two-equation model also underpredicted the experimental results. The two-equation model underestimated the vertical force in the laminar regime with differences of 22% of the laminar results. The one-equation model matched fairly well with the laminar case at low Reynolds number, with differences of 6% of the laminar results. When the Reynolds numbers in the bearing were between 250-617, the one-equation model experienced an increase in the vertical force with increasing Reynolds number up to a minimum bearing Reynolds number of around 2500. Suganami and Szeri [31] and Brockwell et. al. [72] predicted the onset of turbulence occurring at Reynolds numbers between 400-900 and 500-800 respectively. These ranges correlated well with the location of the increased load predicted by the one-equation model. Figure 77 shows the same data but scaled by the laminar results. The two-equation model did not increase the load capacity of the bearing until well into the turbulent regime. The main difference between the one-equation and two-equation model is the inclusion of the dissipation differential equation. The magnitude of the dissipation term was causing the lower than expected hydrodynamic forces.

Another CFX mesh was created containing approximately 50 million elements to examine the influence of mesh density on the differences between the laminar assumption and the turbulence models at low Reynolds numbers. This model was run for each minimum Reynolds number case varying from 10 to 750. The percent differences between the 3 million element model and the 50 million element model are presented in Table 33.

The resulting vertical forces are plotted for the laminar, 1-equation, and 2-equation models in Figure 78 and Figure 79. The drop in the difference between the one-equation model and the laminar case can be seen in Figure 79.

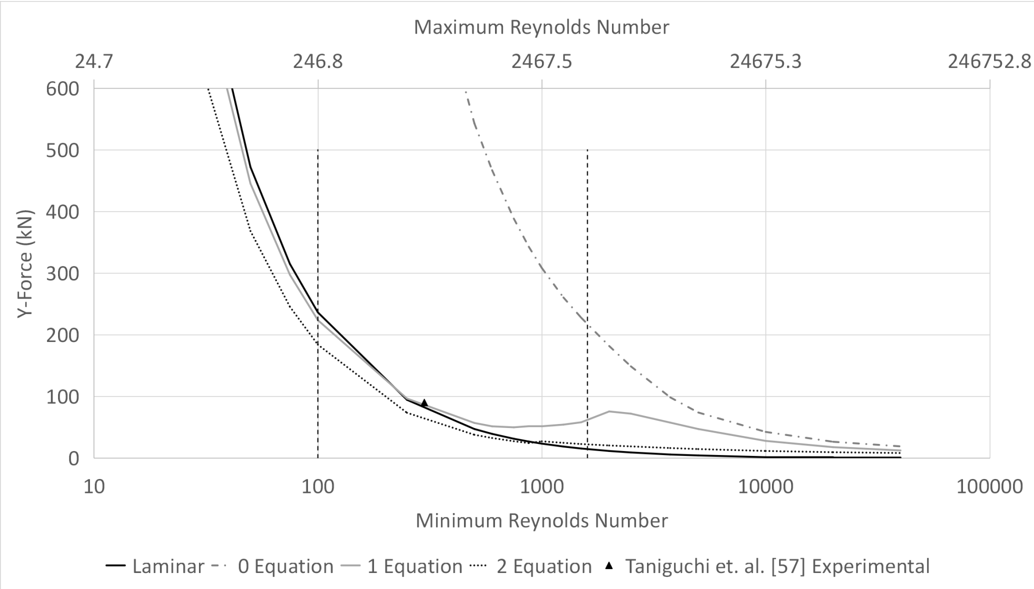

Figure 76: Load capacity for the coarse mesh (3 million elements)

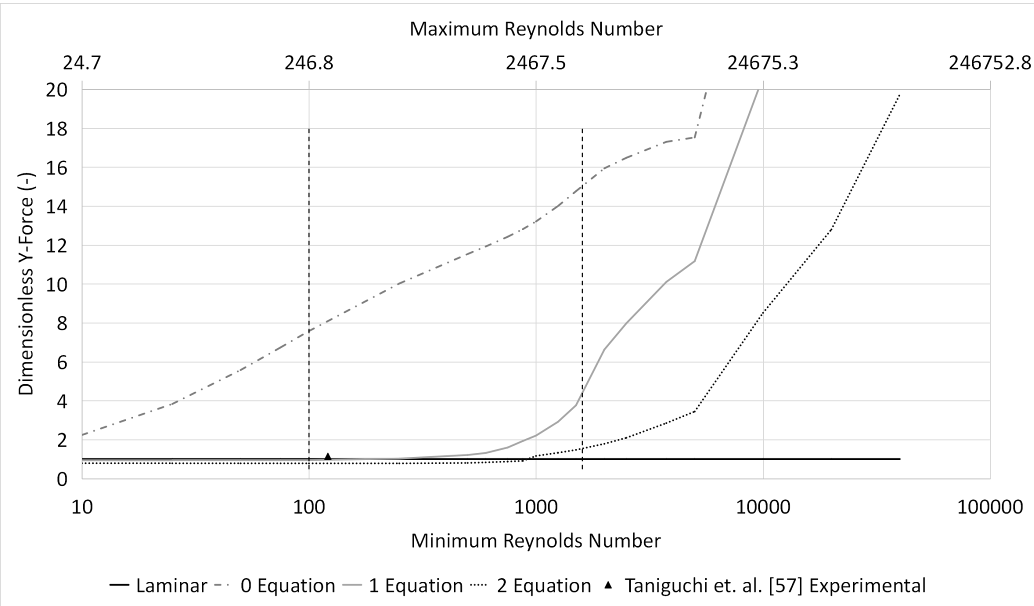

Figure 77: Nondimensional load capacity for the coarse mesh (3 million elements)

Table 33: Percent differences between the 50 million and 3 million mesh results for each turbulence model

Re	Laminar	0-Equation	1-Equation	2-Equation
10	1.3	-6.0	-1.7	-6.6
25	0.2	-8.8	-1.4	-7.4
50	-0.1	-16.6	-1.7	-7.7
75	-0.2	-20.6	-1.9	-7.9
100	-0.3	-23.7	-1.9	-8.0
250	-0.5	-33.3	-1.0	-8.5
500	-0.9	-38.2	-2.8	-10.5
750	-1.3	-39.2	-12.0	-2.7

For low Reynolds numbers, increasing the number of elements to 50 million did not greatly alter the results for one-equation turbulence model. However, the overall resulting percent difference between the laminar model and the one-equation model for Reynolds numbers in the laminar regime dropped from 5-6% to 3-4%. The finer mesh one-equation results still digressed from the laminar results at Reynolds numbers between approximately 250-617, the same as the coarse mesh. The finer mesh two-equation results also showed an increase in vertical load in the laminar regime. The differences between the two-equation and laminar results in this regime dropped from 22-13% to 16-12%. As the Reynolds number increased the results appeared to match up with the coarse results. The pad model with the finer mesh was not analyzed for Reynolds numbers high enough for the onset of turbulence for the two-equation model. However, based on Figure 79, the onset wouldn't have changed significantly based on the higher density mesh.

5.5 Conclusions

Two-equation turbulence models have been the primary method used in the literature for simulating turbulence in fluid-film bearings. This is commonly done regardless of the Reynolds number and without any justification of the selected turbulence model. Another challenge in analyzing fluid-film bearings is the wide range of Reynolds numbers that occurs in the different portions of the film. A turbulence model that can accurately predict the flow in both the turbulent regions and the laminar regions of the same flow would be highly advantageous. This study examined the acceptable use of several

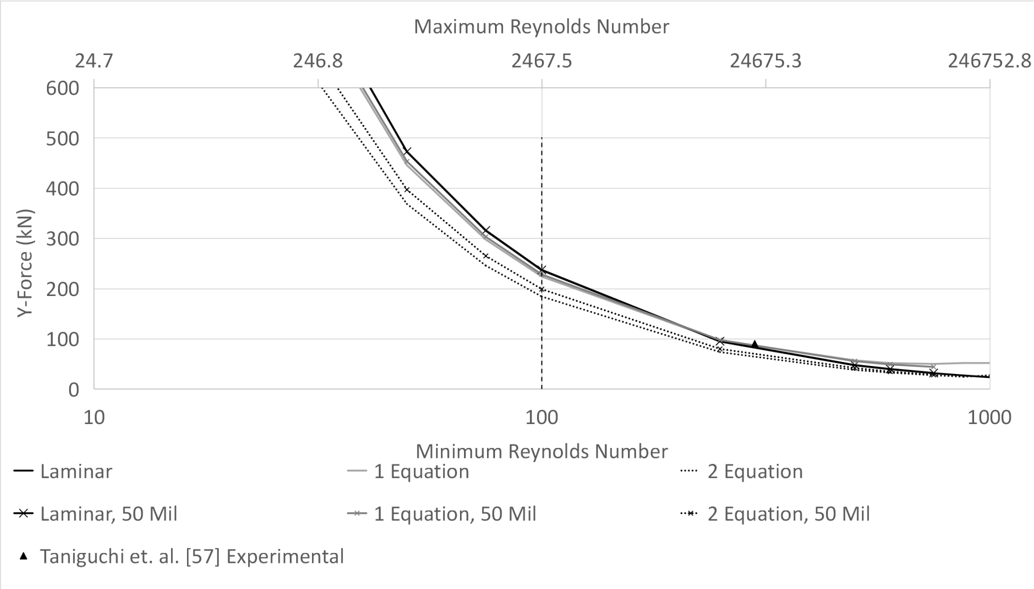

Figure 78: Mesh comparison of hydrodynamic forces in line with direction of loading at low Reynolds numbers

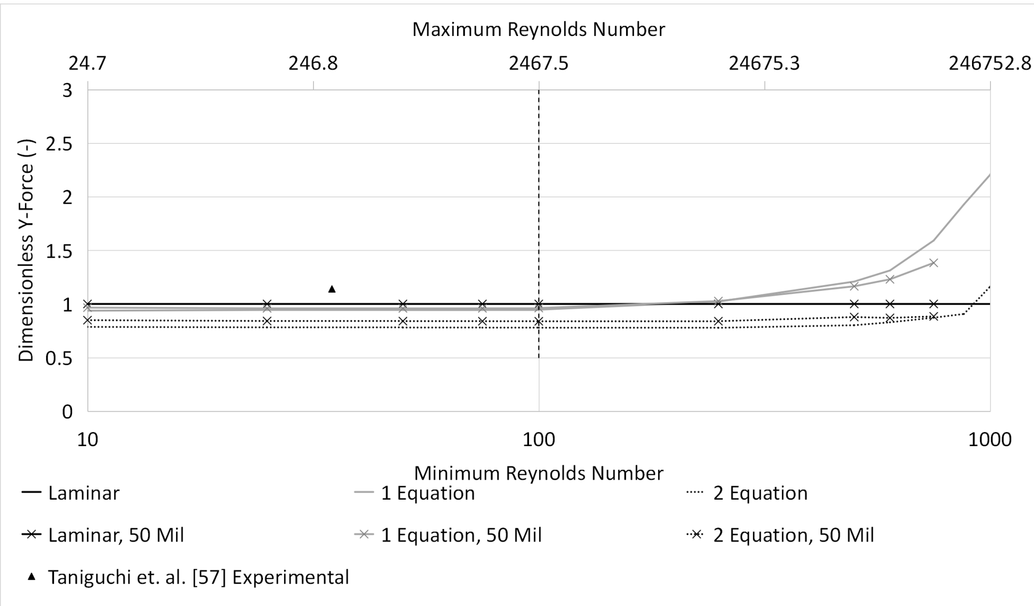

Figure 79: Mesh comparison of nondimensional hydrodynamic forces in line with direction of loading at low Reynolds numbers

different eddy viscosity turbulence models for thin film applications.

First a brief discussion of the wall effects on the turbulence in a thin-film was presented. Next, a bearing case study was presented which examined the influence of several different turbulence models on the hydrodynamic forces across a broad range of Reynolds number. The base CFD model was validated against experimental data from Taniguchi et. al. [57]. Then the geometry of the film was fixed and the Reynolds number was varied by altering the fluid viscosity. The hydrodynamic loads are presented for simulations using three different turbulence models and a laminar flow model. The three turbulence models were a zero-equation model based on the Prandtl-Kolmogorov expression, the eddy viscosity transport model (one-equation), and the k-ω SST model (two-equation).

For laminar flow conditions, the one-equation model corresponds quite well with the laminar model (up to 6% difference in vertical, hydrodynamic load). The one-equation model predicted the increase in hydrodynamic loads at Reynolds numbers which correspond well with prior studies [31, 72]. Therefore, the one-equation turbulence model can be used for bearings with Reynolds numbers near the predicted values for the onset of turbulence. The engineer does not have to know the exact Reynolds number at which this occurs, and this turbulence model can be used across the whole bearing despite the variation of Reynolds numbers. The two-equation model underpredicts the loads by up to 22% in the laminar regime, while the zero-equation model largely overpredicts them. The increase in vertical load occurred well after the predicted onset Reynolds numbers [31, 72] for the two-equation model. The vertical load predicted by the two-equation model was improved to 16% underprediction in the laminar region when a very fine mesh was used. Achieving a fine enough mesh to further reduce this error is generally not practical with current computers. This underprediction continued even when the Reynolds number was large enough for turbulence to begin to occur. This drop in load capacity did not correspond well with current experimental literature on fluid-film bearings [31, 72]. It would be highly advantageous to take advantage of the one-equation model's capability to more accurately capture the behavior in laminar and lower Reynolds numbers turbulence in fluid-film bearing application. This would reduce the reliance on experimental parameters to determine the onset of turbulence. The one-equation model is able to achieve this quite well. Further studies are needed for determining the appropriate Reynolds numbers and method of transitioning from a one-equation model to a two-equation model while using a reasonable number of elements.

6 Conclusion

In Chapter 2 and Chapter 3, CFD models were developed for a fluid-film bearing with a stadium-shaped, jacking pocket, a pair of diamond-shaped, jacking pockets, and a hourglass-shaped, jacking groove. The models were validated using experimental results and a TEHD code. Defining parameters of the jacking features' geometries were then varied to assess their influence on bearing performance. The depth of the feature was varied for all three designs, along with the circumferential length of the stadium-shaped pocket and the groove width of the hourglass-shaped groove. Finally, design-of-experiment and linear regression models were used to examine each of the different geometric parameters and any interaction effects.

As the depth of the features increase, the pressure profile transitions between two regimes before reaching a steady pressure profile for deep pockets. Stadium-shaped jacking pocket depths up to $0.28 \times C_b$ increased the load capacity of the bearing by as much as 6%. A similar increase was seen for the double diamond pockets, although the peak load capacity occurred at pocket depths of $0.60 \times C_b$. As the depths increased further, the pressure became constant across the pocket and the peak pressure shifted downstream of the pocket. In all three cases, the transition to a deep pocket is completed at a pocket depth of about $7 \times C_b$. The hourglass-shaped groove shows similar results for depths beyond $0.60 \times C_b$ but had a slight loss in load capacity for shallow grooves. The pair of diamond pockets, the hourglass-shaped groove, and the stadium-shaped pocket all transitioned between two regimes as the depth of the feature increased. The flow trends were similar for each geometry. The first regime saw a drop in pressure occurring immediately prior to the leading edge of the feature. Downstream of the leading edge of the feature, a rapid increase in the pressure occurred. The second regime was characterized by equalization of the pressure across the feature and development of a peak pressure occurring slightly downstream of the feature. The two regimes were very distinct, with a specific depth at which the transition happened, for both the hourglass-shaped groove and stadium-shaped pocket. This occurred at a depth of $0.6 \times C_b$ for the groove and $0.28 \times C_b$ for the stadium-shaped pocket. The double diamond pockets gradually shifted between the two regimes. The pressure at the leading edge of the pocket continued to drop as the peak pressure decreased. This range occurred at depths varying from $0.34 \times C_b$ - $0.60 \times C_b$.

The presence of jacking features had a minimal effect on the power loss in the bearing and journal equilibrium position. This held true for all three geometries. However, their presence can change the stiffness characteristics by a significant amount. The geometry of the pair of double diamonds pockets had variation in K_{xx}, K_{yy}, K_{xy}, and K_{yx} of 38%, 36%, 104%, and 31%, respectively. Failing to understand the influence of this design can introduce a high degree of cross coupling in the system. This can contribute significantly to rotordynamic instability. The geometry of the stadium-shaped pocket from Chapter 2 had variation in K_{xx}, K_{yy}, K_{xy}, and K_{yx} of 27%, 6%, 8%, and 12%, respectively. The pocket depth in Chapter 2 was more limited than the studies performed in Chapter 3. It is hypothesized that this is the reason that the variation is so much higher for the pair of diamond pockets than for the stadium-shaped pocket. The hourglass-shaped groove had variation in K_{xx}, K_{yy}, K_{xy}, and K_{yx} of 23%, 12%, 26%, and 20%, respectively. This jacking feature has much less of an effect on the film stiffness than the pair of diamond pockets (and potentially the stadium-shaped pocket). The variation in stiffness caused by the groove can still be important to understand to ensure overall machine stability.The variation in the direct stiffness terms can influence the location of the system critical speeds, which can result in higher than acceptable vibration in the machines. These studies are the first to examine how each aspect of a jacking pocket's geometry influence the operation and linear stiffness values of a fluid-film journal bearing.

In Chapter 4, the applicability of the Reynolds equation to fluid-film, journal bearings with jacking pockets was examined. This was done by comparing results using a Reynolds equation solver to an experimentally verified CFD model. Several different methods for performing an analysis using the Reynolds equation were examined. The superior method was to bias the elements towards the pocket to minimize the size of the elements along the border of the pocket. This method was applied to several different stadium-shaped jacking pocket designs. While the Reynolds equation generally underpredicts the pressure profile, this difference disappears when the journal eccentricity is optimized to an equilibrium position. Performing this optimization increased the eccentricity positions by 2-4% of the total radial clearance. Aside from being minimal, this increase is a conservative error which will result in safer bearing operation.

Justification for the acceptable use of the Reynolds equation for bearings with hydrostatic lifting feature has not been previously addressed in the literature. The results of this work demonstrate that the Reynolds equation can be used successfully to capture the physics that occur in fluid-film, journal bearings containing jacking pockets. Biasing should be used to ensure that thin elements exist around the border of the pocket. These thin elements reduce the numerical error associated with the sudden transition in film thickness. Doing this will help reduce overall mesh sizes and simulation runtimes. Although the Reynolds equation underpredicts the pressure in the bearing for a given journal position, this difference is mitigated by allowing the journal to find its own equilibrium position. Conversely, the changes in journal equilibrium position due to the lack of inertia terms in Reynolds equation and other modeling errors will result in a more conservative bearing design.

Chapter 5 presented a case study on the influence of several different turbulence models on the hydrodynamic forces generated in a fluid-film, journal bearing. A base model was developed and validated against experimental data. The Reynolds number was then varied from 10 to 40e3 by altering the fluid viscosity and the hydrodynamic forces are presented. The three different turbulence models are a zero-equation model based on the Prandtl-Kolmogorov expression, the eddy viscosity transport model (one-equation), and the k-ω SST model (two-equation), as well as a laminar flow model. Because of the highly varying film thickness in a bearing, the local Reynolds number can vary significantly throughout the film. The ability of a turbulence model to accurately predict flow in both the laminar and turbulent regions would be extremely useful in the modeling of fluid-film bearings.

The one-equation model corresponds best with the laminar model under laminar flow conditions. The two-equation model underpredicts the loads by up to 22% while the zero-equation model largely overpredicts them. A very fine mesh was able to reduce the error in the two-equation model to 10% in this region. Increasing the fineness of the mesh enough to further reduce the error isn't achievable on a standard computer. The underpediction of this model continues even when the Reynolds number is large enough for turbulence to begin to occur, and this drop in load capacity does not correspond well with experimental literature of fluid-film bearings. It would be highly advantageous to take advantage of the one-equation model's capability to more accurately capture the behavior in laminar and lower Reynolds numbers turbulence in fluid-film bearing application. This would reduce the reliance on experimental parameters to determine the onset of turbulence. The one-equation model is able to achieve this quite well. Further studies are needed for determining the exact Reynolds number and a proper method for transitioning from a 1-equation model to a 2-equation model.

Acknowledgements

I would like to thank God for watching over me during this process and using it to pull me closer to him. I would like to thank my beautiful wife, Rachel Branagan, for all of her patience and support over the course of my degree. I would like to thank the Rotating Machinery and Controls Laboratory for funding this research. I would like to thank my advisors Dr. Christopher Goyne and Dr. Roger Fittro for all their support and guidance in this work. I would also like to thank Dr. Robert Rockwell and Dr. Minhui He for their insight and direction. I would like to thank Dr. Lyle Branagan, Dr. Cori Watson, and Neal Morgan who provided their expertise and advice towards this research. I would like to thank my family for all their encouragement and heckling. I would also like to thank Pioneer Motor Bearing for their support and patience in this endeavor.

References

[1] G. Welter and W. Brasch, "Test on plain bearings with a new method of lubrication under very high pressure," *Phil. Trans. Roy. Soc., Lond. Ser.*, vol. 257, pp. 31–70, 1937.

[2] X. Raud, M. Fillon, and M. Helene, "Numerical modelling of hydrostatic lift pockets in hydrodynamic journal bearings–application to low speed working conditions of highly loaded tilting pad journal bearings," *Mechanics & Industry*, vol. 14, no. 5, pp. 327–334, 2013.

[3] L. San Andres, "Turbulent hybrid bearings with fluid inertia effects," *Journal of tribology*, vol. 112, no. 4, pp. 699–707, 1990.

[4] V. Constantinescu and S. Galetuse, "Pressure drop due to inertia forces in step bearings," *Journal of Lubrication Technology*, vol. 98, no. 1, pp. 167–174, 1976.

[5] M. Braun, F. Choy, and Y. Zhou, "The effects of a hydrostatic pocket aspect ratio, supply orifice position, and attack angle on steady-state flow patterns, pressure, and shear characteristics," *Journal of tribology*, vol. 115, no. 4, pp. 678–685, 1993.

[6] M. Helene, M. Arghir, and J. Frene, "Numerical study of the pressure pattern in a two-dimensional hybrid journal bearing recess, laminar, and turbulent flow results," *TRANSACTIONS-AMERICAN SOCIETY OF*

MECHANICAL ENGINEERS JOURNAL OF TRIBOLOGY, vol. 125, no. 2, pp. 283–290, 2003.

[7] M. Helene, M. Arghir, J. Frene, *et al.*, "Numerical three-dimensional pressure patterns in a recess of a turbulent and compressible hybrid journal bearing," *TRANSACTIONS-AMERICAN SOCIETY OF MECHANICAL ENGINEERS JOURNAL OF TRIBOLOGY*, vol. 125, no. 2, pp. 301–308, 2003.

[8] P. Liang, C. Lu, W. Pan, and S. Li, "A new method for calculating the static performance of hydrostatic journal bearing," *Tribology International*, vol. 77, pp. 72–77, 2014.

[9] R. E. Johnson and N. D. Manring, "Sensitivity studies for the shallow-pocket geometry of a hydrostatic thrust bearing," *American Society of Mechanical Engineers, the Fluid Power and Systems Technology Division (Publication) FPST*, vol. 10, pp. 231–238, 2003.

[10] E. V. Kumar, V. M. Phalle, S. C. Sharma, and S. Jain, "Analysis of a worn multirecess hydrostatic journal bearing system," in *ASME 2009 International Design Engineering Technical Conferences and Computers and Information in Engineering Conference*, pp. 1089–1095, American Society of Mechanical Engineers, 2009.

[11] K. Dufrane, J. Kannel, and T. McCloskey, "Wear of steam turbine journal bearings at low operating speeds," *Journal of lubrication technology*, vol. 105, no. 3, pp. 313–317, 1983.

[12] V. K. Dwivedi, S. Chand, and K. Pandey, "Effect of number and size of recess on the performance of hybrid (hydrostatic/hydrodynamic) journal bearing," *Procedia Engineering*, vol. 51, pp. 810–817, 2013.

[13] R. Wordsworth and C. Ettles, "The effect of jacking pockets in hydrodynamic thrust pads," *Wear*, vol. 31, no. 1, pp. 167–171, 1975.

[14] N. Heinrichson and I. Santos, *On the design of tilting-pad thrust bearings*. Technical University of DenmarkDanmarks Tekniske Universitet, Department of Mechanical EngineeringInstitut for Mekanisk Teknologi, 2006.

[15] N. Heinrichson, I. F. Santos, and A. Fuerst, "The influence of injection pockets on the performance of tilting-pad thrust bearings—part i: theory," *Journal of Tribology*, vol. 129, no. 4, pp. 895–903, 2007.

[16] N. Heinrichson, A. Fuerst, and I. F. Santos, “The influence of injection pockets on the performance of tilting-pad thrust bearings—part ii: comparison between theory and experiment,” *Journal of Tribology*, vol. 129, no. 4, pp. 904–912, 2007.

[17] D. V. De Pellegrin and D. J. Hargreaves, “An isoviscous, isothermal model investigating the influence of hydrostatic recesses on a spring-supported tilting pad thrust bearing,” *Tribology international*, vol. 51, pp. 25–35, 2012.

[18] M. Fillon, M. Wodtke, and M. Wasilczuk, “Effect of presence of lifting pocket on the thd performance of a large tilting-pad thrust bearing,” *Friction*, vol. 3, no. 4, pp. 266–274, 2015.

[19] M. Wodtke, M. Fillon, A. Schubert, and M. Wasilczuk, “Study of the influence of heat convection coefficient on predicted performance of a large tilting-pad thrust bearing,” *Journal of Tribology*, vol. 135, no. 2, p. 021702, 2013.

[20] M. Wodtke, A. Schubert, M. Fillon, M. Wasilczuk, and P. Pajączkowski, “Large hydrodynamic thrust bearing: Comparison of the calculations and measurements,” *Proceedings of the Institution of Mechanical Engineers, Part J: Journal of Engineering Tribology*, vol. 228, no. 9, pp. 974–983, 2014.

[21] V. Zouzoulas and C. I. Papadopoulos, “3-d thermohydrodynamic analysis of textured, grooved, pocketed and hydrophobic pivoted-pad thrust bearings,” *Tribology International*, vol. 110, pp. 426–440, 2017.

[22] G. Fu and A. Untaroiu, “A study of the effect of various recess shapes on hybrid journal bearing performance using computational fluid dynamics and response surface method,” *Journal of Fluids Engineering*, vol. 139, no. 6, p. 061104, 2017.

[23] J. Hinze, *Turbulence.* McGraw-Hill, 2 ed., 1975.

[24] R. Granger, *Fluid Mechanics.* Dover Books on Physics, Dover Publications, 1995.

[25] R. W. Armentrout, M. He, T. Haykin, and A. E. Reed, “Analysis of turbulence and convective inertia in a water-lubricated tilting-pad journal bearing using conventional and cfd approaches,” *Tribology Transactions*, vol. 60, no. 6, pp. 1129–1147, 2017.

[26] A. Z. Szeri, *Tribology: friction, lubrication, and wear.* McGraw-Hill, 1980.

[27] J. Frene, "Tapered land thrust bearing operating in both laminar and turbulent regimes," *Asle Transactions*, vol. 21, no. 3, pp. 243–249, 1978.

[28] A. Szeri, "Some extensions of the lubrication theory of osborne reynolds," *Journal of tribology*, vol. 109, no. 1, pp. 21–36, 1987.

[29] G. Hopf and D. Schuler, "Investigations on large turbine bearings working under transitional conditions between laminar and turbulent flow," *Journal of Tribology*, vol. 111, no. 4, pp. 628–634, 1989.

[30] A. Tieu, "Oil-film temperature distribution in an infinitely wide slider bearing: An application of the finite-element method," *Journal of Mechanical Engineering Science*, vol. 15, no. 4, pp. 311–320, 1973.

[31] T. Suganami and A. Szeri, "A parametric study of journal bearing performance: the 80 deg partial arc bearing," *Journal of Lubrication Technology*, vol. 101, no. 4, pp. 486–491, 1979.

[32] C. Taylor, "Paper 6: Turbulent lubrication theory applied to fluid film bearing design," in *Proceedings of the Institution of Mechanical Engineers, Conference Proceedings*, vol. 184, pp. 40–47, SAGE Publications Sage UK: London, England, 1969.

[33] O. Pinkus, *Thermal aspects of fluid film tribology.* American Society of Mechanical Engineers, 1990.

[34] A. Missana, E. Booser, and F. Ryan, "Performance of tapered land thrust bearings for large steam turbines," *ASLE TRANSACTIONS*, vol. 14, no. 4, pp. 301–306, 1971.

[35] I. Boussinesq, "Mem. pres, par div. savants a'l'acad. sci," *Paris*, vol. 23, p. 46, 1877.

[36] V. Constantinescu, "On turbulent lubrication," *Proceedings of the Institution of mechanical engineers*, vol. 173, no. 1, pp. 881–900, 1959.

[37] C.-W. Ng, "Fluid dynamic foundation of turbulent lubrication theory," *Asle Transactions*, vol. 7, no. 4, pp. 311–321, 1964.

[38] H. Reichardt, "Vollständige darstellung der turbulenten geschwindigkeitsverteilung in glatten leitungen," *ZAMM-Journal of Applied Mathematics and Mechanics/Zeitschrift für Angewandte Mathematik und Mechanik*, vol. 31, no. 7, pp. 208–219, 1951.

[39] H. Elrod and C. Ng, "A theory for turbulent fluid films and its application to bearings," *Journal of Lubrication Technology*, vol. 89, no. 3, pp. 346–362, 1967.

[40] K. Hanjalic, *Two-dimensional asymmetric turbulent flow in ducts*. PhD thesis, University of London, 1970.

[41] W. Jones and B. Launder, "The prediction of laminarization with a two-equation model of turbulence," *International journal of heat and mass transfer*, vol. 15, no. 2, pp. 301–314, 1972.

[42] B. Launder and B. Sharma, "Application of the energy-dissipation model of turbulence to the calculation of flow near a spinning disc," *Letters in heat and mass transfer*, vol. 1, no. 2, pp. 131–137, 1974.

[43] D. C. Wilcox, "Reassessment of the scale-determining equation for advanced turbulence models," *AIAA journal*, vol. 26, no. 11, pp. 1299–1310, 1988.

[44] D. C. Wilcox, "Multiscale model for turbulent flows," *AIAA journal*, vol. 26, no. 11, pp. 1311–1320, 1988.

[45] F. Menter, "Zonal two equation k-ω turbulence models for aerodynamic flows," in *23rd fluid dynamics, plasmadynamics, and lasers conference*, p. 2906, 1993.

[46] F. R. Menter, "Two-equation eddy-viscosity turbulence models for engineering applications," *AIAA journal*, vol. 32, no. 8, pp. 1598–1605, 1994.

[47] F. R. Menter, "Eddy viscosity transport equations and their relation to the k-ε model," *Journal of fluids engineering*, vol. 119, no. 4, pp. 876–884, 1997.

[48] P. Bradshaw, D. Ferriss, and N. Atwell, "Calculation of boundary-layer development using the turbulent energy equation," *Journal of Fluid Mechanics*, vol. 28, no. 3, pp. 593–616, 1967.

[49] C. Taylor and D. Dowson, "Turbulent lubrication theory—application to design," *Journal of Lubrication Technology*, vol. 96, no. 1, pp. 36–46, 1974.

[50] Z. Safar and A. Szeri, "Thermohydrodynamic lubrication in laminar and turbulent regimes," *Journal of Lubrication Technology*, vol. 96, no. 1, pp. 48–56, 1974.

[51] L. Bouard, M. Fillon, and J. Frene, "Comparison between three turbulent models—application to thermohydrodynamic performances of tilting-pad journal bearings," *Tribology international*, vol. 29, no. 1, pp. 11–18, 1996.

[52] Y. A. Ravikovich, Y. I. Ermilov, A. O. Pugachev, A. A. Matushkin, and D. P. Kholobtsev, "Prediction of operational characteristics of fluid-film and gas bearings for high-speed turbomachinery using computational fluid dynamics," *Proceedings of the 29th Congress of the International Council of the Aeronautical Sciences*, 2014.

[53] F. Ghezali, A. Bouzidane, and M. Thomas, "Influence of flow regime in a recess on the pressure field of an orifice compensated hydrostatic bearing," *Proceedings of the International Symposium on Aircraft Materials (ACMA)*, 2014.

[54] S. L. Edney, G. B. Heitland, and S. M. DeCamillo, "Testing, analysis, and cfd modeling of a profiled leading edge groove tilting pad journal bearing," *In ASME TURBO EXPO Conference, Stockholm (Sweden)*, pp. 2–5, 1998.

[55] S. Uhkoetter, S. aus der Wiesche, M. Kursch, and C. Beck, "Development and validation of a three-dimensional multiphase flow computational fluid dynamics analysis for journal bearings in steam and heavy duty gas turbines," *Journal of Engineering for Gas Turbines and Power*, vol. 134, no. 10, p. 102504, 2012.

[56] B. Manshoor, M. Jaat, Z. Izzuddin, and K. Amir, "Cfd analysis of thin film lubricated journal bearing," *Procedia Engineering*, vol. 68, pp. 56–62, 2013.

[57] S. Taniguchi, T. Makino, K. Takeshita, and T. Ichimura, "A thermohydrodynamic analysis of large tilting-pad journal bearing in laminar and turbulent flow regimes with mixing," *Journal of Tribology*, vol. 112, no. 3, pp. 542–548, 1990.

[58] M. Fitzgerald and P. Neal, "Temperature distributions and heat transfer in journal bearings," *Journal of tribology*, vol. 114, no. 1, pp. 122–130, 1992.

[59] M. He, *Thermoelastohydrodynamic analysis of fluid film journal bearings.* PhD thesis, Ph. D. dissertation, University of Virginia, Charlottesville, Virginia, USA, 2003.

[60] S. Dousti, "An extended reynolds equation development with applications to fixed geometry bearings and squeeze film dampers," *PhD diss., Ph. D. dissertation, University of Virginia, Charlottesville, Virginia, USA*, 2014.

[61] G. S. Nassab, "Inertia effect on the thermohydrodynamic characteristics of journal bearings," *Proceedings of the Institution of Mechanical Engineers, Part J: Journal of Engineering Tribology*, vol. 219, no. 6, pp. 459–467, 2005.

[62] M. Braun and W. Hannon, "Cavitation formation and modelling for fluid film bearings: a review," *Proceedings of the Institution of Mechanical Engineers, Part J: Journal of Engineering Tribology*, vol. 224, no. 9, pp. 839–863, 2010.

[63] L. Branagan, "Toward a quantitative analysis of journal and bearing scratches," *Proceedings the 5th EDF/Pprime Workshop*, 2006.

[64] G. E. Box, J. S. Hunter, and W. G. Hunter, *Statistics for experimenters: design, innovation, and discovery*, vol. 2. Wiley-Interscience New York, 2005.

[65] F. Gao and L. Han, "Implementing the nelder-mead simplex algorithm with adaptive parameters," *Computational Optimization and Applications*, vol. 51, no. 1, pp. 259–277, 2012.

[66] D. Kleinbaum, L. Kupper, A. Nizam, and E. Rosenberg, *Applied regression analysis and other multivariable methods.* Nelson Education, 2013.

[67] M. He, C. H. Cloud, J. M. Byrne, J. A. Vázquez, *et al.*, "Fundamentals of fluid film journal bearing operation and modeling," in *Asia Turbomachinery & Pump Symposium. 2016 Proceedings.*, Texas A&M University. Turbomachinery Laboratory, 2016.

[68] D. Dowson and C. M. Taylor, "Cavitation in bearings," *Annual Review of Fluid Mechanics*, vol. 11, no. 1, pp. 35–65, 1979.

[69] T. Suganami and A. Szeri, "A thermohydrodynamic analysis of journal bearings," *Journal of Lubrication Technology*, vol. 101, no. 1, pp. 21–27, 1979.

[70] D. Dowson, J. Hudson, B. Hunter, and C. March, "Paper 3: An experimental investigation of the thermal equilibrium of steadily loaded

journal bearings," in *Proceedings of the Institution of Mechanical Engineers, Conference Proceedings*, vol. 181, pp. 70–80, SAGE Publications Sage UK: London, England, 1966.

[71] J. C. Nicholas *et al.*, "Tilting pad bearing design.," in *Proceedings of the 23rd Turbomachinery Symposium*, Texas A&M University. Turbomachinery Laboratories, 1994.

[72] K. Brockwell, W. Dmochowski, S. DeCamillo, *et al.*, "Analysis and testing of the leg tilting pad journal bearing-a new design for increasing load capacity, reducing operating temperatures and conserving energy.," in *Proceedings of the 23rd Turbomachinery Symposium*, Texas A&M University. Turbomachinery Laboratories, 1994.